THIRD ORDER NONLINEARITY OF SEMICONDUCTOR QUANTUM DOTS COMPOSITES AND OPTICAL SIMULATIONS

by

YONGWANG GAO

A dissertation submitted to the Graduate Faculty in Engineering in partial fulfillment of the requirements for the degree of Doctor of Philosophy, The City University of New York

2007

UMI Number: 3245067

UMI Microform 3245067

ProQuest Information and Learning Company
300 North Zeeb Road
P.O. Box 1346
Ann Arbor, MI 48106-1346

This manuscript has been read and accepted for the
Graduate Faculty in Engineering in satisfaction of the
dissertation requirement for the degree of Doctor of Philosophy.

Mary J. Potasek

Jan. 23 2007

Date

Chair of Examining Committee

Mumtaz Kassir

Jan. 23 2007

Date

Executive Officer

Samir A. Ahmed

Roger Dorsinville

Ping-Pei Ho

Mark F. Arend

Supervisory Committee

THE CITY UNIVERSITY OF NEW YORK

Abstract

THIRD ORDER NONLINEARITY OF SEMICONDUCTOR QUANTUM DOTS COMPOSITES AND OPTICAL SIMULATIONS

By

Yongwang Gao

Adviser: Professor Mary. J. Potasek

Multiphoton processes are emerging as a significant class of phenomena. Accelerated growth in nanotechnology has led to new materials with unique physical and optical properties that have never been observed before. These developments have given rise to potential new applications and devices with physical properties that can far exceed those of traditional materials/systems. And we investigated multi-photon and multi-pulse train processes. First, we investigate novel materials with large third order nonlinearity consisting of semiconductor quantum dots in organic materials. We show that semiconductor quantum dots in an organic host matrix lead to significant enhancement of two-photon absorption. We developed a new synthesis method, and obtained CdS quantum dots using a surfactant as capping agent (decylamine). Historically, the formation of colloidal quantum dot preparation was sufficient for their use. However, for use as absorbers and other devices, the technology must be extended to the formation of thin films of these materials. Therefore we made the first, to our knowledge, optically transparent thin films of colloidal semiconductor quantum dots in reversed micelle structure using polystyrene matrixes. This advancement in material processing is a key

enabling tool, which may lead to a new era by providing nanosturctured composite materials with large third-order optical nonlinearity. The β value of CdS we obtained is 788cm/GW, and this TPA coefficient is almost two orders of magnitude greater than that for bulk CdS. The thin film preparation method is very general and can be adapted to other kinds of semiconductor quantum dot material. We also used our technique for CdSe QD capped with reverse micelle, and we observe the β value of 304cm/GW.

Second, we used numerical technique, previously developed by Professor Potasek, to investigate hybrid two-photon processes and multi-pulse trains. Many of the chromophores with large two-photon absorption are hybrid materials in which the two-photon absorption is coupled to an excited state absorption. This coupling makes the detailed analysis of the photophysics much more complex. Professor Potasek's numerical method agrees very well with published results. We also examined the details of the carrier dynamics for femtosecond pulses, which also are also in agreement with experimental results.

Acknowledgement

First of all, I would like to thank my advisor Professor Mary Potasek for her great guidance and many helpful discussions. Every time, before we start a new research topic, she would help me to understand the expected standards of achievement and likelihood of success in this area. She showed me in which direction my research could go but always left me enough room to choose my way based on my own interest. Prof. Potasek provides effective guidance so that I can maximize the ability.

Besides, I would like to thank Prof. Samir A. Ahmed, my Co-mentor. Professor Roger Dorsinville, and Professor Ardie D. Walser also give a lot of help. I would like to thank for their many advices and valuable discussions. In particular, I will also thank my wife, Jing, for her support and care.

Table of Contents

List of Tables

List of Figures

Chapter 1 Introduction and Brief Review of Nonlinear Quantum Dots Materials

1.1 Introduction

As more intense lasers are developed, the requirements for novel optical material increase. High performance, all optical switches for future use of optical communication, optical computer chips, optical filters, saturable absorbers,, and amplifiers are all possible applications of these materials. Scientists have moved their attention to hybrid nanometer size organics-inorganic materials, in many fields, such as chemistry, biology, physics and material science. The origin of term "nanotechnology" was first used in the 1970s. At the beginning, no one ever knew how it was going to change the world. "Nanoparticles" typically refers to the quantum confinement effect, and the size of Nanoparticles should be small enough to show the quantum confinement property [1]. A quantum dot is a three-dimension semiconductor crystal with a diameter of a few nanometers. Quantum wires are confined in 2D and quantum wells are confined in 1D. In the nanoregime, the electrons can overcome the barriers of bulk semiconductors, thus opening a whole new field.

Fig. 1-1 Quantum Dots

The latest development in nanoparticles research involves tuning dots in the Nanoworld. Researchers at Lawrence Berkeley National Laboratory discovered new methods to construct CdSe nanostructures and calculate their electronic states. They combined quantum dots and segmented nanorods into many branching forms. Scientists have formed new ways to calculate the electronic properties of these nanostructures. A disordered crystal structure with mere 10 atoms puts them under constant strain, which increases the stiffness of the particles by Gilbert and his colleagues. More interesting properties, such as strength, elasticity, and magnetism are showing up as researchers keep investigating the new structures and understanding of these nanoparticles. The deeper researchers go into the nanoscale, a new wide window with promising future applications spurs them to achieve even greater findings.. The optical properties are strongly dependent on the quantum confinement. For example, bulk CdSe (1.7eV) and CdS (2.55eV), are particular valuable because of the particular energy band-gaps. We want to tune particle sizes, and design special optical properties in the interested energy band. Therefore, we would shift the optical absorption and emission across the visible and UV range. For instance, CdSe QD materials have very good Photolumenescent property [1]. A large range of Dot sizes, 1nm to 13nm [2], make these nanoparticles have a large emission range. The fast electron-hole part recombination time as small as a few femtoseconds, is also a good feature for future nano-transistor.

The Nonotechnology may have significant impact on people's lives. For example, it could help extend the lifetime of different kinds of materials, reduce costs, improve

medicine, computer device, even the normal communication device. In nano-opto-electronics, the new nanometer memory chips and transistors have already been on the market with less power usage. All these new features come from the new material structure.

Potential applications have spurred the development of a large variety of synthesis techniques for semiconductor nanocomposites [2-7]. As intense laser have developed, scientists are also looking for novel materials with large nonlinear optical properties. For example, the super fast optical switch requires a high value of nonlinear refraction (n_2) and low two-photon absorption. Currently, there is no material that has the ideal property. Consequently, scientists are investigating nanomaterials. Recent theoretical studies [8-9] predict enhanced nonlinear susceptibility for nanoparticles, but there is no experimental data supporting this theory. There are a several papers [10-13] that show the same order (or less) of magnitude of the optical nonlinearity as that of bulk material.

We are interested in materials with novel two-photon absorption, which have one or two orders of magnitude increase in TPA over present materials. Currently, the β values of nano-materials are too small for significant applications. For example, I. Gerdova reported the nonlinear absorption coefficient β varied from 0.2 to 10cm/GW for different wavelengths [10].

1.2 Motivations for this work

We synthesize and investigate new nanocomposite materials, which may have

novel NLO properties in the visible and near IR spectral regions. We focus on the real and imaginary parts of the third order nonlinear susceptibility of semiconductors (CdS and CdSe) whose band gap energies fall in the spectral region of interest. Changing these materials will change the resonances to either longer (e.g. mid to far IR) wavelengths or shorter (e.g. ultraviolet) wavelengths depending on the band gap.

The nonlinearity of the semiconductor nanoparticles by themselves is not high enough for potential applications. The largest β value I found in CdS nanoparticles is 10 cm/GW [10], and others are even smaller such as [10-13]. Hence we need more advanced nanocomposite materials. We have investigated organic-semiconductor nanostructures because theoretical predictions indicate that novel excitons may be formed in these structures. Materials with large optical non-linearity in the VIS/IR regions may have many applications, such as optical communications (e.g. optical switches) and laser hardening (e.g. optical filters and optical limiters). Both the real and imaginary parts of the non-linearity are subjects of interest. The real part gives rise to self-focusing or self-defocusing depending on the sign of the non-linearity. The imaginary part is really what we are especially interested in, which gives rise to two-photon absorption.

The two-photon effect is well-known. When two low-energy long-wavelength photons strike a molecule at the same time, they have the same effect as one photon of half the energy. To make this process work, however, a very strong intensity is needed. Many of the chromophores with large two-photon absorption are actually hybrid materials in which the two-photon absorption is coupled to an excited state absorption

as shown in Fig.1-2

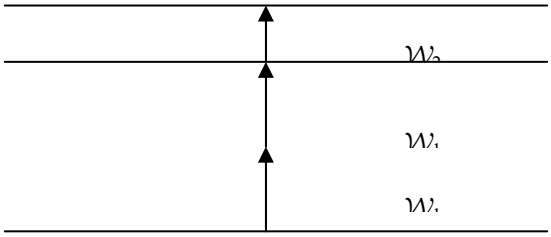

Fig. 1-2 Two-photon absorption energy levels followed by an excited state absorption

When the low intensity light passes these kinds of material, it goes through with very little linear absorption. The novel material with strong two-photon absorption will let the low intensity go though, but substantially reduce light at high intensity..

For example, we use the new material with strong two-photon absorption to protect optical sensors.

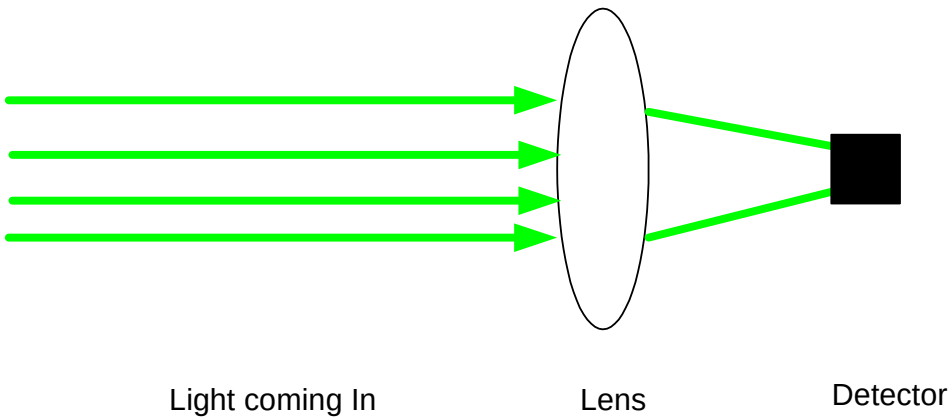

Fig. 1- 3 The detector without protecting filter

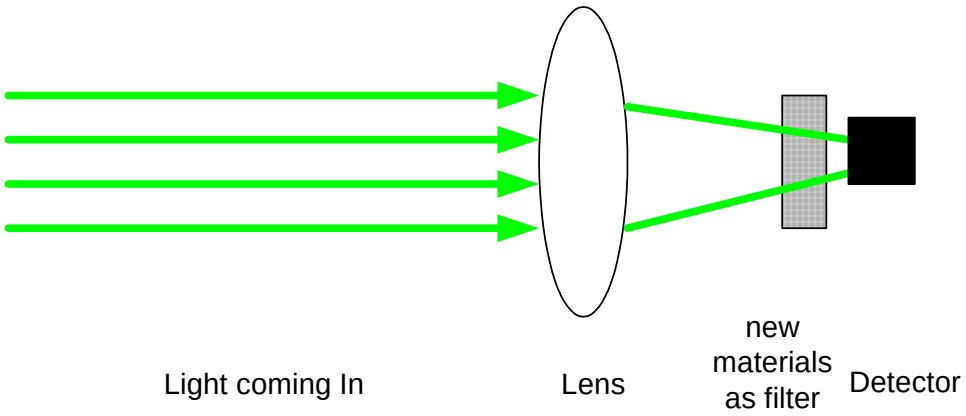

Fig. 1-4 The detector with protecting filter

The detector is a very sensitive device, and it would be damaged by the strong intensity laser light in Fig. 1-3. In Fig. 1-4, the new material could cut off the high intensity instantaneously when the intensity is over some certain threshold. Since the two-photon absorption is depends on I^2, the low intensity light could always reach the detector without breakdown.

The aim of this work is to synthesize the novel structures that combine both organic and semiconductor material and provide very strong two-photon absorption properites. We need to find the way to form the optical thin film, and characterize their nonlinearity. Additionally, the new organic and semiconductor material also needs to provide the necessary stability and processability for these important applications.

1.3 Nonlinear Optics

Nonlinear optics is the study of the interaction of intense laser light with matter. The field of nonlinear optics started in 1961, and the interest in this field has grown continuously. When laser light propagates through matter, its high intense electrical and magnetic field induces the motion of the charged components in the material. The

bound charges start to oscillate in the applied electrical magnetic field. The strength of this oscillation is dependent on the applied electric field and the polarization of the materials [14].

In the linear optics, the low applied electric field can only slightly change the material polarization. The proportional induced polarization is linear with the electric field E

$$P=\chi^{(1)}.E \tag{1-1}$$

where $\chi^{(1)}$ is known as the linear susceptibility. In nonlinear optics, the applied electric fields are high; therefore the higher order of the polarization can not be ignored. The polarization P(t) as a power of applied field strength E(t) as

$$P(t)=\sum_i \chi(i)E(t)^i \tag{1-2}$$

$$P=P^{(1)}+P^{(2)}+P^{(3)} \tag{1-3}$$

where E(t)= E *exp(-wt) + c. (1-4)

χ(2) is the second-order susceptibility and χ(i) is the *i*th-order susceptibility of the medium. The first term is the linear refraction and absorption. The second-order suscepibility is very useful for frequency doubling and optical switching, but only occur in noncentrosymmetric crystals, such as KDP.

Second-Harmonic Generation

$$\begin{aligned} P(2)(t) &= \chi^{(2)}[E_1^2 e^{-2i\omega_1 t}+E_2^2 e^{-2i\omega_2 t}+2E_1E_2 e^{-i(\omega_1+\omega_2)t} \\ &+2E_1E_2^* e^{-i(\omega_1-\omega_2)t}+c.c]+2\chi^{(2)}[2E_1E_1^*+E_2E_2^*] \end{aligned} \tag{1-5}$$

Third-order Polorization and Third-Harmonic Generation

$$P(3)(t)=\chi^{(3)}.E(t)^3 \tag{1-6}$$

For simplification purpose, let's use the monochromatic field

$$E(t) = E\cos\omega t \tag{1-7}$$

$$\mathrm{P(3)(t)} = \frac{1}{4}\chi^{(3)}.E^3\cos 3\omega t + \frac{3}{4}\chi^{(3)}.E^3\cos\omega t \tag{1-8}$$

The imaginary part of the susceptibility gives rise to the coefficient for two-photon absorption (β) and is given by

$$\beta = \frac{3\omega_0}{4n_0 c}\mathrm{Im}(\chi^{(3)}) \tag{1-9}$$

The real part of the susceptibility gives rise to the coefficient for the nonlinear index of refraction (n2) and is given by

$$n = n_0 + n_2\frac{|E|^2}{2} = n_0 + \gamma I \tag{1-10}$$

Where n_0 is the usual linear refractive index, n_2 is the nonlinear refractive index.

$$n_2 = \frac{12\pi^2}{n_0^2 c}\mathrm{Re}(\chi^{(3)}) \tag{1-11}$$

1.4 Quantum Confinement and Quantum Effects

1.4.1 Exciton and Semiconductor Quantum Dots

The property of a novel hybrid exciton formed by combining the "localized" Frenkel exciton with a "delocalized" Wannier-Mott exciton has been of considerable recent interest [15]-20]. The Frenkel exciton is the excited electronic state with the electron and the hole situated in the same molecule or atom. The Frenkel excitons have small radii and very large oscillator strength. In contrasts, being a pair of electron and hole in the semiconductors, the large-radius Wannier-Mott exciton in semiconductors is

relatively weakly bound due to typically large electron-hole distance. The interaction between Wannier-Mott excitons is very important while their oscillator strength is rather weak. The Wannier-Mott exciton wavefunctions overlap each other to get the exciton resonance, so the optical nonlinearity of Wannier-Mott exciton can be large at rather low density. These differences between the Frenkel excitons in organic materials and the Wannier excitons in semiconductors suggest forming systems, which have a hybridization of both the excitons. By combining an organic material and a semiconductor in one heterostructure system, an excited state is expected to have major properties of both kind of excitons and can overcome the limitation of each kind of excitons.

Fig. 1-5 (a) Wannier exciton in typical semiconductor with binding energy ~10meV, radius ~100Å (b)Frenkel exciton in typical organic materials with binding energy ~1eV, radius ~10Å

When semiconductor quantum dots are placed in a three-dimensional lattice, the excitons in nearest-neighbor quantum dots interact with each other due to multipole interaction. This interaction allows the presence of a "transfer Wannier-Mott exciton " propagating through the lattice. When such a lattice is put in an organic host, this

transfer Wannier exciton is coupled with the Frenkel exciton of the organic medium and at resonance of the two excitons, a new hybrid exciton appears in the system. The mixed state has a large exciton radius, large oscillator strength and very large optical nonlinearity. The lattice configuration allows tuning the optical properties and resonance regions as well as the value of the nonlinearity by controlling the dot radius, the spacing between the dots, and the semiconductor material (Assuming the ideal array with dots of the same radius R and the same dot –dot spacing d [20]).

A free exciton is a bound electron-hole pair that has a binding energy of a few meV. If optical excitations are of sufficiently high frequency, they impart enough energy to ionize an electron previously in the valence band of the crystal. A vacant hole is left in the position where the electron was.

The excitation energy can be readily transferred from ion to ion because of the strong coupling. The e-h pair behaves as a single hydrogenic particle and can move through the crystal without requiring that the individual ions switch spatial position. As excitons which ar ot spatially bonund to a region smaller than their natural separation distance (Bohr radius) are free to move about the crystal. For the free exciton scenario, it is more appropriate to think of the e-h pair as not being localized at all.

There is a non-negligible amount of negative Coulombic attraction between the electron and its associated vacancy. Although free excitons are free to move arond the crystal as e-h pairs, (as long as sufficient optical excitation continues) the electron and hole will both be both mutually bound.

There is a natural spatial e-h separation preferred by the system [21].

This may be calculated by balancing the centripetal force on the electron to the coulombic attraction force.

$$\frac{m_0 v^2}{r_{ex}} = \frac{q^2}{4\pi\varepsilon_0 r_{ex}^2} \tag{1-12}$$

The Bohr postulate angular momentum L may be expressed mathematically as

$$m_0 v r_n = n\hbar, \tag{1-13}$$

We have $r_{ex} = \frac{k\varepsilon_0 \hbar^2}{m_{re} q^2}$, (1-14)

where m_{re} is the reduced effective mass ($1/m_{re} = 1/m_c + 1/ m_v$), m_c and m_v are the conduction band and valence band effective masses), q is the the electronic charge, ε_0 is the permittivity of free space and r_{ex} is the spatialseparation of the electron and hole. The dielectric constant k scales ε_0 to account fro the fact that the electron and hole interact through an attractive Coulombic force which is screened by the dielectric constant of the crystal. For CdS, k is ~ 8.5. Using the Bohr's hydrogenic model, it follows that excitonic bound state is given by 1-14

$$E_{ex} = \frac{q^2 / k\varepsilon_0}{2a_0^*} = \frac{m_{re}}{m_0}\frac{1}{(k\varepsilon_0)^2}\frac{q^2}{2a_0} = 13.6\frac{m_{re}}{m_0}\frac{1}{(k\varepsilon_0)^2}(eV) \tag{1-15}$$

where m_0 is the electron rest mass, and a_0 is the Bohr radius ($a_0 = \frac{\hbar^2}{m_0 q^2}$). For this model to be valid, r_{ex} should be large in comparison to the lattice constant of the host material. Semiconductors,posses relatively small effective masses and large dielectric constants (if compared to insulators). Hence it is reasonable to assume that

the requirement is satisfied.

The importance of the excitonic Bohr radius is that it provides a threshold value below which the confinement regime becomes relevant. That is, an exciton in a nanoparticle will not experience confinement if the spatial dimension is larger than that of its own preferred electron-hole spatial separation. Confinement energy will not impact to energy levels available to the exciton unless the e-h spatial separation is reduced below the excitonic Bohr radius. Below this threshold value begins the exhibition of quantum sizing freatures, such as distinct variation of density of states with nanocrystal size. Materials such as cadmium sulfide are particularly good for observation of quantum size effects at relatively large nanocrystal sizes – nearly an order of magnitude larger than that of silicon or cadmium selenide. Thus cadmium sulfide is a very good candidate for the purpose of observation of quantum size effects, and its excitonic Bahr Radii is 315 À.

1.4.2 Quantum Dots Sizing Effects

One of the most interesting properties of semiconductor nanocrystals is the distinct large-magnitude change in their optical properties as a function of nanoparticle size. Optical activity is concentrated to a few transitions, resulting in an enhancement in nonlinear optical effects. The change in the density of available electronic states is understood by initially considering Heisenberg's uncertainty relationship between momentum and spatial positioning of both free and confined particles.

$$\Delta p_x \Delta x \geq \frac{\hbar}{2} \tag{1-16}$$

For a free particle or a particle confined to a periodic potential, the energy and the momentum $\hbar k$ may be well-define, but the particle position is not defined. From the Schrodinger equation, energy eigenvalues are produced through the Hamiltonian operating on the wavefunction. There energy eigenfunctions of the particle can be viewed as superpositions of k states associated with the bulk.

For a free particle, the energy dependence on wavevector k is quadratic [22].

$$E = \frac{\hbar^2 k^2}{2m} \tag{1-17}$$

1.4.3 Coulombic Attraction

Quantum confinement results in a blue shift in the location of the density of states when the nanocrystal size is below their corresponding excitonic Bohr radius. The energy shift is proportional to $1/r^2$. The most important is the exciton's electron-hole coulombic attraction potential. This makes the energy of the nanocrystal proportional to 1/r.

The Hamiltonian of the excitonic bound state is approximately described by the hydrogenic model [23]:

$$\hat{H} = -\frac{\hbar^2}{2m_h}\nabla_h^2 - \frac{\hbar^2}{2m_e}\nabla_e^2 - \frac{q^2}{\varepsilon|r_e - r_h|} \tag{1-18}$$

where $|r_e - r_h|$ represents the e-h pair separation and m_e and m_h are the electron and hole effective masses. Assume the smaller r, wavefunction will take the following

form:

$$\psi_n(r) = \frac{C_n}{r}\sin(\frac{npr}{R}) \tag{1-19}$$

The energy of the lowest excited state then becomes:

$$E = \frac{\hbar^2\pi^2}{2R^2}[\frac{1}{m_e} + \frac{1}{m_h}] - \frac{1.8q^2}{\varepsilon R} \tag{1-20}$$

As the QD radius decreases, the bandgap increases.

For example, we calculate the CdS nanoparticles at wavelength 340nm, and the band gap rise up to 3.56eV.

1.5 Picosecond Laser Experiment Setup

The picosecond system is a Continuun passively and actively mode-locked Nd:YAG oscillator. The compact optical bench has three main stages: an oscillator, an amplifier, and a harmonic generator. In the oscillator, a single flashlamp pumps, an Nd:YAG rod that emits light at the fundamental 1064nm. A passive mode-locking dye solution on the end mirror allows for the power build up in the cavity and pulsing. The system is enhanced by the active mode-locking system made of an acousto-optic modulator. A Marx board is driven electro-opticl Pockets cell triggered by a photodiode, a pulse selector. The photodiode senses for intensity buildup inside the cavity, sends a trigger signal to the Marx bench board which applies a 4KV voltage to the pockek cell, change the polarization of the pulse. The pulse is sent to the amplifier after extracted from the oscillator.

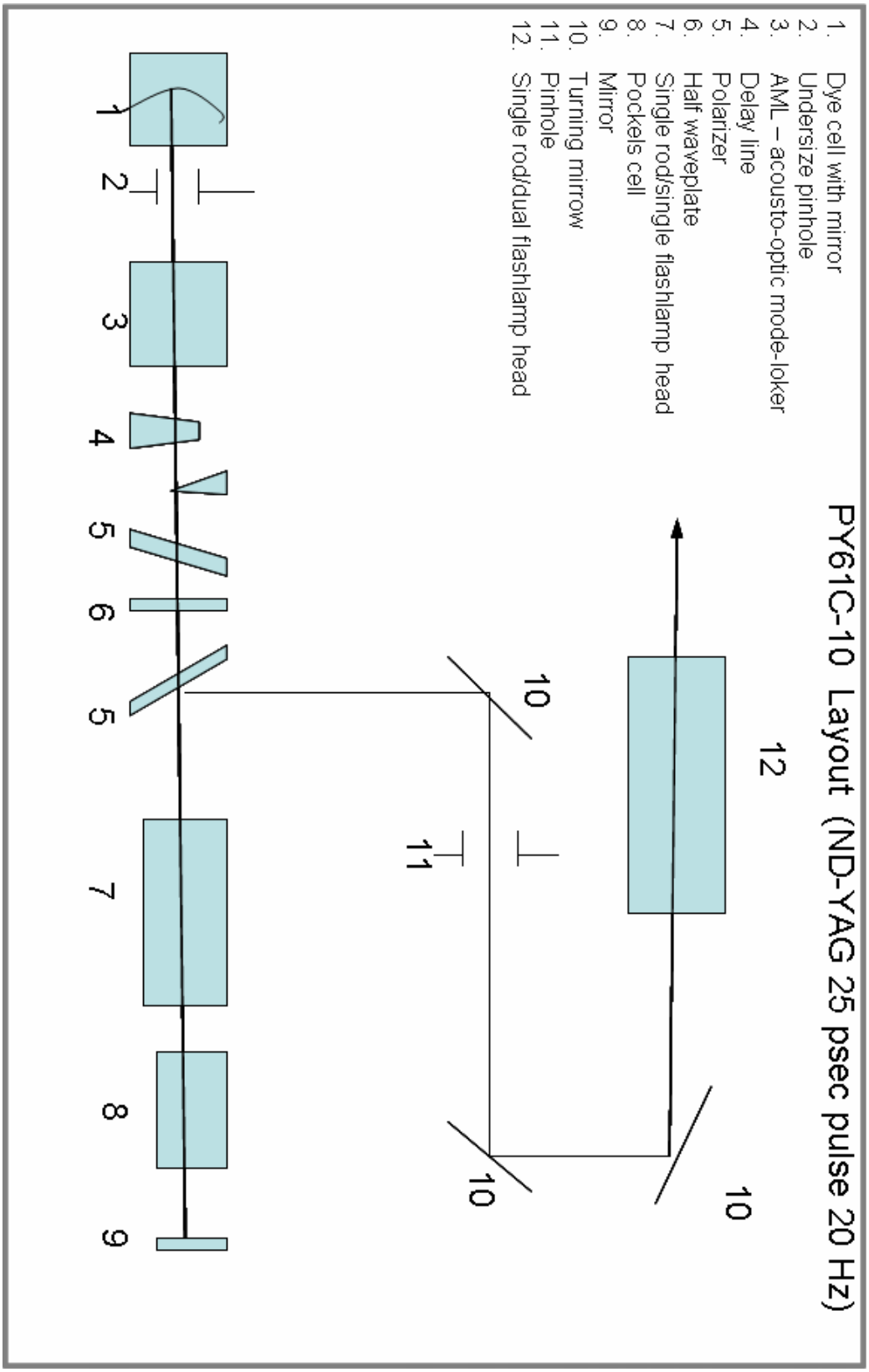

Fig. 1-6 The PY61C-10 Picosecond Laser Layout

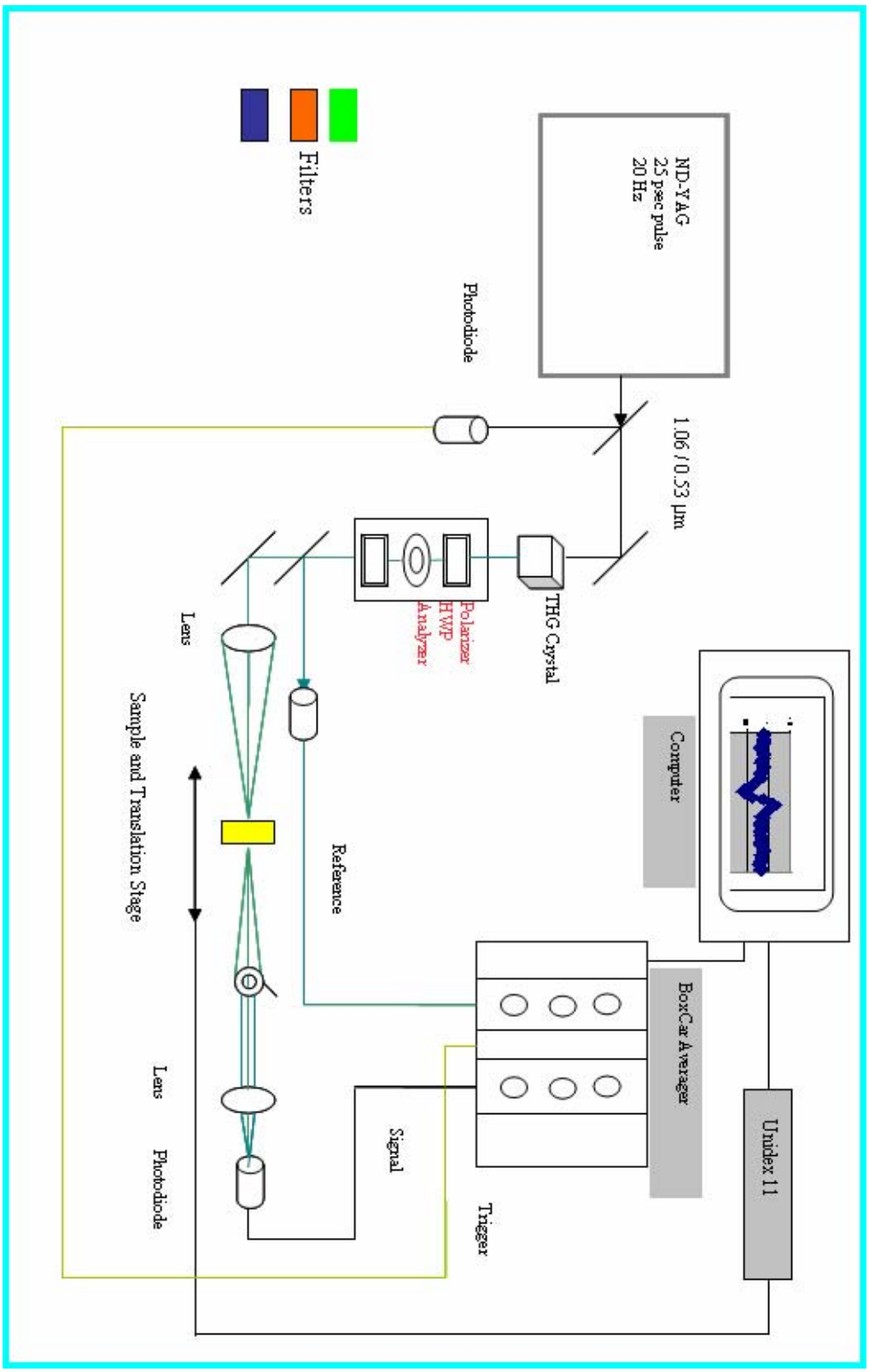

Fig. 1-7 Z-scan Setup

1.6 Transmission Electron Microscopy

In the nanostructure study, Transmission Electon Microscopy (TEM) is the most important instrument of investigation. It helps us to directly study the nanoparticle shape, size, and their organization structure. TEM has the capacity to provide real space imaging at a very high resolution of a few À. It can show a lot of detail view inside the material, which helps in understanding the properties.

1.6.1 TEM Schematic Structure

In each instrument, illumination from the source (lamp, filament in the electron gun) is focused by the condenser lens onto the specimen. A first magnified image is formed by the objective lens. This image is further magnified by the projector lens onto a ground glass screen (light) or fluorescent screen (electrons). The magnification system can give a magnification of 250,000. To study the CdS in dendrimer G4, G5 and G6, I used the Zeiss EM 902.

1.6.2 The Zeiss EM 902

Fig. 1-8 Zeiss EM 902

The Zeiss EM 902 is an 80 kV thermionic transmission electron microscope (TEM) with a maximum line resolution of 0.34 nm and a point resolution of 0.5 nm. It operates in normal, diffraction, or low dose modes at either 50 or 80 kilovolts. Its magnification range is 150x to 250,000x, but it performs best at 7,000x to 140,000x. In the Spring of 2005, this microscope was upgraded with a MegaView III - iTEM image acquisition system. This new system can acquire images at a maximum pixel resolution of 1376 x 1034. Images may also be taken on film (Kodak SO-163).

1.7 Perkin Elmer LS 50 Luminescence and Absorption Spectrometer

1.7.1 Perkin Elmer LS 50 Luminescence Spectrometer

Fig. 1-9 LS 50 Luminescence Spectrometer

Florescence is a short lived emission that usually occurs within 10^{-9} to 10^{-7} seconds of the sample being excited. When operating in the fluorescence mode two gating periods occur. During the first gating the instrument integrates the excitation and emixxion photomultiplier signals. This is followed by a second gating period, which occurs shortly before the next flash and integrates the dark current signal (the signal produced when no light is falling on the photomultipliers). The value obtained from the second gating is subtracted from that obtained from the first gating to produce a value that represents the signal free from dark current contribution and long-lived luminescence emission.

Perkin Elmer LS 50 Luminescence Spectrometer consists of a spectrometer

unit connected to a computer. At the front of the Model LS 50 is the sample compartment, which is hinged on the underside. The compartment can be opened by using the finger grip on the top of the compartment to pull the cover down. The sample dells are located in the sample compartment and different sampling accessories can be installed in this area. Also within the sampling area are two sockets used for controlling accessories that are electrically operated.

1.7.2 Lambda 19 Spectrometer

Fig. 1-10 Lambda 19 Spectrometer

The Lambda 19 is a high performance, PC-driven spectrometer. The 'UV' version operates in the ultraviolet (UV) and visible (IVS) spectral ranges, while the 'NIR' version extends to the near infraired (NIR) spectral range. The Lambda 19 Spectrometer is of modular design, permitting you to arrange the modules

ergometrically according to your preferences. The sample compartment is generously proportioned and can accommodate a wide range of sample handling accessories. An interesting feature is the ability to remove the entire sample compartment to permit the installation of future specialized accessories.

The detector compartment houses the detector assembly. This compartment may be regarded as a second sample compartment, since the standard detector assembly can easily be removed to permit the installation of special sample handling accessories thant incorporate their own optics and detectors. The Lambda 19 spectrometer features an all-reflecting, double-mono-chromator optical system. The optical components are coated with silica for durability. Holographic gratings are used in each monochromator for the UV/VIS range.

Later I will show a lot of UV absorption figures. All those solutions are contained in 1mm cell, and the absorption measurements are really the optical density measurements.

1.8 Thesis overview

This section summarizes the whole thesis structure. The first chapter presents the basic definitions of nonlinear optics and describes the measurement devices. The description of the quantum confinement of the systems we studied is in the first chapter. It is related to the synthesis of quantum dots materials we presented in the Chapter one also. After that, we start off with a brief introduction on the previous work and background research of all other chapter. At the end of Chapter One, we

introduce the measurement equipment. In Chapter Two, we discuss the synthesis method of the quantum dots CdSe and CdS in two kinds of reverse micelle systems, the preparation of two different thin films, and their linear characterizations. To analyze the nonlinear optical properties, we perform open aperture Z-scan technique and transmission measurements, which can give us the value of the imaginary part of the third-order nonlinear susceptibility. In Chapter Three, we give a detailed description of the Z-scan technique, which is used for the measurement of the imaginary part of the third order nonlinear susceptibility of the hybrid materials—CdS and CdSe. For CdSe capped with reverse micelles. We only use the z-scan technique to measure the two-photon absorption. We also perform the nonlinear transmission to find the TPA coefficient. In Chapter 4 and 5 we present the simulations. First, we demonstrate the simulation on effects of excited state absorption on two-photon absorbing materials in chapter 4. We describe the simulation theory, characteristics of population densities, and optical pulse shapes. Chapter 5 describes the optical pulse shape simulation of a train of multiple pulses. We preformed the carrier population redistribution, and calculated the pulse intensity and the pulse shape distortion.
In the last chapter, we give a short conclusion and future direction.

Chapter 2 Semiconductor Quantum Dots Composites

2.1 Introduction

Nanometer-sized semiconductor materials have attracted broad attention in the fields of physics, chemistry, and biology for their unique chemical and physical properties as well as their potential technological applications [1-6]. Nanometer-size crystals (NC) exhibit behavior intermediate between bulk material and molecules. These systems have received special attention mainly because of their unique size-dependent optical properties which include optical properties such as large nonlinearity.

Various approaches have been explored to pursue a simple and tunable synthetic route for II-VI semiconductor monodisperse NCs, including polymer and glass matrix host methods [7-8] and gas-phase [9-10], solid-state [11], and solution-phase syntheses [12-13]. Among these methods, it is well-established that synthetic routes utilizing colloidal assemblies as templates enable production of high-quality monodisperse semiconductors, metals, and metal oxide NC dispersions[7,12].

Here I describe the synthesis of mass-selected CdSe and CdS nanoparticles as well as the fabrication of a thin film consisting of surfactant-capped nanoparticles integrated in a processable polystyrene matrix under room temperature. I propose a novel system sonsisting of CdS and CdSe reverse micelles exhibiting with large nonlinearity, and we also provide a new method to improve the processability and stability of these materials while maintaining their important optical properties.

2.2 Surfactants, micelles and the reverse micelles-structure

2.2.1 Surfactants

Surfactants constitute the most important group of detergent components. The term surfactant is a blend of "Surface active agent" [14]. A surfactant is common defined as a material, which can greatly reduce the surface tension of water when used in very low concentrations. Surfactants reduce the surface tension of water by adsorbing at the liquid-gas interface. Surfactants are usually organic compounds that are amphiphilic, and they have so called “tail and head”. The “tail” refers to that they contain hydrophobic groups, and the “heads” refers to the hydrophilic groups.

The surfactants are widely used in the farming industry. For examples, A very low-concentrate surfactant solution help pesticides stick to and completely cover vegetation allowing them to work efficiently. Another most common surfactant which is used in everyday living is detergent. They clean poorly soluble hydrophobic material, making it (oil and grease) easier to remove from the surface.

Here are some commonly used surfactants [14].

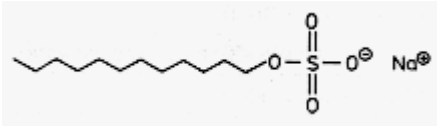

Sodium dodecylsulfate (SDS)

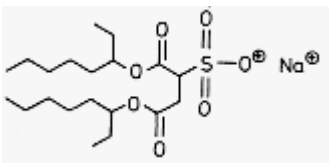

Bis(2-ethylhexyl)sulfosuccinate Sodium salt

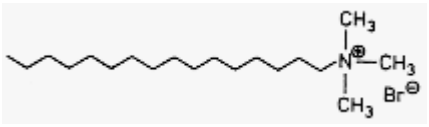

Cetyltrimethylammoniumbromide (CTAB)

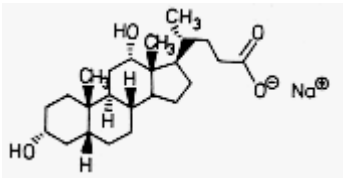

Sodium deoxycholate (DOC)

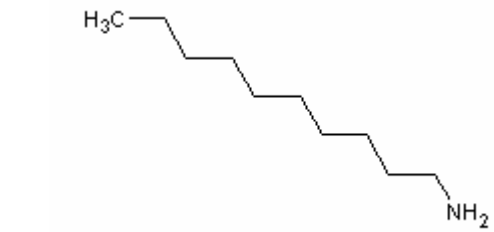

Decylamine

Fig. 2-1 Most often used surfactants

2.2.2 Micelles

Micelles are aggregates of surfactant molecules dispersed in a liquid colloid. A typical micelle in aqueous solution forms a roughly spherical or globular aggregate with the hydrophilic "head" regions in contact with surrounding solvent, sequestering the hydrophobic tail regions in the micelle center [14].

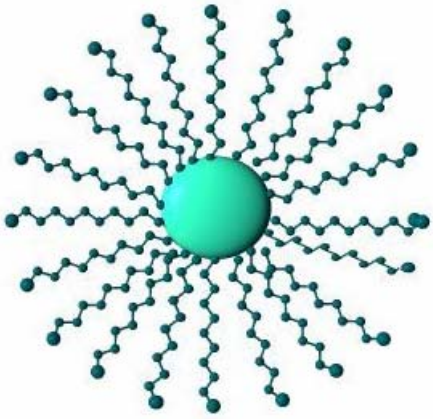

Fig. 2-2 Normal Micelles Structure

There are several conditions in which micelles form. First, if the concentration of surfactant is bigger than the critical micelle concentrations (CMC) [14], hydrophobic effects drive micelle to form in water. Second, if the temperature of the system is greater than the critical micelle temperature, micelles form spontaneously.

2.2.3 Reverse Micelles

Reverse micelles [14], are formed by dissolving the surfactant in an organic solvent and a limited a mount of water to produce a macro-homogeneous solution. In a nonpolar solvent, the exposure of the hydrophilic head groups to the surrounding bulk solvent is energetically unfavorable. Therefore the hydrophilic groups tend to be sequestered in the micelle core and the hydrophobic groups remain solvent-exposed on the surface of the micelle. These reverse micelles are extremely difficult to form from surfactants with charged head groups, since hydrophilic sequestration would create highly unfavorable electrostatic interactions. By varying the amount of water, surfactant, and organic solvent, micelle capped semiconductor quantum dots system

will vary too. When the surfactant is kept at a constant concentration, increasing the water content will increase the volume of the reverse micelles. On the other hand, keeping the amount of water the constant, but increases the surfactant concentration and decease the size of the micelles [15].

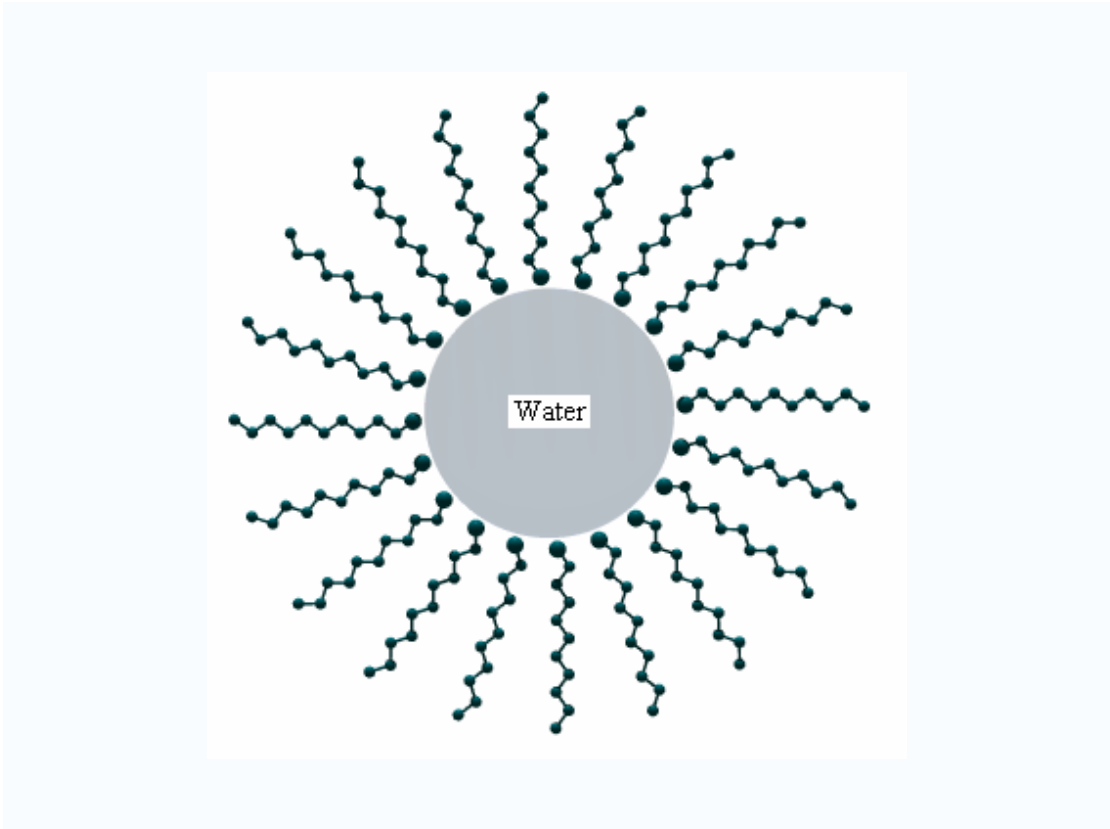

Fig 2-3. Reverse micelles

2.2.3.1 The absorption spectrum of reverse micelles

In our system, we use reverse micelles as blocking media, which can prevent the nanoparticles from growing into aggregates. For example, in nanoscale hydrophilic cavities, reverse micelles are widely used in the synthesis of semiconductor and other nanoparticles [15-23]. In micelle-capped cadmium sulfide (CdS) nanoparticles [16, 23], quantum confinement effects on the band gap absorption have been extensively studied [24-31]. However, we have found that the absorption properties of CdS

nanoparticles also depend on the particular synthesis. . In addition, we found that the wavelength of the linear absorption of the reverse micelles is similar to that of the CdS QD material.

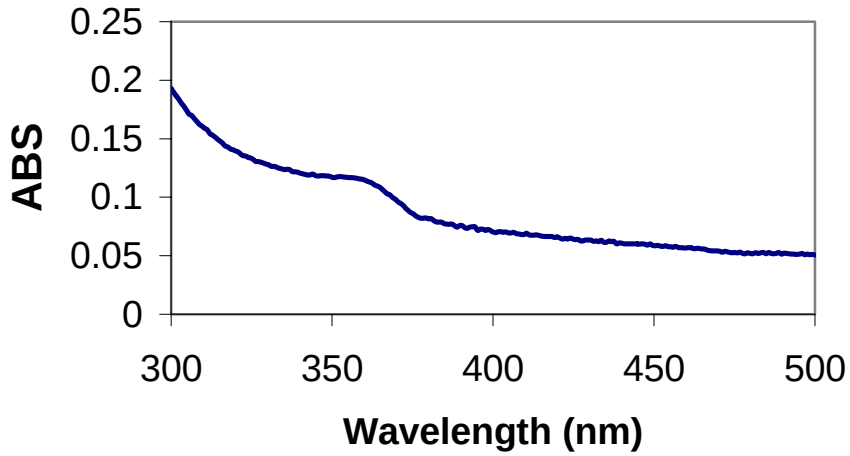

Fig. 2-4 Reverse micelles in toluene

The absorption shifts to the right with decreasing CdS particle sizes [24, 27-31].

2.3 Nanoparticles capped with Surfactant

In further effects to control semiconductor QD size and size distributions, capping methods using thiols or mercaptans have been developed [32]. For the size control, the capping agent to sulfur ratio chemically determines the QD size. Making colloidal suspensions of nanocrystallites by precipitation from solutions containing the elements, in general, are relatively cheap and efficient. Such colloidal crystallites grow by the addition of individual ions until one of those supplies is either depleted or removed. Consequently, by arresting the precipitation after a certain time, the size of the precipitate could be controlled in a range between 15 and about 500 angstroms.

Sizes within a single batch normally do not vary by more than 15 percent, although higher monodispersity has been demonstrated in various works [32].

In this area, the early work focused on colloidal synthesis with no effort to form composites [33-37]. The CdS nanoparticles capped with thiophenol [38-39] are used in X-ray diffraction and absorbance measurements, where they measured the ratio of capping agent to sulfur controlled QD sizes.

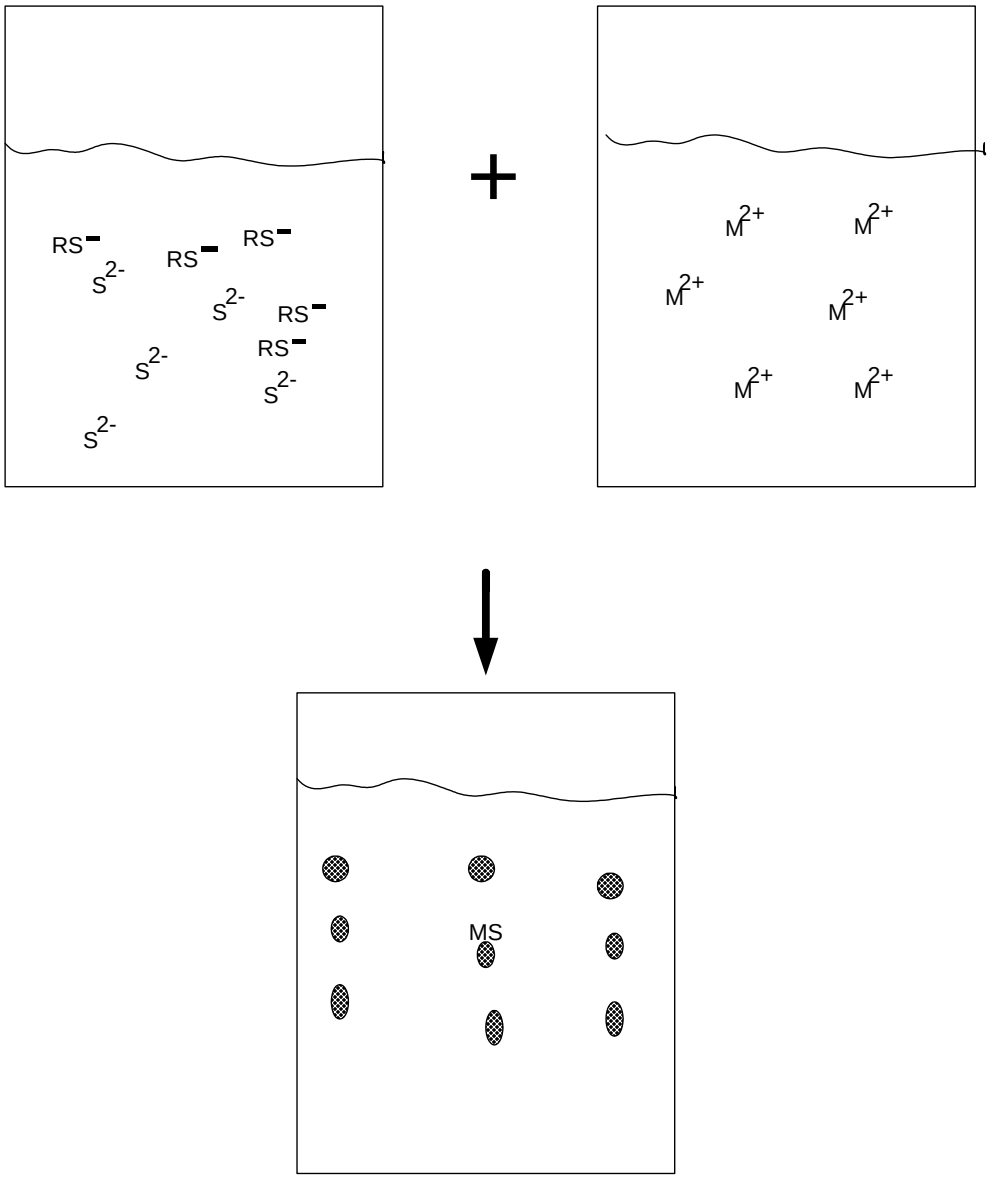

Fig.2-5 Schematic of nanoparticles capped with reverse micelles

RS^- is the capping agent. S^{2-} is the sulur, and M^{2-} is the metal ion.

Another strategy to form metallic nanocrystals and assemble them into a bulk-like array involves capping them – surrounding them – with organic molecules that will trap them at a particular size, and prevent two of them from getting close enough together to merge into a large particle via polar ionic interaction [40].

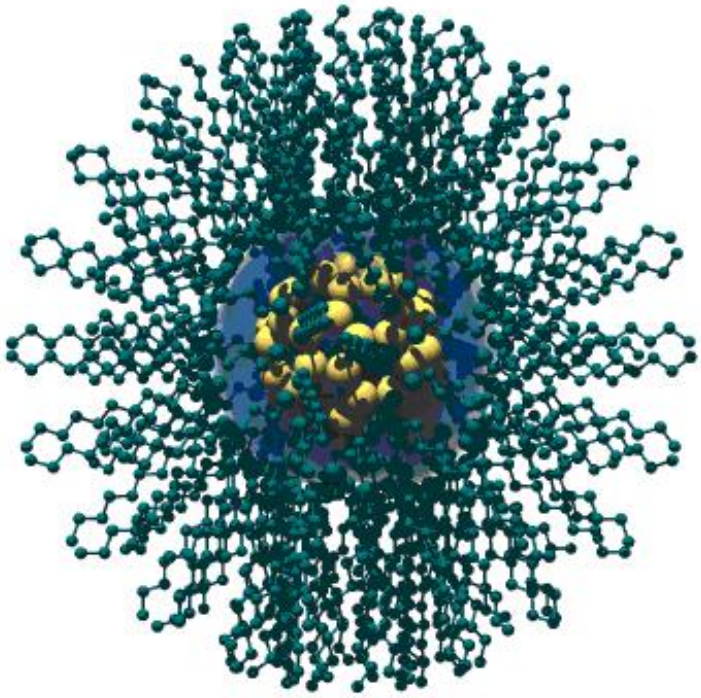

Fig.2-6 3D schematic of nanoparticles capped with reverse micelles

Majetich and Carter [41] reported the synthesis of colloidal CdSe capped with six different terminating ligands, and studied the surface effects. In this work, to prevent coalescence when extracting the quantum dots from the micelles, they were capped with ligands which bond to their surfaces. In order to minimize the differences other than at the surface, a single batch of colloidal CdSe was divided into six parts, and a different terminating ligand was added to each. The bandgap, absorption oscillator

strength and trapping time have no change by the surfaces test. However, the luminescence experiments were affected by the surfaces of those particles. Nonlinear optical measurements indicated that a very promising two-photon absorption (β values) ranging from 8.7 x10 $^{-6}$ to 1.2 x 10^{-5} cm/W. In our (CdS) experimental data, it is very close to these values. The brief overview of various approaches to fabrication is presented here, with greater detail to follow. It is now common practice for colloidal nanofabrication to include a passivating surfactant for enhancement. Many years ago, researchers used cadmium sulfide as a model materials to study the quantum confinement. Compared with other material, the quantum effects of CdS are more pronounced.

Many synthesis methods for producing CdS quantum dots have been studied. I list some significant results that have been obtained earlier with CdS [41-44].

The availability of a reliable semiconductor colloidal synthesis method which results in unique size, shape and surface is very crucial for the optical properties and a lot of applications. The strategy of keeping the particles small brought with it the concept of arrested precipitation, which made use of inverse micelles as nanometer-sized reactors, which can act as capping agent to prevent the uncontrolled growth and aggregation of particles. The choice of a suitable stabilizer can be considered a key point in advanced colloidal synthesis of semiconductor nanoparticles. Stabilizers regulate the growth rate and size of the nanoparticles, block them from oxidation and provide a dielectric barrier at the surface. As discussed previously, colloidal chemistry nanoparticle synthesis mechanisms are varied with regard to the specific chemical precursors

utilized, and temperature, pressure, etc conditions.

2.4 CdSe capped with reverse micelles

2.4.1 Introduction

We report three reverse micelles synthesis of CdSe nanoclusters in decylamine-toluene dispersion. We study those three groups of the solution absorption spectra and optical thin absorption spectra, and find the most stable CdSe QD size. The fabrication of a thin film consists of a polystyrene-toluene dispersion mixture. Nanoparticles of $(CdSe)_n$ are stable at n = 13, 19, 33 and 34 with structures distinctively different from the bulk fragments as reported previously [33]. From transmission electron microscope (TEM) measurement of a thin film deposited on carbon coated copper grid, we determined the diameter of these nanoparticles to be 2 nm. Measurements of optical absorption of the toluene dispersion give additional evidence that our sample contains stable mass-selected nanoparticles. The position of the sharp excitonic absorption band (i.e. 415nm, corresponding to $(CdSe)_{33,34}$) and the anticipated strong quantum confinement of the nanoparticles make this system a promising class of organic/semiconductor nanocomposite with large two-photon absorption (TPA) in the visible and near infrared for potential application in optical limiting.

2.4.2 CdSe Quantum dots Sample preparation

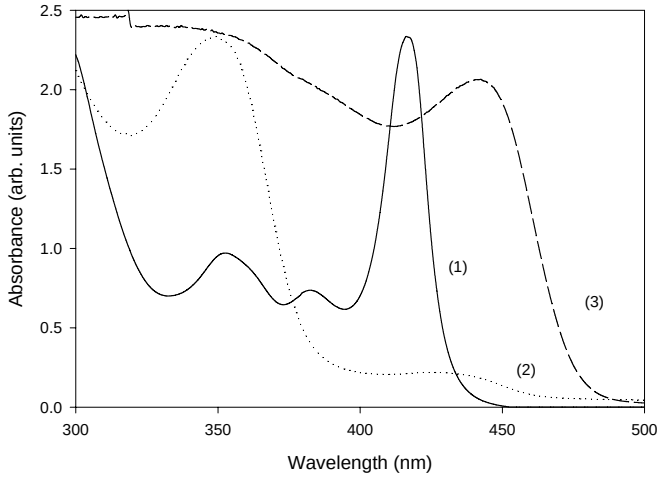

Fig.2-7. Optical absorption spectra.

Curve(1) corresponds to the sample prepared with [Na_2SeSO_3]=0.05M

curve(2) corresponds to the sample prepared with [Na_2SeSO_3]=0.9mM

curve(3) corresponds to the sample prepared with [Na_2SeSO_3]=0.01M

Micelle-capped CdSe NCs were prepared according to the procedure described in [45]. Briefly, cadmium nitrilotriacetate (CdNTA), obtained by dissolving 0.16g of $CdSO_4$ and 0.21g of sodium nitrilotriacetic acid in 10 ml of water, was mixed with 1.2 ml of decylamine ($CH_3(CH_2)_9NH_2$) as surfactant. The cadmium ions bind to the amine groups of the surfactant. The solution is further mixed with 15ml aqueous solution of sodium selenothiosulfate (Na_2SeSO_3) which dissociates in alkaline conditions to yield Se^{2-}.On adding toluene to this solution, the micelles move up into the toluene and transform into reverse micelles in which nanoparticles of CdSe form. By adding toluene onto the solution, the products come together to form nanoparticles in the

toluene (upper) side which turns to greenish yellow within 20 minutes, whereas the water (lower) side remains colorless. The total reaction yield is more than 20%.

In first curve of Fig.2-7, the absorption spectrum of the CdSe dispersion shows a sharp excitonic peak at 415nm together with smaller peaks at 382 nm and 352 nm, which are blue-shifted considerably from the bulk value at 680 nm. The main components of this sample are identified as $(CdSe)_{33}$ and $(CdSe)_{34}$. The smaller bands at 382 nm and 352 nm correspond respectively to the nanoclusters $(CdSe)_{13}$ and $(CdSe)_{19}$ as reported previously [45].

To investigate the different clusters, we further varied the concentration of Na2SeSO3, to form two other CdSe clusters. For a concentration of $[Na_2SeSO_3]$ =0.9mM, curve 2 in Fig.2-7, shows that the main product is the smaller nanoclusters, which is identified as $(CdSe)_{13}$. Under sufficient concentration of Cd^{2+} ion, the cluster $(CdSe)_{13}$ is the first cluster to be formed, and no other large particles are formed as shown in the absorption spectum. Under the same condition as above except that the concentration of Na2SeSO3 is increased to 0.01M, there is a very strong absorption peak at 450nm. The long flat absorption from 420 to 300nm in the third curve of Fig.2-7, indicates a wide range of QD distribution in the solution.

The concentration of the reagent sodium selenothiosulfate has been reduced in this preparation; therefore, the number of available Se atoms that can react is higher than in the previous case. From the three absorption spectrums, we observe that lower number of (CdSe) units exist in all the other QD solutions.

2.4.3 The absorption in water

The samples of CdSe nanoparticles have been prepared simply by mixing aqueous solutions, and separated by adding toluene to the mixed aqueous solution. After 20 minutes, the solutions are well separated. The upper part of the solution is toluene containing CdSe quantum dots, and the lower part of the solution is aqueous solution. Measurements of the absorption spectrum 500nm and 300nm, showed that the value of the absorption increased substantially (Fig. 2-8).

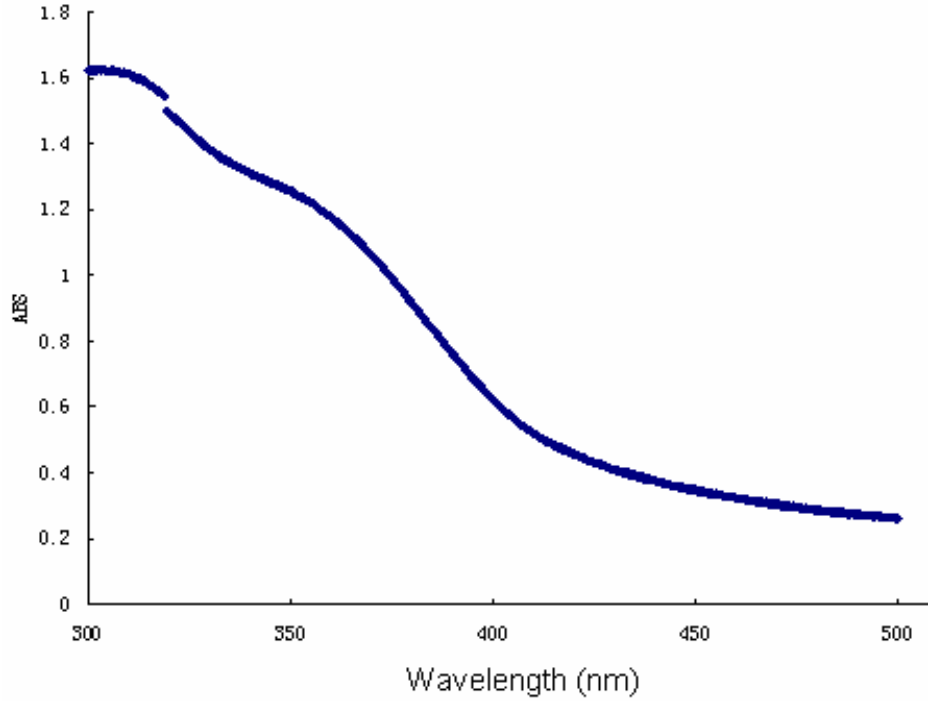

Fig.2-8 The spectrum absorption of the aqueous solution

2.4.4 CdSe TEM

The quantum dots size and shape were observed by TEM. Because the micelles may interfere with the electron transmission, the small quantum dots are very difficult to observe. Here we show two kinds of TEM image of CdSe solution, the small QD in

curve (1) and large QD in curve (3) in Fig. 2-7. In Fig.2-9, the QD size distribution is quite close. But in

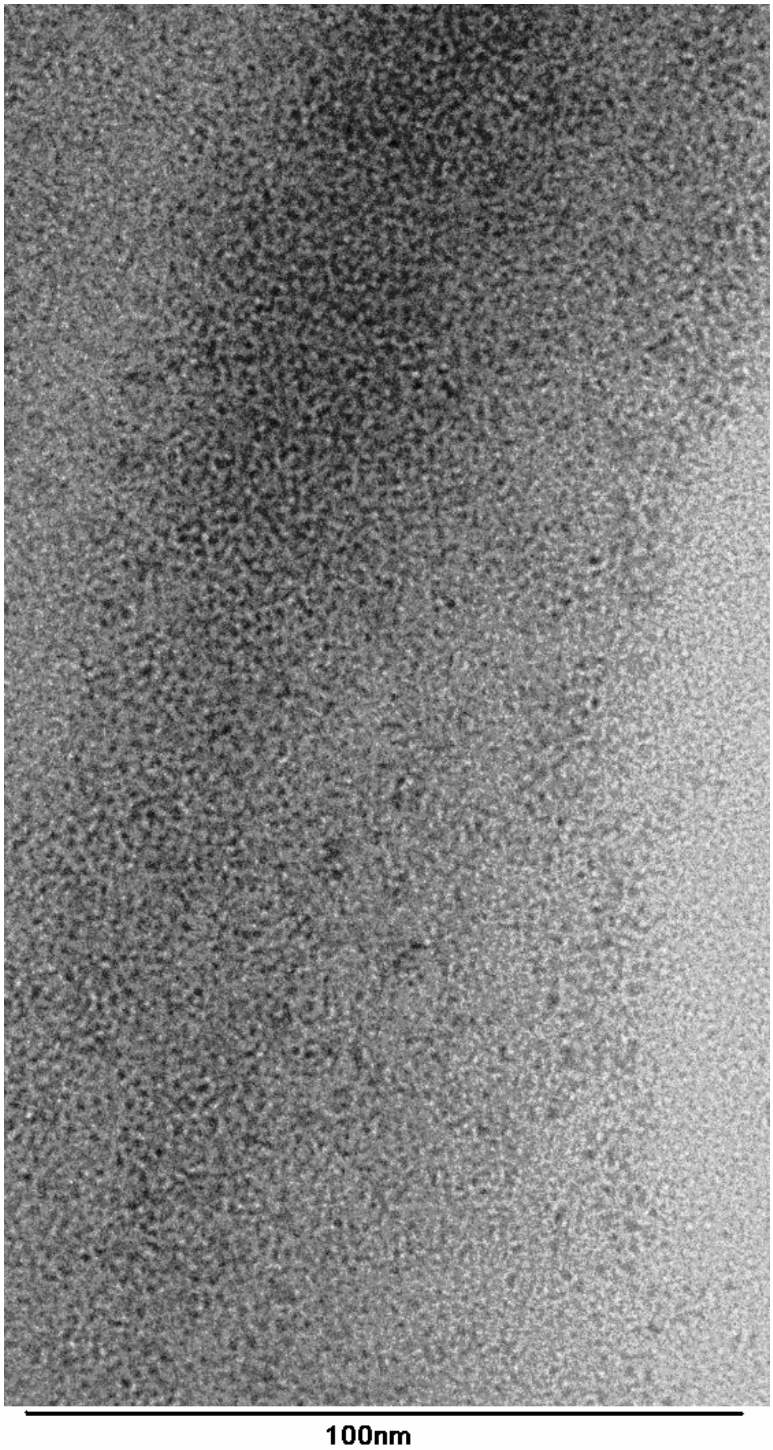

Fig. 2-9 High concentration CdSe TEM in Curve (1) solution

Fig.2-10, we observe a broad distribution, and each dot varies a lot. There are more nanorods in Fig. 2-10 than in Fig.2-9.

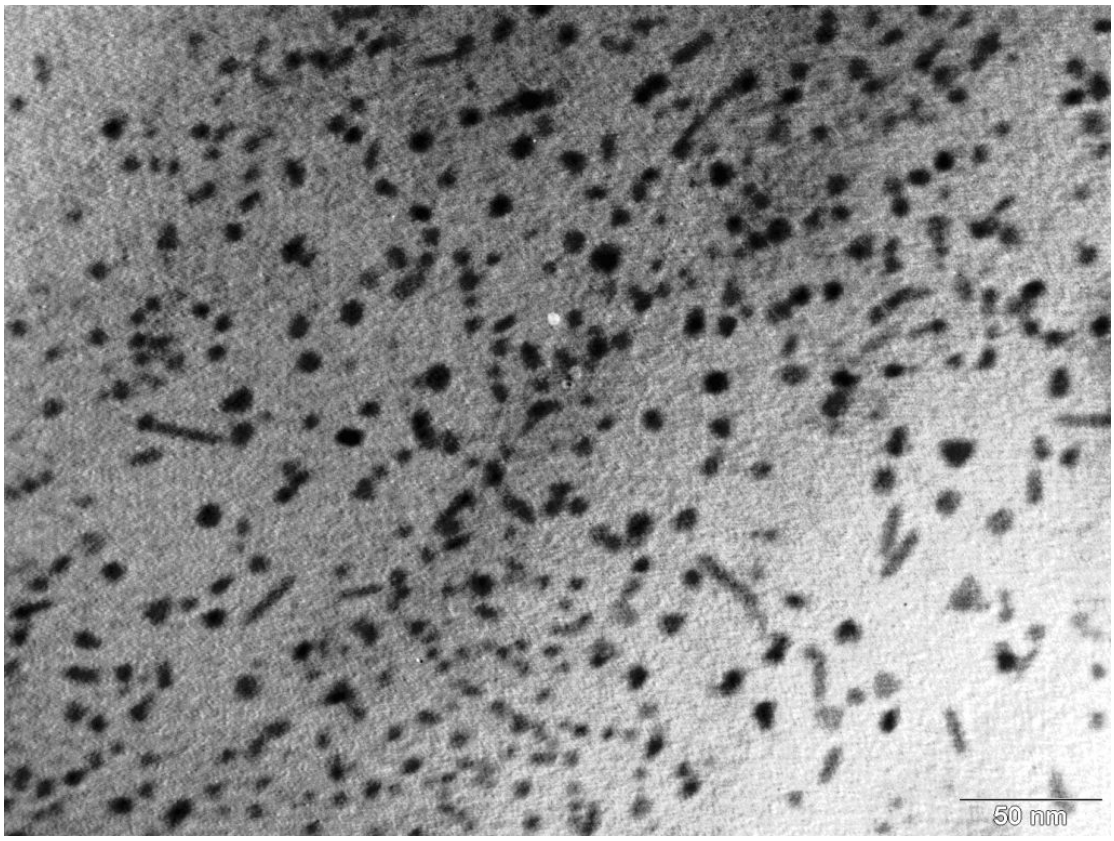

Fig. 2-10 Large size Quantum dots and rods in curve (3) solution

2.4.5 CdSe Film

Polymers provide a highly processible matrix compatible with various conducting and insulating substrates without the lattice matching required in semiconductor epitaxy. Unfortunately $C_{10}NH_2$-capped nanoparticles can hardly cover large areas in a homogenous way owing to their monodispersity and stability that are inferior to longer alkylamine-capped nanoparticles [46]. They can easily aggregate at the air/water interface and are difficult to form a uniform arrangement in large areas.

In our sample, the decylamine-capped CdSe nanospheres are assumed to be accommodated between the polymer chains. Two polymers (polystyrene, PS, and polymethylmethacrylate, PMMA) have been tested so far and absorption spectra have been taken to characterize the spin-coated thin films (inset in Fig.2-11). The toluene dispersion, after being optically characterized, was mixed with other toluene solutions containing a polymer matrix. Specifically, we used 70mg/ml polystyrene (PS) and 50mg/ml polymethylmethacrylate (PMMA). The single layer spin-coating process consists of the deposition of the polymer - surfactant-capped QDs toluene mixture.

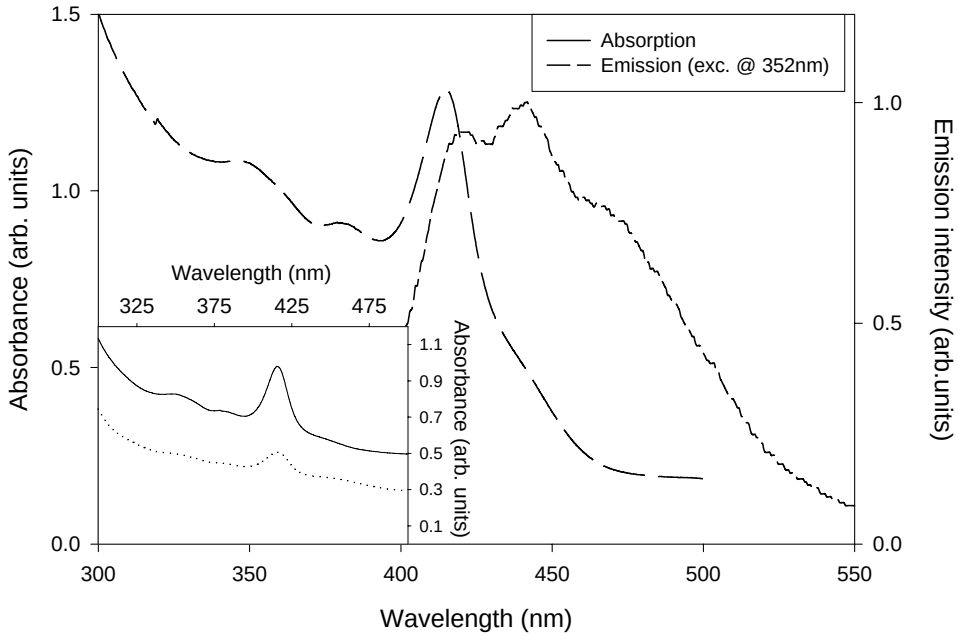

Fig. 2-11 Optical characterization of thin films

Absorption spectrum (long-dashed line) and emission spectrum (short-dashed line) of the bilayer thin film. In the inset, absorption spectra of monolayer thin films prepared using polystyrene mixture (70mg/ml, solid line) and PMMA mixture (50mg/ml, dotted line).

We noticed a slightly improvement of the quartz surface coverage and, consequently, of the optical absorption properties. However, the intensity of the main excitonic peak (i.e. 415nm) is still too low and the baseline of the spectrum is too high, signaling the presence of scattering phenomena. Therefore, even though we improved the overall uniformity of the film, the optical properties of the nanocomposite material are not sufficient for device applications.

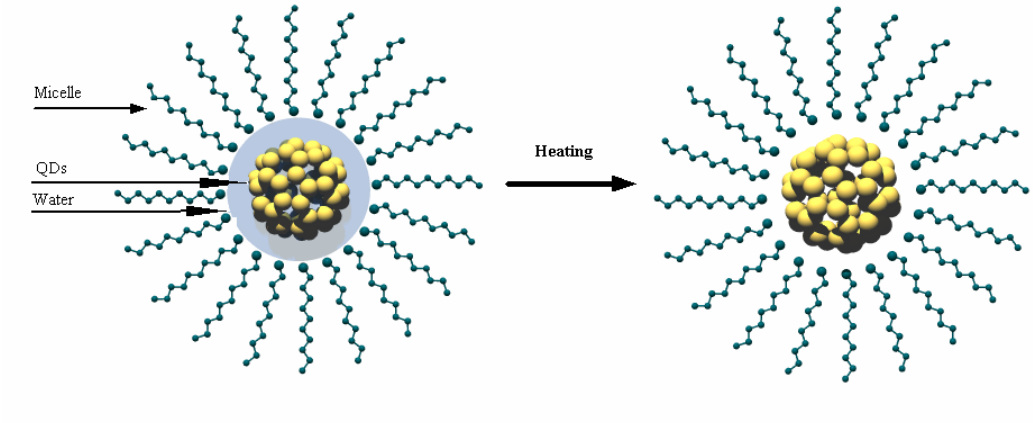

Fig. 2-12 Heating effects

To solve the scattering phenomena, I used increased temperatures to increase the film transparency. Additionally, the large amount of polystyrene would reduce the linear absorption, but low amount of polystyrene could form any structure on the quartz substrate. I use the high polystyrene film as the base, and heat the CdSe solution on top of the base. A strong and transparent film layer forms, and many layers can be added.

The thin film fabrication technique consists of the initial spin-coating of the polystyrene layer (from saturated polystyrene in toluene solution) on a 1mm-thick quartz substrate (at 5000rpm until uniform coverage of quartz plate is achieved)

followed by deposition of the toluene mixture (surfactant-capped QDs in a polystyrene matrix) on the pure polystyrene layer. Post-deposition thermal treatment, at temperatures ranging from 50 to 80°C for 10 to 20min, is required in order to obtain an optically transparent thin film.

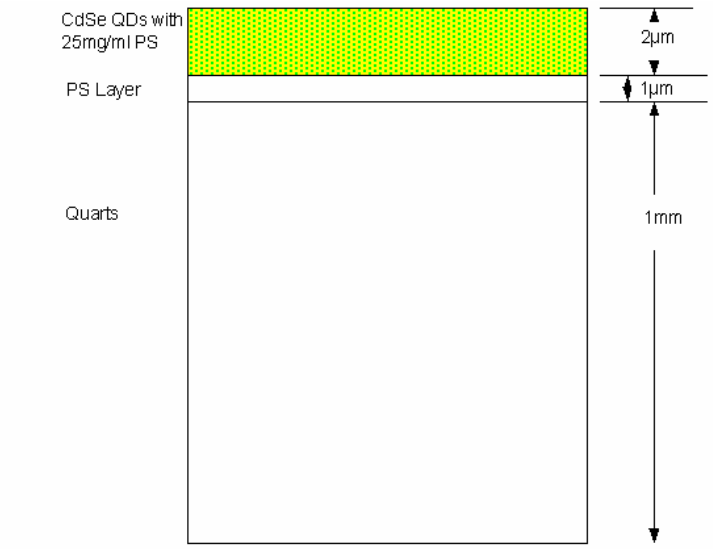

Fig.2-13 Film structure

When we form the thin form, we found an interesting temperature dependent effect. We varied the temperature, and we got a series films with different absorption spectrums. At low temperature, most of the times we get similar film absorption spectrum as the solutions absorption spectrum in Fig.2-14.

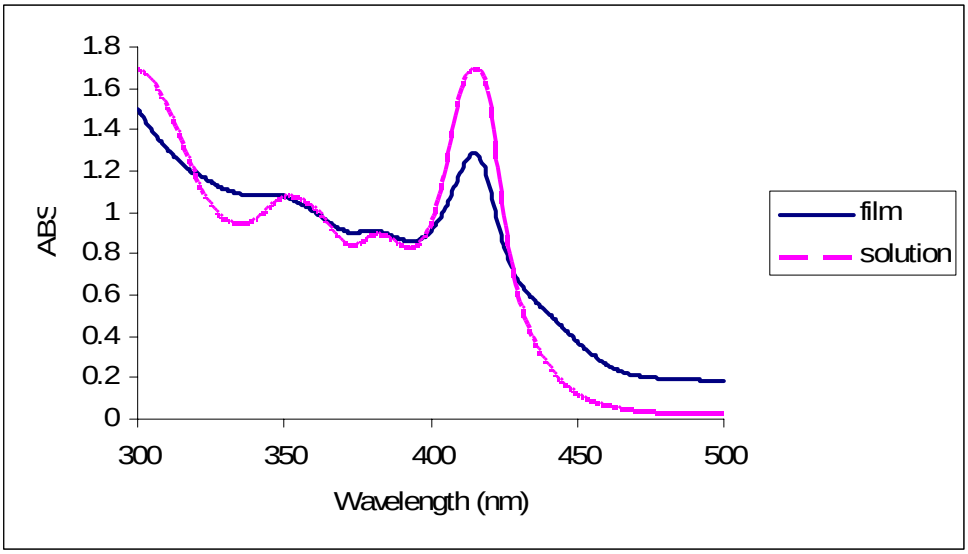

Fig. 2-14 CdSe Film at low thermal heating temperature

As we increase the temperature, the peak absorption at 415nm decreases; however, the peak absorption at 450nm increases. At temperature above 80°C, a strong absorption peak at 450nm develops as shown in Fig.2-15.

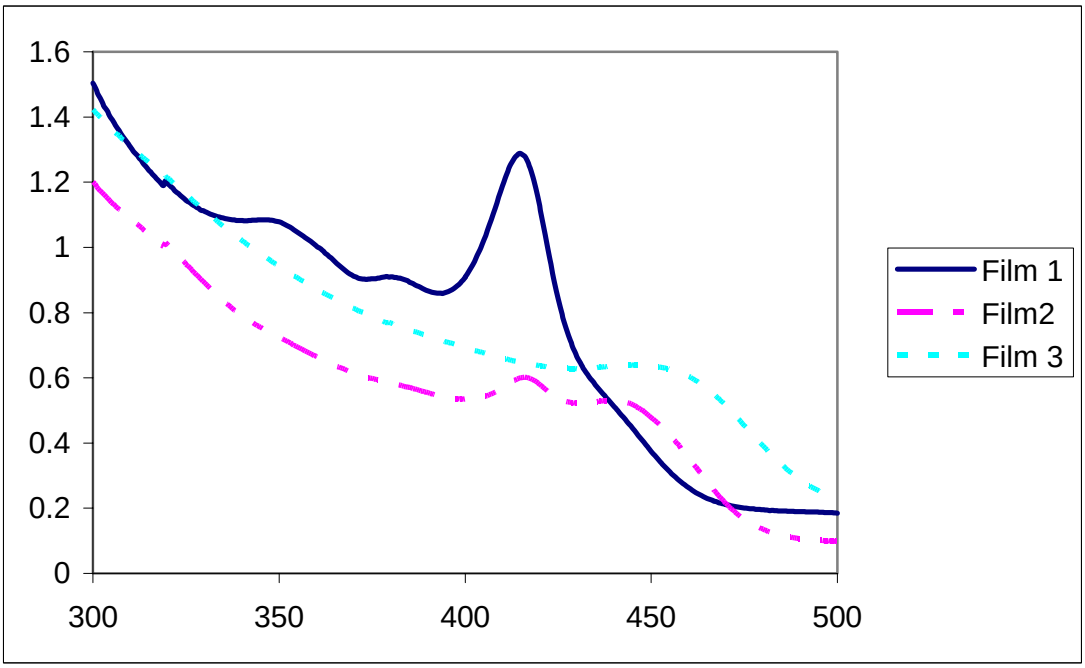

Fig. 2-15 CdSe Film and thermal heating temperature

2.4.6 Photoluminescence Spectrum

We use the 1mm cell containing the CdSe solution, and pump at 355nm.

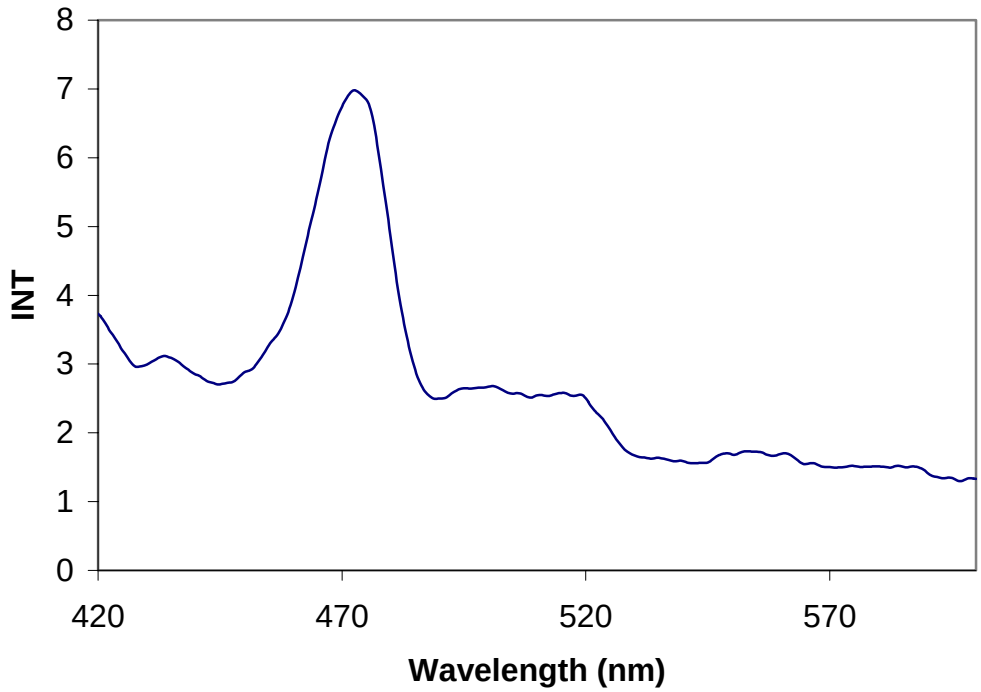

Fig. 2-16 the emission spectra ex 355nm

We also recorded emission spectra of the thin film (Fig. 2-16). With excitation at 355nm in 1mm cell, we observe emission mainly at three different wavelengths (433, 470 and 520nm). This is typical of systems in which the active components are very close one to each other and indicates the possibility of obtaining energy transfer between the nanoparticles.

2.4.7 Stability of CDSe Quantum Dots

The CdSe QD solution in [45] is very stable, but the Cdse QD solution is not stable in our experimental results. We observe that the QD in solution precipitate after a week. After two weeks, the CdSe QD solution has almost no absorption at those

wavelengths. After we mix the polystyrene into the CdSe solution, the solution decays in a few days, which means polystyrene structure in toluene push CdSe capped with micelle out of the toluene solution. We used Transmission Electron Microscopy to analyze the precipitates, and found that CdSe QDs are still in those precipitates.

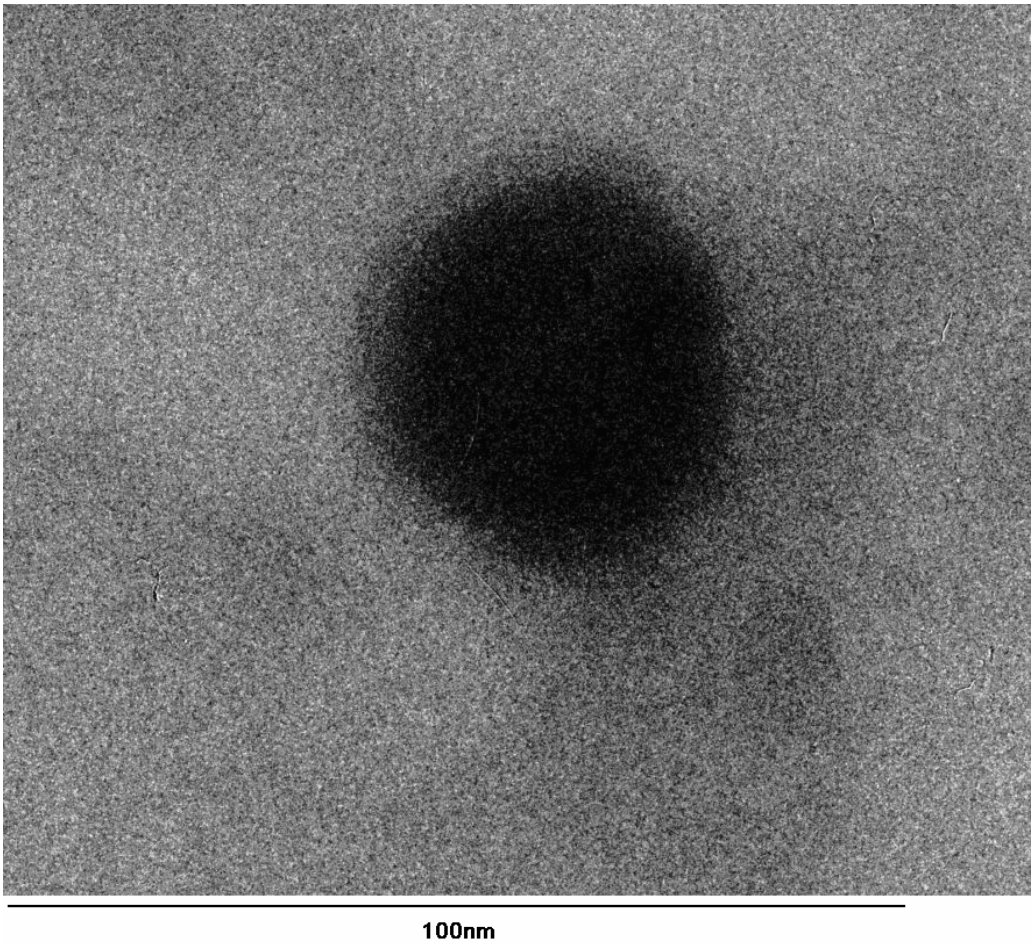

Fig. 2-17 the precipitate image

The stability problem happens in the CdSe film too. In Fig. 2-18, it shows the temporal evolutions of the absorption spectra of CdSe thin films. Optical data were recorded at the same experimental conditions, to make the spectra of comparable magnitude. As a basis for comparison, the absorption spectra of the as-synthesized toluene dispersions are also reported; these data are represented in the respective

graphs as a dashed line. As shown in the Fig.2-18, the CdSe thin film decays in a few days.

An improved method for CdSe film is to place another PS layer on the top of the CdSe layer, which protects the CdSe film from the air. The film with protected layer will last weeks with less change in absorption spectrum.

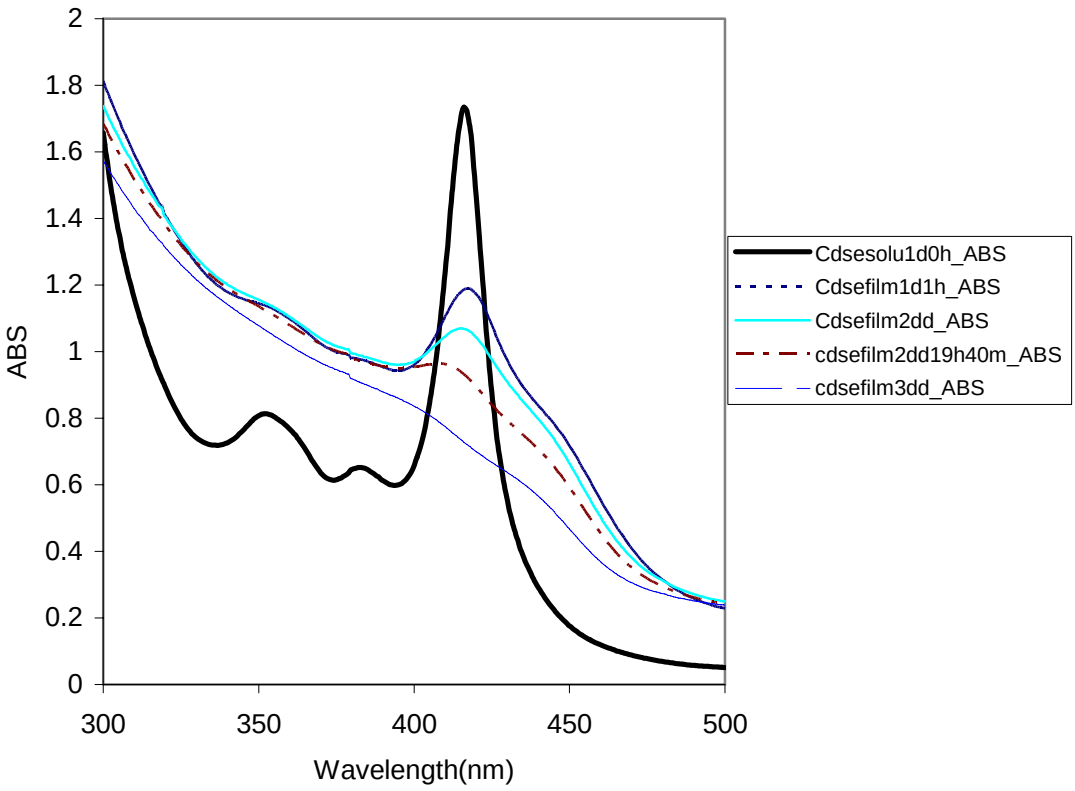

Fig. 2-18 CdSe film aging

2.4.8 The Beer Law and Quantum dots concentration

Using absorption spectral data we can also determine the CdSe molar concentrations (C_{CdSe}). In particular C_{CdSe} can be directly calculated from the the optical density of colloidal CdSe dispersions in the short-wave section of the spectra far enough from

the absorption threshold. Authors of [47] showed, that the optical density of CdSe colloids at 350 nm (D_{350}) can be used for C_{CdSe} determination, since the discretization of the energy spectrum of CdSe nanocrystals due to quantum effects of exciton confinement do not noticeably affect the structure and the intensity of the absorption band. So, the molar absorption coefficient of CdSe nanoparticles at 350 nm, ε_{350}, and therefore, the optical density D_{350} do not depend upon their size. According to [47], C_{CdSe} can be calculated using the following expression:

$$C_{CdSe} = \frac{D_{350}}{1.438 \times 10^{32} \times (2R)^3} \qquad (2\text{-}1)$$

Here we use a variation of this formula, since our samples show absorption peaks around 350nm. Specifically, D_{350} in the previous expression must be substituted with D_{300} in order to have a reasonable estimation of C_{CdSe}. In fact, the density of states is approximately constant at 300nm and the absorbance is indicative of the number of unit absorbers rather than the oscillator strength of a particular electronic transition.

2.5 CdS capped with reverse micelles

CdS QD capped with sodium bis(2-ethylhexyl)-sulfosuccinate(AOL) reverse micelles are widely studied by many groups[48]. However, we are the first group to report CdS QD capped with decylamine, a simple and short length surfactant. The new CdS QD has very significant linear and nonlinear optical properties.

Recently, He et al. [49] reported a large third-order nonlinearity of CdS NCs embedded in Nafion films. Capped CdS NCs in polydiacetylene and polystyrene [50]

were also reported for enhanced nonlinearity compared with bulk materials. However, there is no reported novel two-photon absorption in those materials. Here we observe that TPA is more than 2 orders of magnitude greater than those in CdS bulk materials [50], and more than 4 orders greater than those reported TPA in semiconductor-NC-doped glasses [51].

2.5.1 Synthesis of CdS QD

After investigating the CdSe QD in toluene, I create my own recipe of synthesis CdS QD capped with reverse micelle. CdSe QD grows at a very slow rate, but CdS QD grows into aggregates in less than seconds. The main changes made in the published preparation for CdSe NCs are indeed mandatory due to the faster reaction time (microseconds instead of 20 minutes) of CdS nanoparticles formation. I found that there are too effective procedures to slow down the reaction time, and increase the yield of CdS QD in toluene. One way is to increase the amount of surfactant (Decylamine), and increase the number of the micelles in water. Another easy way is to add the Hydrochloric Acid (HCL) into the mixed synthesized solution. HCL is also the first time used in CdS QD preparations. Using HCL, it is very easy to control the synthesis procedure. First we dilute HCL to 5%, and make it easy to tune the strongest absorption wavelength. Specifically, 5ml of an aqueous solution of cadmium nitrilotriacetate (CdNTA), obtained by dissolving 0.79g of $CdSO_4$ and 1.1g of sodium nitrilotriacetic acid in 50 ml of water, was mixed with 1.0 ml of decylamine ($CH_3(CH_2)_9NH_2$) as surfactant. The cadmium ions bind to the amine groups of the

surfactant. The solution is further added to a mixture consisting of 5ml aqueous solution of sodium sulfide (Na_2S, 0.05M) and toluene (8ml). The products come together to form micelle-capped nanoparticles in the toluene side.

However, we have found that the absorption properties of CdS nanoparticles are also sensitive to procedures used with the reverse-micelle method. For example, when we change the last step in the procedure by adding sodium sulfide aqueous solution (after that, we add toluene into the mixed solution.), rather than the mixture consisting of sodium sulfide aqueous solution and toluene we observe a large amount of yellow solid material (CdS) growing in the solution.

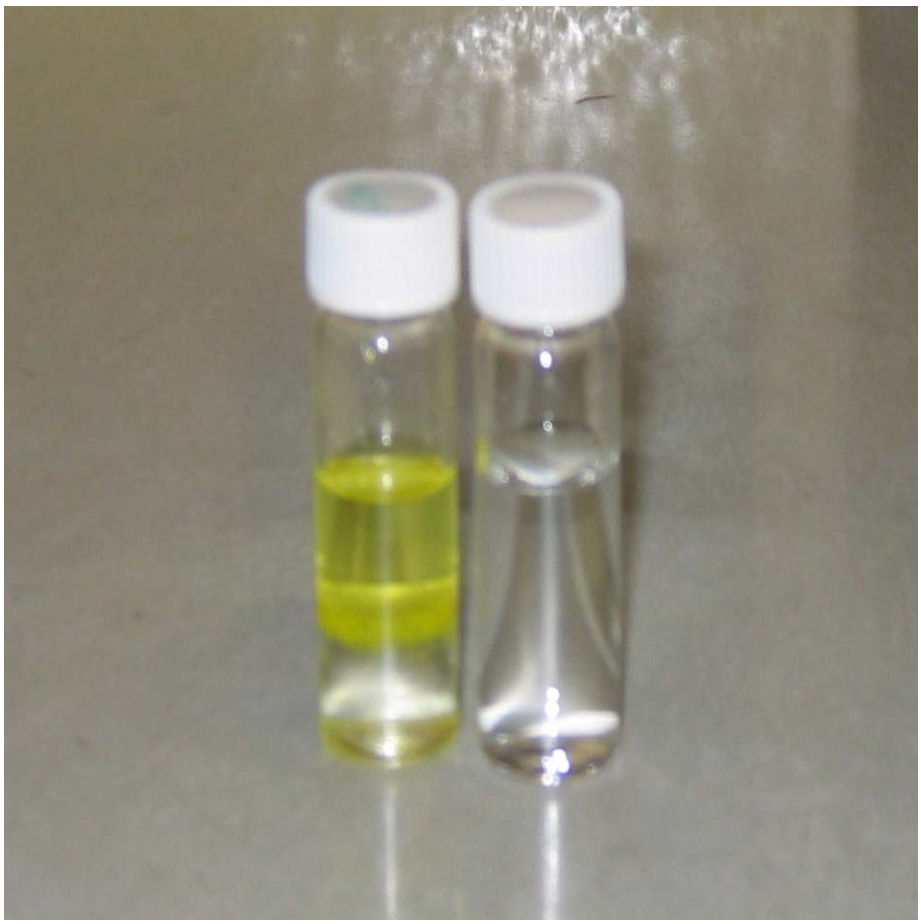

Fig. 2-19 CdS solutions

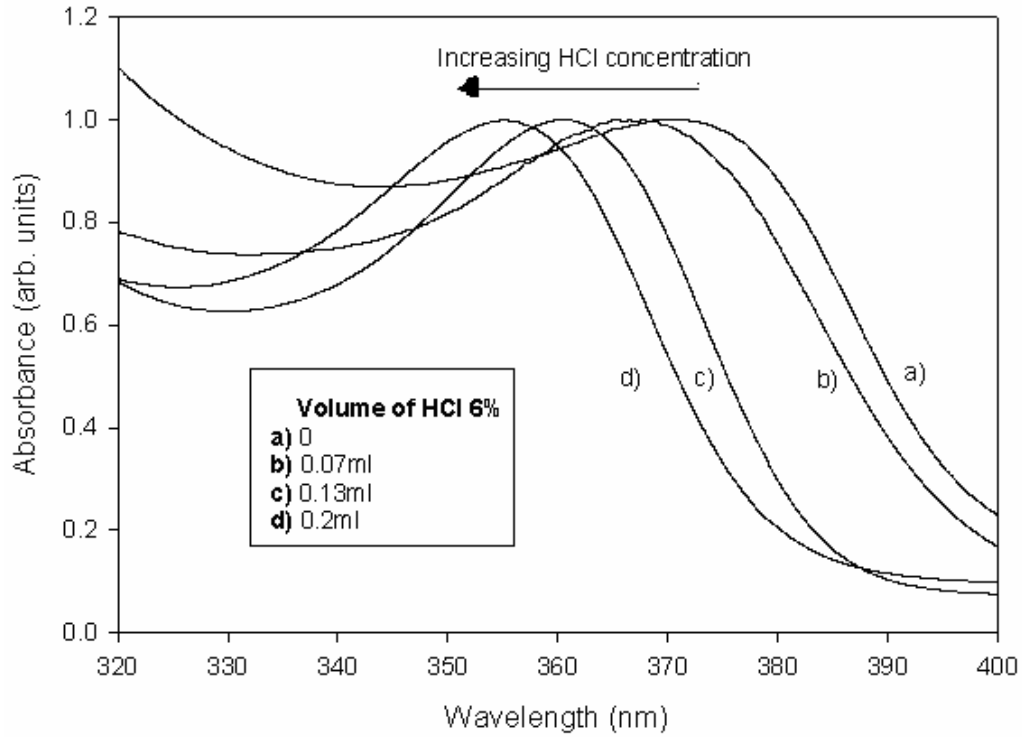

Fig.2-20 A series absorption spectrum of CdS QD solutions

2.5.2 CdS QD Size Calculations

In this section, we discuss about QD radius. As the QD radius increases, the bandgap increases. One way to investigate this effect is to calculate the excitonic bandgap. There have been several theories for calculating this phenomenon [52]. In particular, one simple formula, in the tight-binding framework, is given by the expression [52] for CdS QDs where $E_g(R)$ is the size-dependent excitonic bandgap, defined as the energy of the lowest exciton state with respect

$$Eg(R) = 2.5 + \frac{1.52}{R^{1.632}} - \frac{0.435}{R^{1.032}} \qquad (2\text{-}2)$$

We calculate the bandgaps and QD sizes for the wavelength at 340nm, 360nm, 380, 400nm, and 420nm in Table2-1.

Table 2-1 Dots diameter and band gap

Wavelength(nm)	Δ Band gap(eV)	Dot Diameter(nm)	Color
340	1.099	2.0	no color
360	0.8963	2.22	no color
380	0.7149	2.51	no color
400	0.5516	2.87	no color
420	0.4039	3.38	greenish

to the ground state and is given in eV, and R is the QD radius in nm. The radius of the QDs used in the experiments reported here is 1.1 nm. The bandgap of bulk CdS is 2.55eV.

2.5.3 CdS Linear Enhancement

To form the optical thin film, we mixed polystyrene inside the CdS QD solution. Thought the absorption spectra study, we interested found increased linear absorption by add polystyrene into the CdS solution (peak absorption around 370nm).

To further investigate this phenomenon, we recorded the UV-VIS absorption spectra of the CdS toluene dispersion before and after mixing the nanoparticles in reverse micelles with the PS matrix. In Fig.2-21, the absorption increase as the polystyrene dissolve in CdS solution. After three hours, the absorption peak is stable. As one can see from the peak absorption intensity of the PS-CdS/micelle mixture is

more than two times bigger than that of the as-synthesized dispersion.

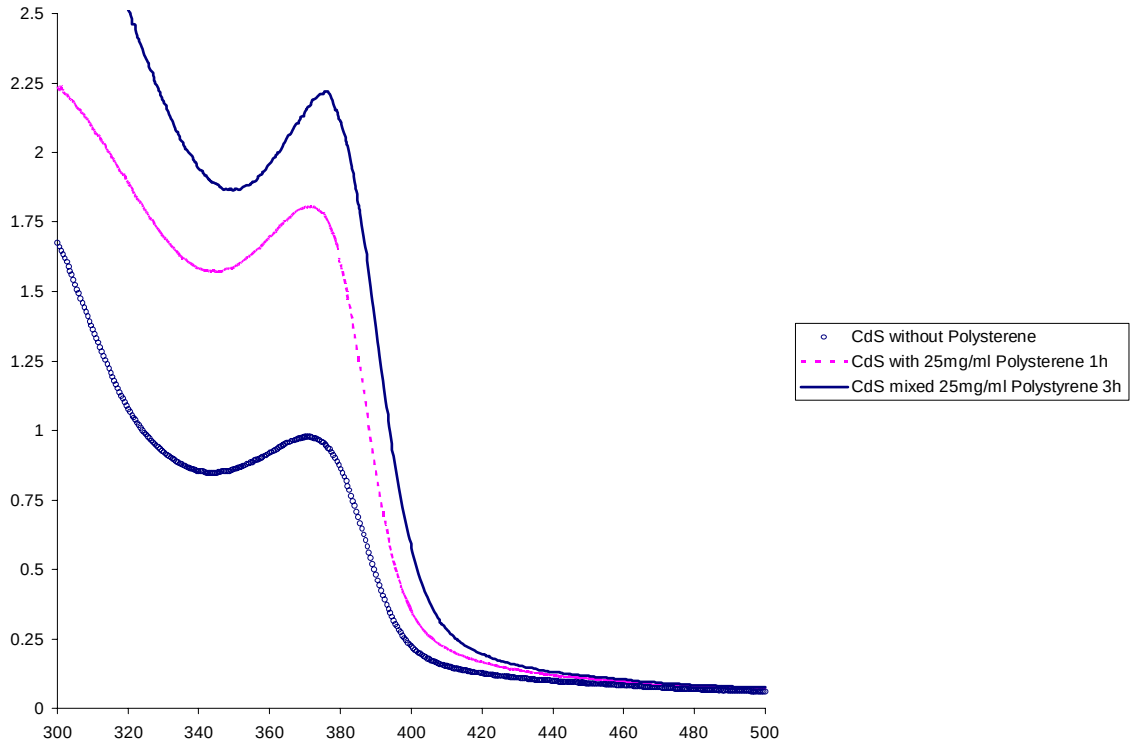

Fig.2-21 Linear absorption enhancement

We also measured the emission spectra, recorded at an excitation wavelength of 374nm, before and after the addition of PS in Fig.2-21. The photoluminescence increase in the PS mixture (i.e. the emission intensity grows by more than four times) in Fig.2-22.

At this time we believe that this effect is due to the reduction of trap states for nonradiative recombination provided by the PS matrix. Hence, the polymer used in the system under investigation acts as a stabilizer of micelle-capped CdS NCs, interrupting their agglomeration after the stage of nanoparticle formation and protecting them from oxidation.

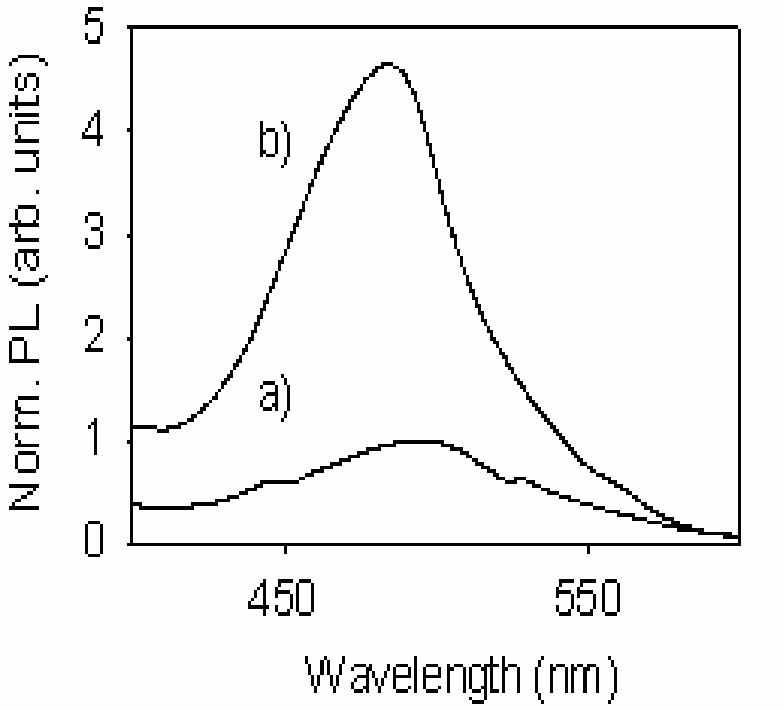

Fig. 2-22 Photoluminescence enhancement

These effects cannot be seen in the CdSe thin film sample for reasons that are not presently understood. However, as we increase the amount of polystyrene, the absorption deceases. The same happens in the CdSe solution too.

2.5.4 TEM of CdS capped with reverse micelles

In this section, we present various TEM images. First, we will show the images of CdS QD capped with reverse micelles. We will observe large amount of CdS QD, less nanorods, and some big aggregates on carbon copper grids. Large number CdS QDs are found on the grids. Most of the CdS nanoparticles are dots, but a small part is large rods in Fig.2-23 (a), (b) and (c).

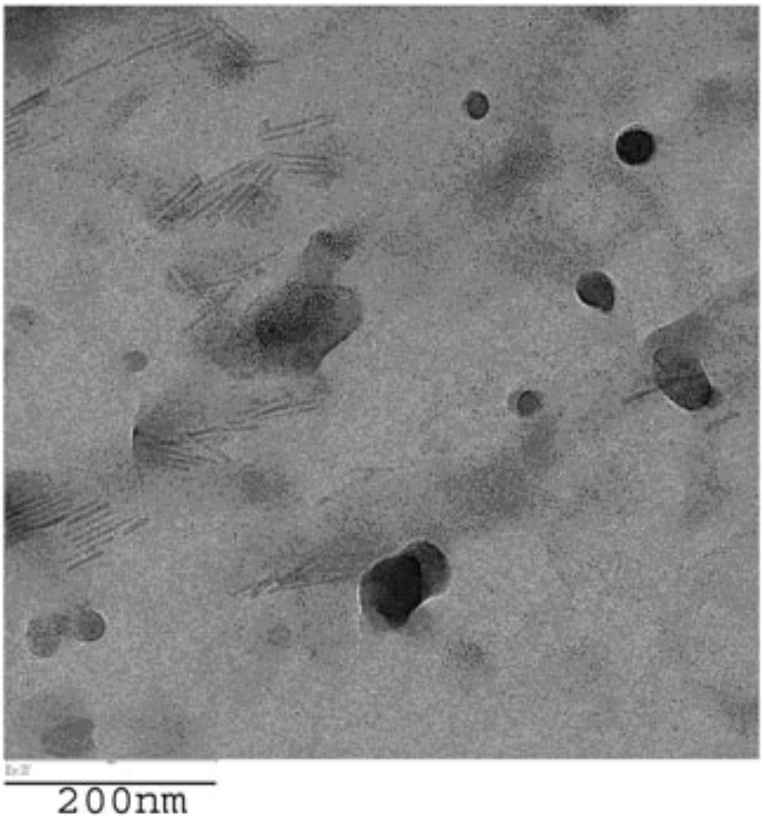

(a)

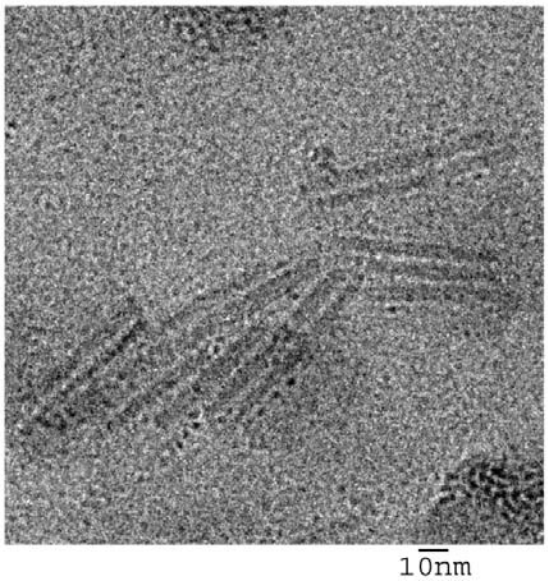

(b)

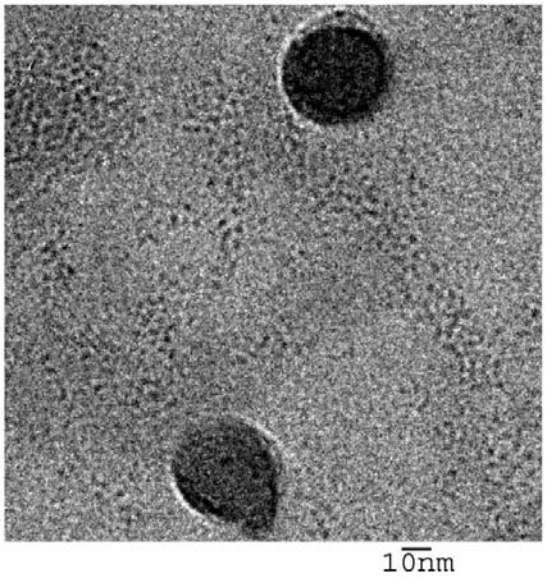

(c)

Fig. 2-23 CdS without Polystyrene (a), (b) and (c)

After we mix the polystyrene inside the CdS solution, we observe a new structure formed on the carbon copper grids through the TEM study. We study two groups of CdS solutions with different amount of polystyrene. The first group is mixed with 10mg/ml polystyrene, and the other group is mixed with 25mg/ml. We found that there is less structure in the 10mg/ml group, and more similar structure in the following images. Because the polymers interact with electrons, we could not see more detail of the connection between the quantum dots.

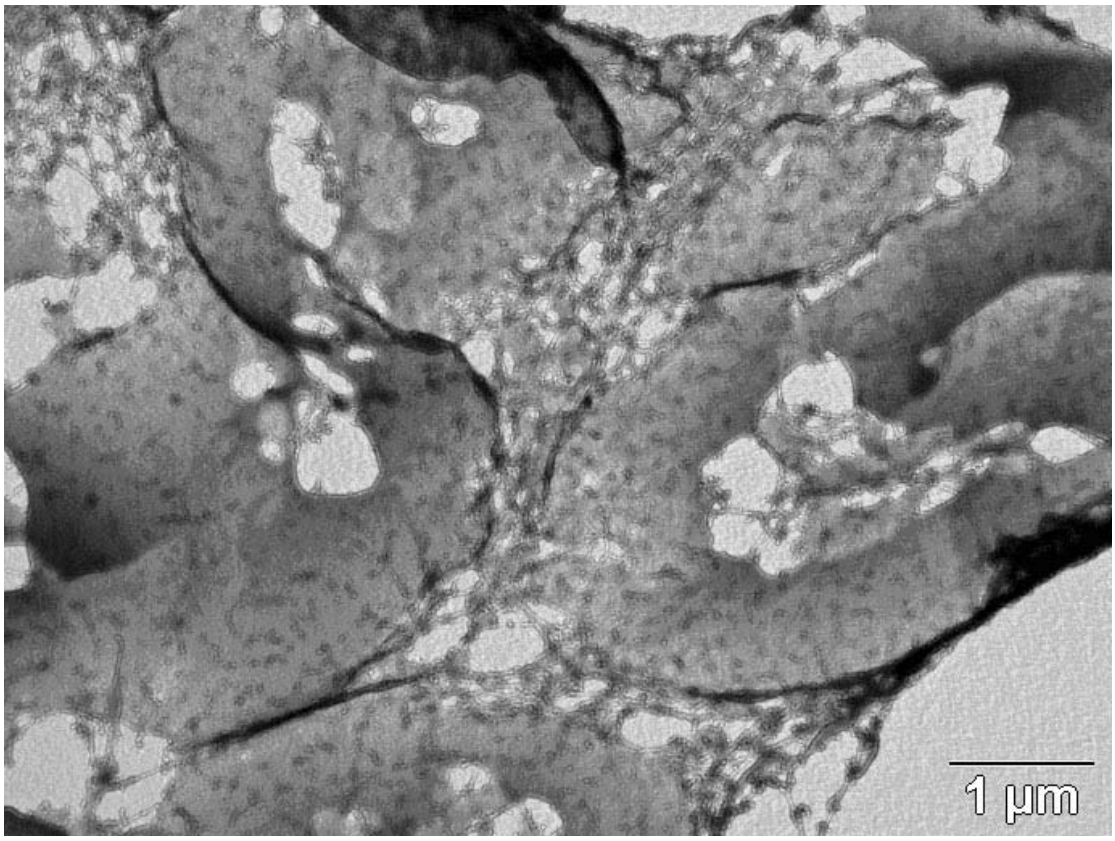

(a)

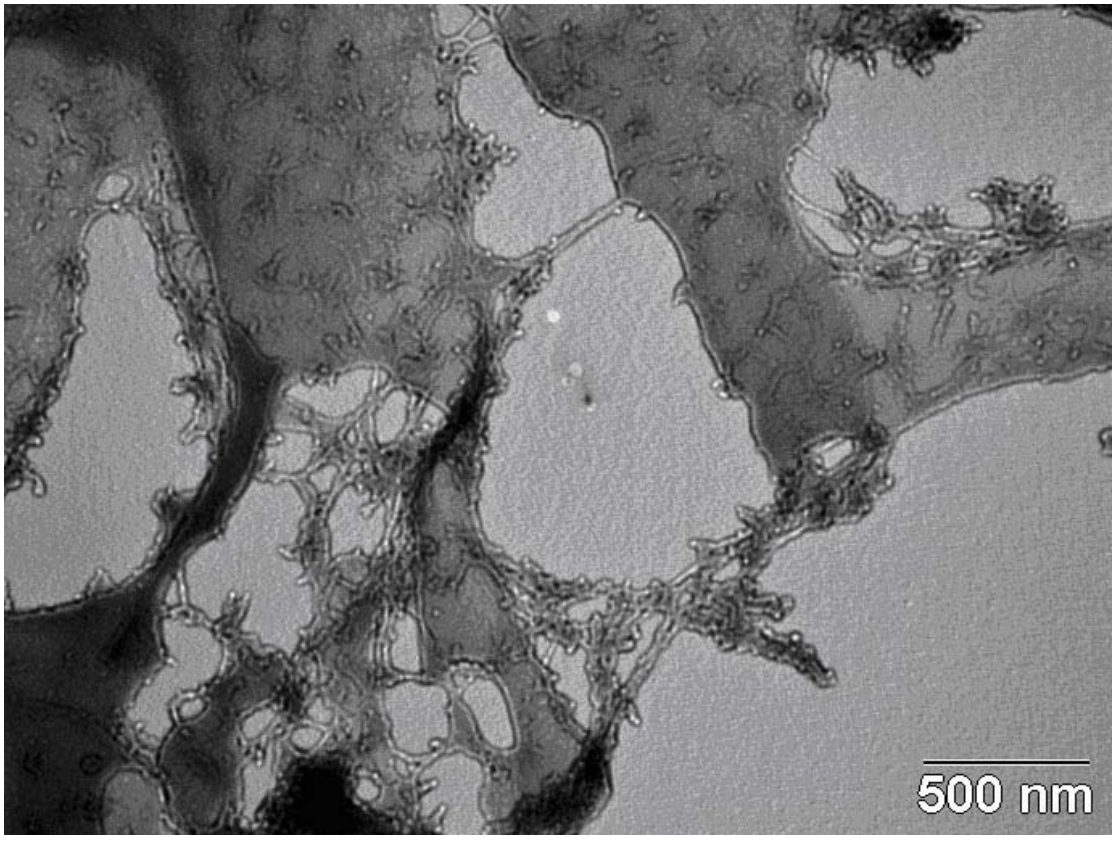

(b)

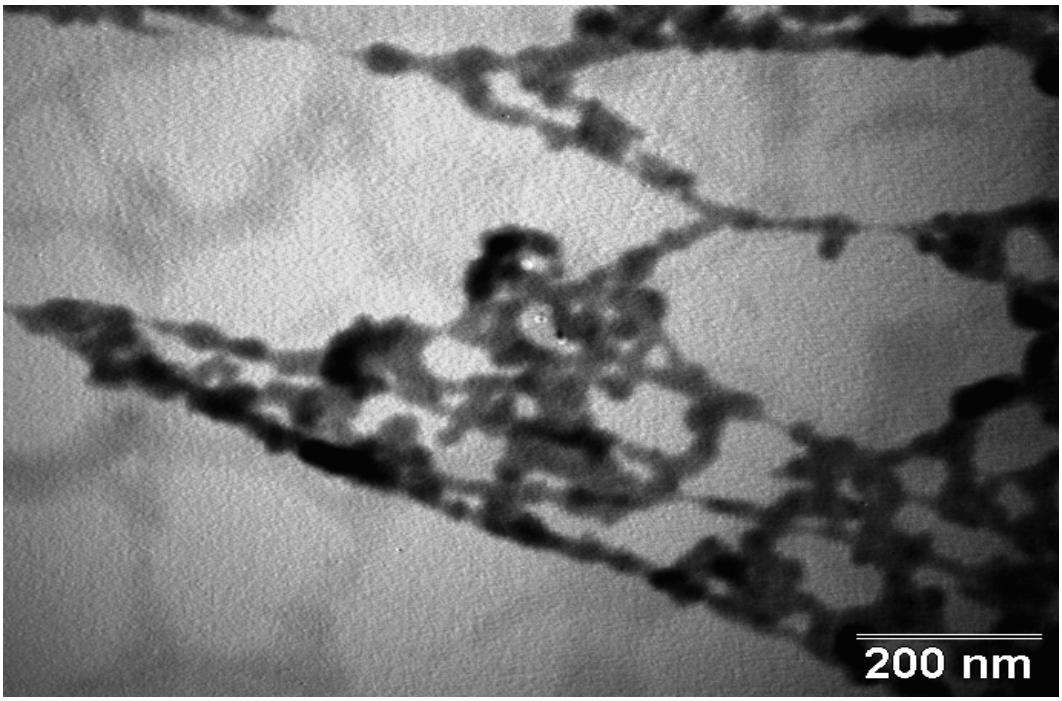

(c)

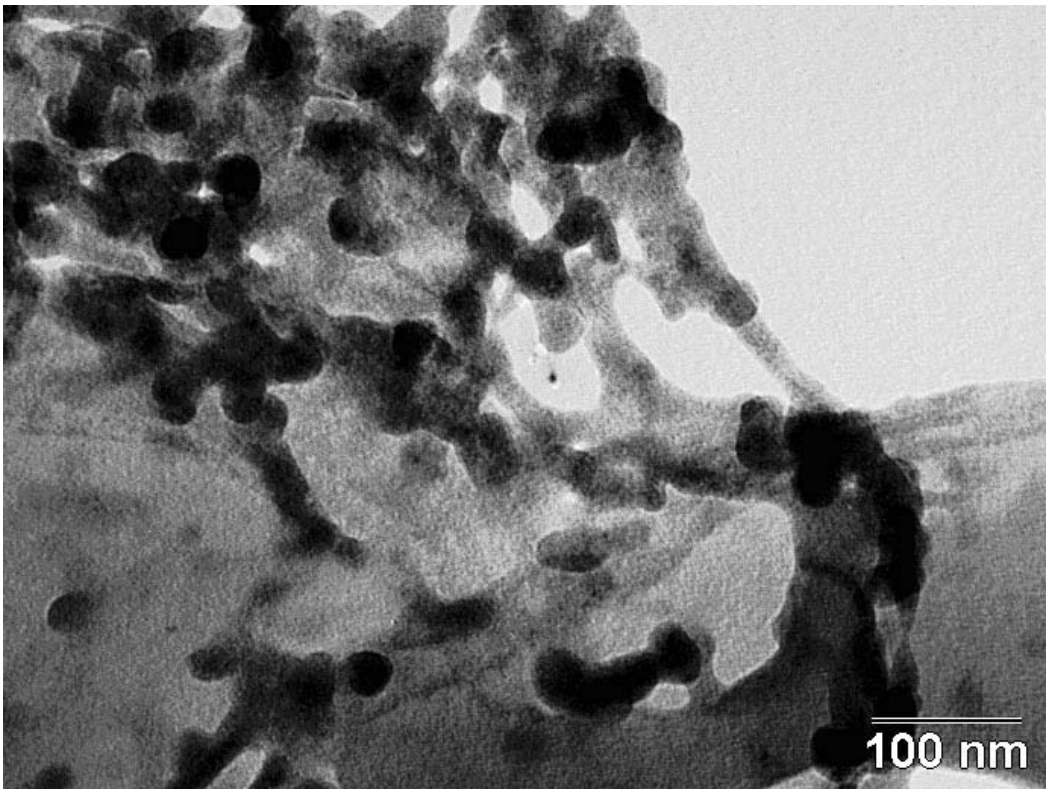

(d)

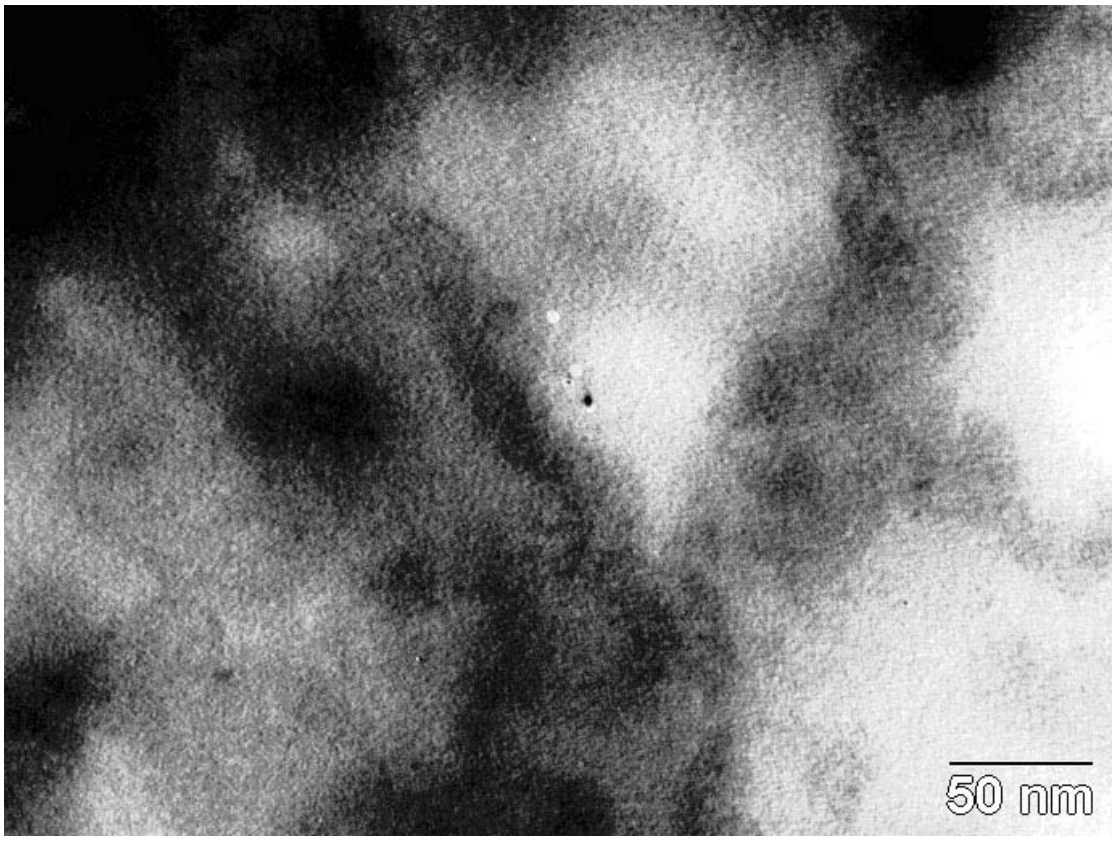

(e)

Fig. 2-24 CdS with Polystyrene (a), (b), (c), (d) and (e)

2.5.5 CdS Film

When we form the thin film, it is initially opaque. To solve this problem, we proceed as in the case of the CdSe film; however, in this case the film forms more easily. As we discuss in the TEM section, CdS solution with low concentration of polystyrene has very good structure. It forms very good thin film with heating.

The toluene dispersion, after being optically characterized, is mixed with 25mg/ml polystyrene (PS). In order to obtain the best optically transparent thin film, we use thermal treatment at temperatures ranging from 70°C to 100°C. As we can see in the Fig.2- 25, Film 1-3 have different absorption peaks.

Variations of the temperature can also move the absorption peak, which means that the absorption peak can further shift from the original CdS QDs solution. But this shift may be small i.e. a few nanometers, or large ~ 40nm as shown in the Fig. 25. While the CdS QDs under the high temperature around 80°C, the QDs gain energy and the QDs increase in size. The evaporation speed and the duration of the high temperature in the procedure are the two main reasons for the shift of the absorption to the right. Using the same solution which has absorption at 356nm, we form four different thin films. These three films have the absorption peaks at 358, 364 and 400nm in Fig.2-25.

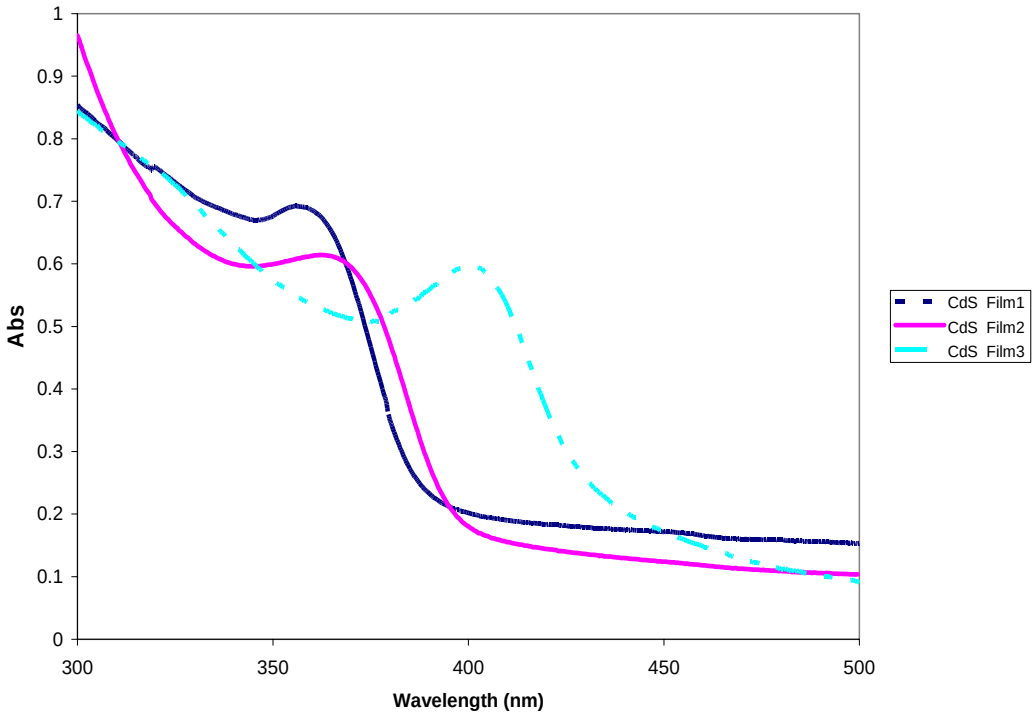

Fig.2-25 Films with Varied absorption peaks

We also measured the emission spectra of Film 2, recorded at an excitation wavelength of 320, 350 and 380nm in Fig. 2-26.

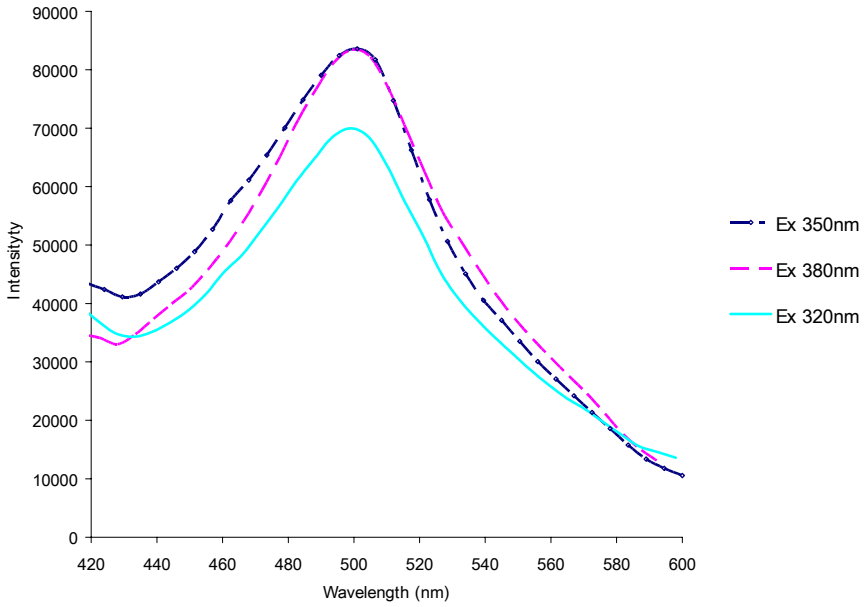

Fig.2-26 The three photoluminescence

2.5.6 Stability of CDSe Quantum Dots

The CdS QD structure is much stable than the CdSe solution, and it lasts months with very little change. After we mix the correct amount of polystyrene into the CdS solution, the solution is still very stable, unlike the CdSe solution which decays in a few days. There are no precipitates found here unlike in the CdSe solution. After we study the TEM of CdS solution with polystyrene in the last section, we think that the CdS capped with reverse micelles well attached onto the polystyrene chains. The CdS thin film also shows a greater stability than the CdSe thin film.

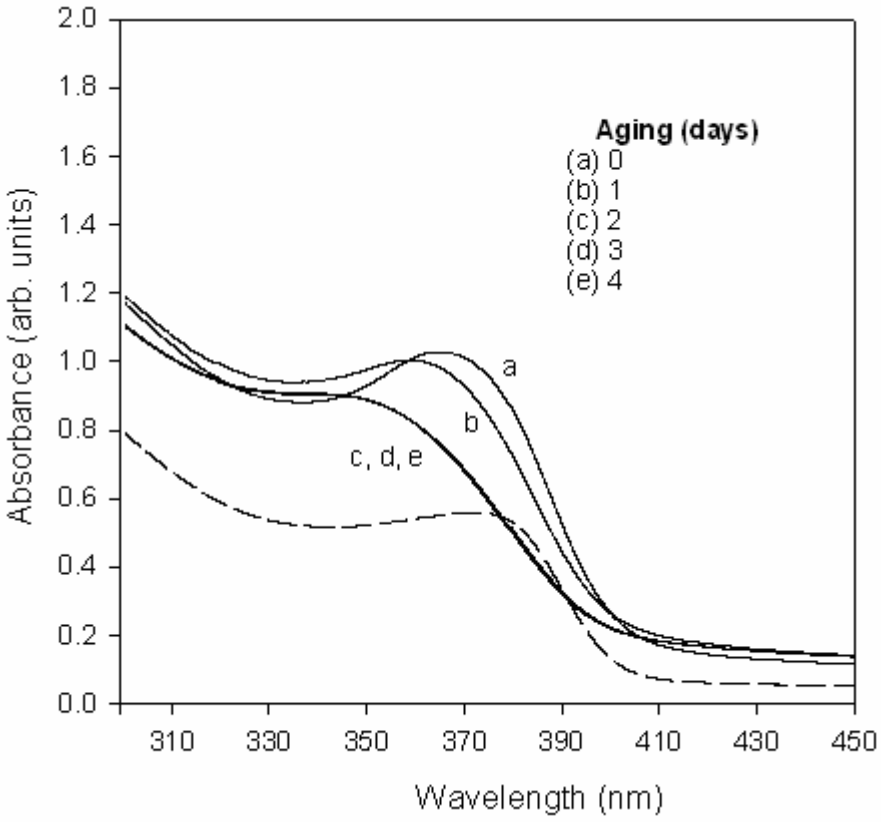

Fig. 2-27 The CdS Aging curves

The temporal evolution of the absorption spectra of the CdS thin film (see Fig. 2-27) shows that absorption reduces from curves a) to b), becomes apparently stable (curves c), d) and e)). The CdS thin film becomes very stable after three days. After months, the emission and absorption have a little after that. It should also be noted that the absorption intensity of the CdS thin film sample is significant higher than the liquid phase (toluene dispersion). In fact in the toluene dispersion, it is presumed that the distance between the nanoparticles is much larger than their size (tens of nm compared to a few nm), so the effect of interparticle interactions is small. In addition, the increment of the absorption band intensity is accompanied with the increase quantum dots concentration.

2.6 CdS in dendrimers

The architecture of the polymer matrix can be used to help in controlling the particle size and size distribution. The blocking copolymers isolate the semiconductore clusters as they form. In the development of nonlinear optical materials, one of the major steps is the synthesis of semiconductor QDs in nanostructured composite materials. These materials involve the combination of QDs with a processable matrix [54]. Some matrix materials used include polymers, copolymers, polymer blends, glasses, and dendrimers. Dendrimer/semiconductors nanocomposites may also be good candidates as materials for optical circuits incorporating switching functions that require a combination of high value for the nonlinear coefficient and very low values of the one-photon and two-photon absorption coefficients. However, there is no reported figure of merit assessment of dendrimer/semiconductor nanocomposites for these applications.

2.6.1 PAMAM dendrimers

PAMAM dendrimers represent an exciting new class of macromolecular architecture called “dense star” polymers, which are produced by dendritech. “Dendrimers” was derived from its tree-like branching structure.

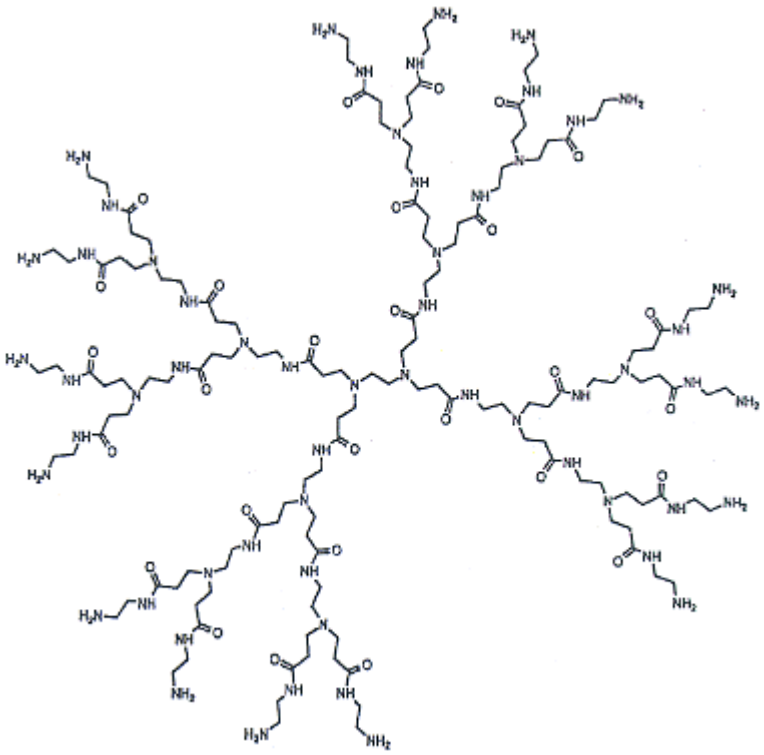

Fig.2-28 Generation 2 PAMAM Dendrimer

Dendrimers are not like classical polymers, whose don't have unique molecular weight. Dendrimers have a high degree of molecular uniformity, narrow molecular weight distribution, specific size and shape characteristics, and a highly-functionalized terminal surface. They are very good nano-blocking media because their large tree-like structure. Between the branches and leaves, there is perfect space left for those nanoparticles. These branches prevent the nanoparticles growing into big aggregates. They can be assumed to act as discrete encapsulating entities. Dendrimers are attractive as building blocks in nanodevices because the locations of the core, branches, and surface functionalities can be controlled and tuned with high accuracy.

Beyond their role as nanoreactors, dendrimers confer thermal and chemical

stability on the encapsulated semiconductor nanoparticles. Most importantly, dendrimers having generation-dependent, multiple functionalities at their surfaces are ideally suited to develop interfaces to other materials based on the multivalency concept [55-56].

2.6.2 CdS in dendrimers

We have investigate poly(propyleneimine) dendrimer matrix having a diaminobutane (DAB) core with and without 2.2 nm CdS nanocrystals[56]. We investigate three different generation, CdS-G4, G5 and G6. Dendrimers are named by each subsequent growth step, which represents a new "generation" of polymer with a larger molecular diameter. The new generation is twice the number of reactive surface sites, and approximately double the molecular weight of the preceding generation[57].

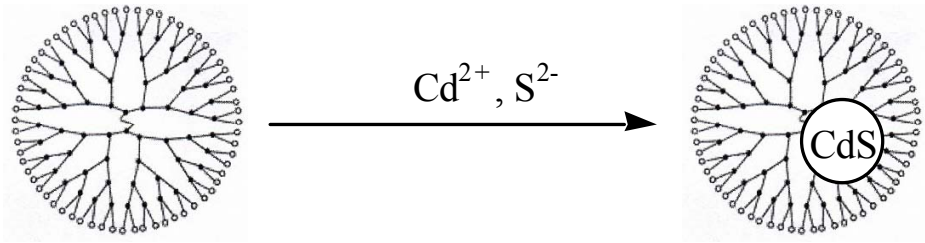

Fig. 2-29. Synthesis of hybrid, dendrimer-encapsulated CdS quantum dots.

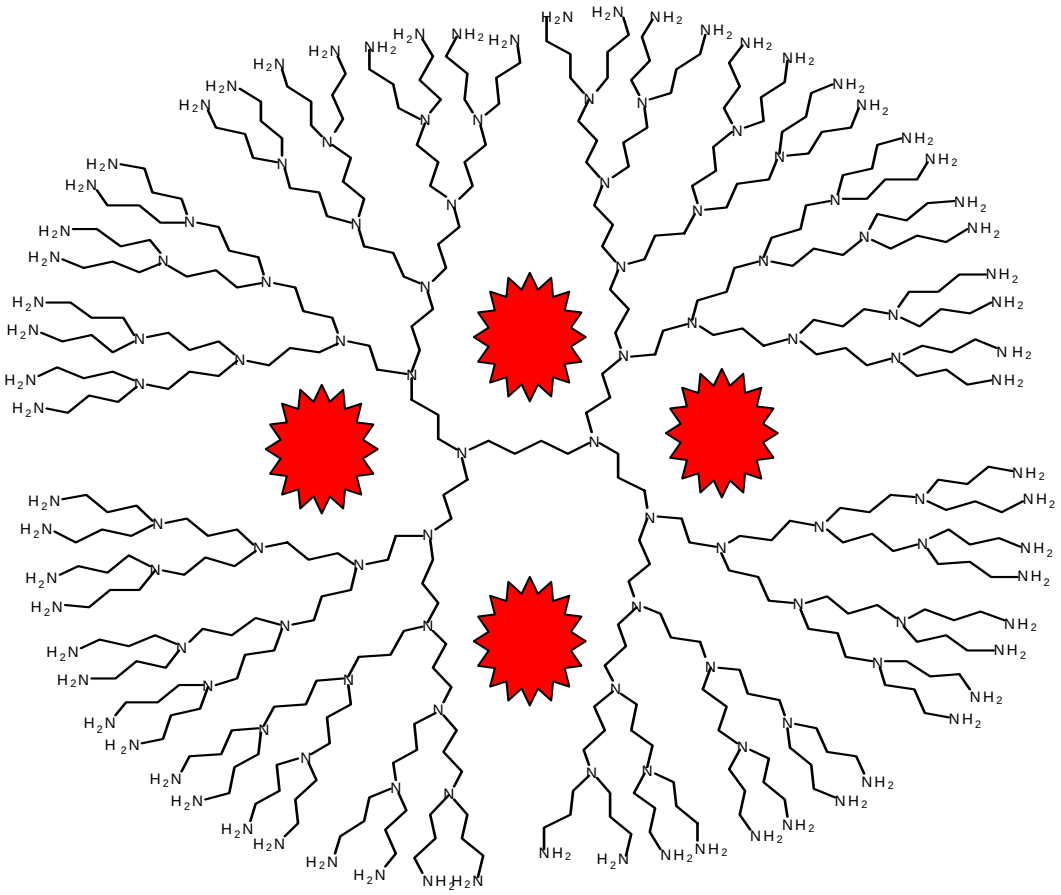

Fig. 2-30 Schematic of Poly(propyleneimine) dendrimer with 1,4-diaminobutane (DAB) Core DAB-Am-64 (Generation 5.0)

2.6.3 The absorption and emission spectrum of CdS in dendrimers

In Fig. 2-31, the CdS G5-DAB film absorption spectrum shows a flat curve over 370nm to 300nm, which means a large range dots distributing in all the branches of the dendrimers. Between 200nm and 300nm, there may also have many even smaller dots inside.

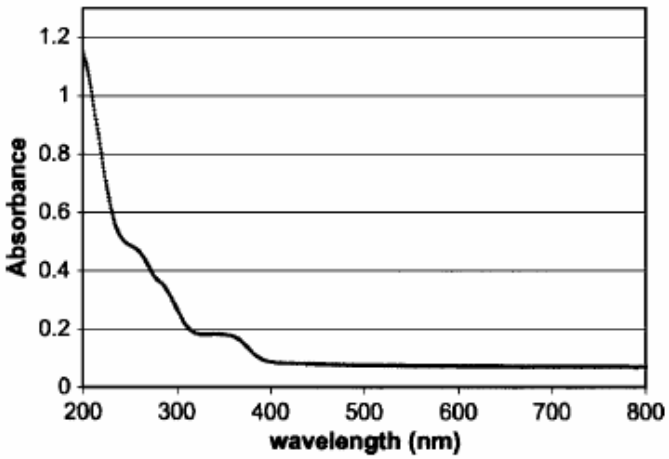

Fig.2-31 The nanoparticles size control of CdS in dendrimers

A lower emission is observed in a broadband from 380 -650 nm with peak at 480nm in Fig. 2-32. As we discussed above, CdS capped with micelles has the emission at 500nm with a narrowed band.

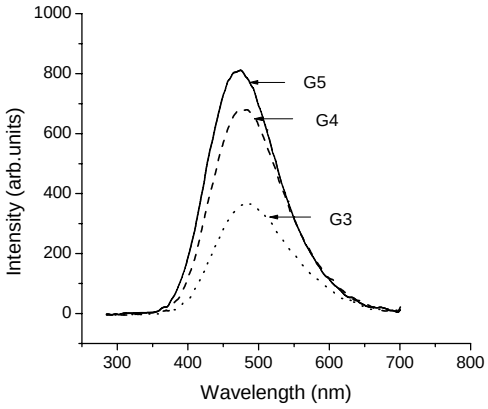

Fig. 2-32 CdS in G5-DAB emission

2.7 Conclusion

Using a simple, yet robust, reverse micelle synthesis method, we successfully prepared a new nanocomposite material. Fine adjustments of the preparation conditions allow one to tune the absorption properties of the sample, so that one type of material may be used for different optical devices through the use of simple

changes at the fabrication stage.

However, one of the primary objective of this effort was the development of a solid state material incorporating micelle-capped CdSe and CdS NCs whose photophysical properties correspond to that of the QDs in a fluid environment (specifically, in a toluene dispersion). The final products are homogeneous thin films having long lifetime and stability. In particular the CdS-polystyrene composite is stable for over 2 months.

The fabrication of optically clear thin films is indeed mandatory for advanced characterization techniques (i.e. Z-Scan and Pump&Probe methods) required to investigate the nonlinear optical properties of these nanomaterials. Additionally,, the position of the excitonic absorption bands, and the anticipated strong quantum confinement of the nanoparticles, make these systems promising classes of organic/semiconductor nanocomposites exhibiting large two-photon absorption (TPA) in the visible and near infrared with potential applications in high-speed communication networks such as all-optical switching, modulating and data processing.

Chapter 3 Nonlinear Characterization

3.1 Introduction

The continuing development of lasers with increased intensity is a key enabling tool for the investigation of nonlinear optical properties of materials. The study of the nonlinear refraction and nonlinear absorption of semiconductors, dyes, fullerene, crystals, metals and nanomaterials (in both solution and thin film structures) by research groups [1-3] worldwide shows growing interest in nonlinear optical effects. Some of the many potential applications include optoelectronics, optical data storage[4-5], microfabrication [6-10], photoconductors and photovoltaics [11], markers for genomes and proteins[12-13], biological and medical detectors [14-15], optical limiters [16-18], biomimetric electromagnetic devices [19], nanopatterning of inorganic/organic materials [20-21]. In all these fields, investigations of semiconductor quantum dots (QD) have received significant attention. The quantum confinement of charge carriers leads to novel physical and chemical behavior. Initially the chemical synthesis of QDs was the subjects of intensive research with the goal of identifying and controlling all the parameters that determined their optical properties [22], [23]. Material size and distribution are significant parameters for enhancing the observed optical nonlinearity. Several methods have been used to control these properties including polymer matrix architecture [25]-[27], porous matrix materials [28], and particle-capping methods [29-30].

One of the next major steps in the development of nonlinear optical devices is the

synthesis of semiconductor QDs in nanostructured composite materials, which was discussed in Chapter 2. These materials involve the combination of CdS and CdSe QDs capped reverse micelles in a polystyrene matrix. Other materials have been combined with QDs including polymers, copolymers, polymer blends, glasses, and ceramics.

Several theories have been developed to investigate the properties of the semiconductor QDs [22]. The ability of combining organic and inorganic materials into one nanocomposite may give rise to new kinds of excitons involved in various optical processes [31]-[33]. Recent studies showed significant promise for nanostructures combining ordered QDs and organic materials. The most interesting topic is the design of hybrid materials showing third-order nonlinearities with strong two-photon absorption. The interesting nonlinear effects arise because of the quantum confinement of semiconductors in low dimensions. This effect adds to the possibility of observing new hybrid nanomaterials due to novel hybrid excitons (Wannier exciton of typical semiconductor coupled with Frenkel exciton of typical organic materials).

From our measurements, we obtained a β value of 788cm/GW (the two-photon absorption coefficient, β, was reported to be 3.1cm/GW for bulk CdS at 610nm[34]). This TPA coefficient is almost two orders of magnitude greater than that in the CdS-Nafion film measured by He et al. [18] who reported a β value of 9.5 cm/GW, which –at the time-was reported to be the biggest value for this class of nanocomposites.

Reasons for high nonlinear absorption coefficient are considered to be quantum

confinement effects. First, the complete extraction of water in micelles by heat treatment produce strong modified surfaces at which the decylamine molecules are incorporated with the cadmium ions. This enhances the dielectric confinement effect, i.e. increases the excited state life of capped CdS nanoparticles, and leads further to the increment of two-photon absorption.

In addition, we notice that the absorption spectrum of the self-standing surfactant micelles (i.e. without the capped inorganic nanocrystals) show an electronic transition resonant with the semiconductor excitonic peak energy. The intensity of this absorption is rather small if compared with the strong absorption of the composite material, however we cannot exclude the possibility of interactions between organic/ inorganic excitons. However, in order to fully determine the detailed physics of the system and, therefore, show the actual confirmation of theoretical predictions requires further investigation..

3.2 Close, Open Aperture Z-scan and Transmission Measurement

3.2.1 Z-scan Theory

The Z-scan technique is used to investigate non-linear properties of various media. This method has been developed by Shane O'Brien and Anton Walsh [35].

Normally, two nonlinear coefficients are used to describe the refractive index change of a medium showing the cubic nonlinearity

$\chi^{(3)}$ (ω; ω, ω, ω). These coefficients are related to the refractive index variation via

field amplitude E and the intensity I. E and I are also interconnected by the relation related by $|\mathrm{E}|^2 = \frac{8\pi}{\mathrm{cn}_2}\mathrm{I}$, where

$$n_2 = \frac{cn_0\gamma}{40\pi} \tag{3-1}$$

We assume the Gaussian beam is propagating along the +z direction, the magnitude of the electrical field can be expressed as

$$|E(z,r,t)| = E_0(t)\frac{\omega_0}{\omega(z)}\exp[-\frac{r^2}{\omega^2(z)} - \frac{ikr^2}{2R(z)}]\exp(-i\Phi(z,t)) \tag{3-2}$$

Where $\omega^2(z) = \omega_0^2(1+\frac{z^2}{z_0^2})$ is the beam waist at the distance z, $z_0 = \frac{k\omega_0^2}{2}$ is the diffraction length of the beam and $k = 2\pi/\lambda$, where λ is the laser wavelength.

When the medium thickness is small enough the changes in the beam diameter inside the sample due to the nonlinear refraction or diffraction can be neglected, it is considered to be an optically thin film. Such a case assumes $\mathrm{L} << \mathrm{z0}/\Delta\Phi(0)$, which significantly simplifies the problem. Inside the sample, the amplitude and nonlinear phase change $\Delta\Phi$ of the electric field are governed by

$$\begin{aligned} \frac{d\Delta\Phi}{dz} &= (2\pi/\lambda)\Delta na \\ \frac{d|I|}{dz} &= -\frac{\alpha(I)}{2}|I| \end{aligned} \tag{3-3}$$

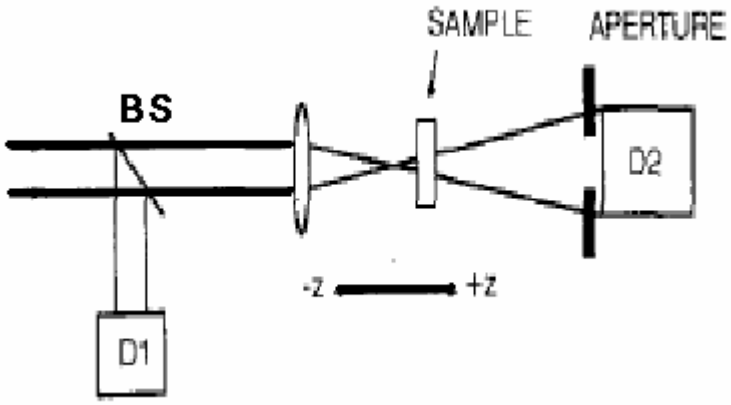

Fig.3-1 Z-scan experiment setup

Z-scan measurements are performed by moving the sample through the focus point of the incident beam. When the sample is close to the focus, the two-photon absorption increases in the presence of strong two-photon absorption. The transmission is low as the photons are absorbed by the samples. The transmission shows a valley at the focus and then increases to the original level as the sample moves away from the focus.

$$\Delta\Phi(z,r,t) = \Delta\Phi_0(z,t)\exp(-\frac{2r^2}{w^2(z)}) \tag{3-4}$$

$$\text{with } \Delta\Phi_0(z,t) = \frac{\Delta\Phi_0(t)}{1+z^2/z_0^2} \tag{3-5}$$

$\Delta\Phi_0(t)$, the on-axis phase shift at the focus, is defined as

$$\Delta\Phi_0(t) = k\Delta n_0(t)L_{eff} \tag{3-6}$$

Where $\text{Leff} = (1-\text{e}^{-\alpha\text{L}})/\alpha$, with L the sample length and α the linear absorption coefficient. I_0 is the on-axis irradiance at focus.(i.e., z=0).

The complex electric field exiting the sample E_e contains the nonlinear phase distortion

$$E_e(r,z,t) = E(r,z,r)e^{-\alpha L/2}e^{i\Delta\Phi(z,r,t)} \tag{3-7}$$

Assuming that theinput beams can be described as Gaussian decomposition, given by Weaire et al. [38], in which the complex electric field at the exit plane of the sample is decomposed into a summation of Gaussian beams by a Taylor series, expansion of the nonlinear phase term in (4.7) is given by,

$$e^{i\Delta\Phi(z,r,t)} = \sum_{m=}^{\infty} \frac{[i\Delta\Phi_0(z,t)]^m}{m!} \exp(-\frac{2mr^2}{w^2(z)}) \tag{3-8}$$

Each Gaussian beam can separately propagate through the sample, where they will be assumed to reconstruct the beam.

The transmitted power through the aperture is obtained by spatially integrating $E_a(r,t)$ up to the aperture radius R_a, giving

$$P_T(\Delta\Phi_0(t)) = c\varepsilon_0 n_0 \pi \int_0^{r_a} \left|E_a(r,t)\right|^2 rdr \tag{3-9}$$

Where ε_0 is the permittivity of the vacuum.

The normalized Z-scan transmittance T(z) can be calculated as

$$T(z) = \frac{\int_{-\infty}^{\infty} P_T(\Delta\Phi(t))dt}{S\int_{-\infty}^{\infty} P_i(t)dt} \tag{3-10}$$

Where $P_i(t) = \pi w_0^2 I_0(t)/2$ is the input power and $S = 1 - \exp(-2r_a^2/w_a^2)$ is the aperture linear transmittance, with ω_a denoting the beam radius at the aperture in the linear regime.

3.2.2 Close Aperture Z-scan

Z-scan is a simple and sensitive single beam technique for measuring the magnitude and sign of $\chi^{(3)}$ [35]. From this kind of measurement, both the size and the sign of the

third order nonlinearity can be determined. The experimental apparatus used to perform the Z-can technique is illustrated in Fig.3-1. If the nonlinear material shows a negative n_2 as the sample is translated from –z to +z, then it will act as a thin lens with a varying focal length. When the sample is far from the focal point, where the intensity is relatively low, little nonlinear refraction occurs and the transmittance remains constant. When the sample approaches the focal point, the intensity increases and causes a change in the negative self-lensing effect. A negative self-focusing effect causes a collimation or narrowing of the beam, which in turn increases the transmittance at the aperture. When the sample is scanning the +z side after passing the focal point, the self-defocusing effect increases the divergence of the beam at the aperture and causes a decreasing transmittance. For materials with a negative (positive) n_2, the profile of the Z-scan transmittance curve will consist of a peak (valley) followed by a valley (peak), as the sample is translated from –z to +z. Fig.3-2 shows the valley-peak (v-p) sequence for positive nonlinearity and a peak-valley (p-v) sequence for negative nonlinearity.

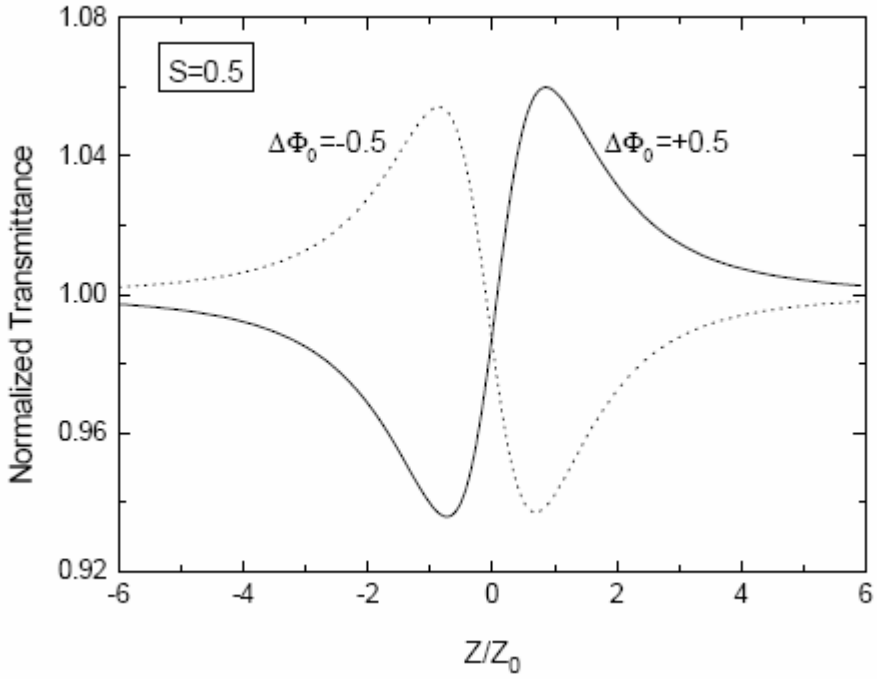

Fig.3-2 Positive (Solid line) and negative (dashed line) third-order nonlinear refraction.

One can ultimately calculate χ^3 related to a known reference under the same experimental condition. In this case, the reference following combined equation is used.

$$\chi^{(3)}_{Sample} = \chi^{(3)}_{Quartz} * \left(\frac{n_0^2 * \Delta T_{p\text{-}v}}{L_{eff}}\right)_{Sample} * \left(\frac{L_{eff}}{n_0^2)\Delta T_{p\text{-}v}}\right)_{Quartz} \quad (3\text{-}11)$$

$$\Delta T_{pv} \cong 0.406(1-S)^{0.27}\left|\Delta\Phi_0\right|, \quad (3\text{-}12)$$

$$\Delta\Phi_0 = \frac{2\pi}{\lambda} n_2 I_0 L_{eff} \quad (3\text{-}13)$$

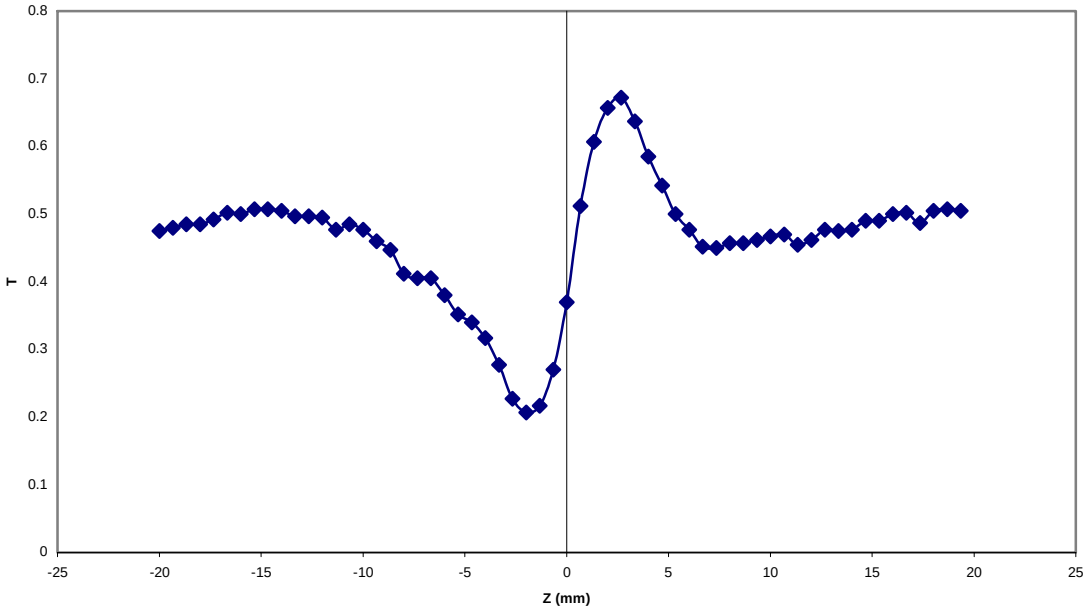

Fig. 3-3 CS_2 Clsoed Z-scan

We investigated the nonlinear refractive response, which enabled us to validate the Z-scan system setup. We calculated the n_2 of the CS_2, and we obtained a value of 4.1 X 10^{-14} cm^2/W. This is very close to the reported value of 3.1 X 10^{-14} cm^2/W [35]. Accurate measurements of n_2 were difficult to obtain at this time because of the significally large value of beta in our samples

3.2.3 Open Aperture Z-scan

There may be considerable contribution from the nonlinear absorption because of the single or multiphoton resonance effects. While Z-scan is affected by both the nonlinear refraction and the nonlinear absorption, open aperture Z-scan only measures the nonlinear absorption. The nonlinear absorption is related to the imaginary part of $\chi^{(3)}$ [35].

Using open aperture Z-scan, we can obtain the two-photon absorption (TPA). We are

concerned with low excitation regimes where the free-carrier effects can be neglected.

Therefore, (3-3) can be rewritten as

$$\alpha(I) = \alpha + \beta I \tag{3-14}$$

The irradiance distribution at the exit surface of the sample as

$$Ie(r,z,t) = (I(r,z,t)e^{-\alpha L})/(1+q(r,z,t) \tag{3-15}$$

Thus, when the open aperture (S=1) Z-scan is performed, the nonlinear absorption coefficient can be calculated from the normalized transmittance by using

$$T(z,S=1) = \sum_{m=0}^{\infty} \frac{[-q_0(z,0)]^m}{(m+1)^{3/2}} \qquad |q_0|<1 \tag{3-16}$$

If we only consider two-photon absorption effect, the third-order nonlinear susceptibility can be separated as following:

$$\chi^{(3)} = \chi_r^{(3)} + i\chi_{im}^{(3)} \tag{3-17}$$

Where the imaginary part is contributed to TPA coefficient

$$\chi_{im}^{(3)} = \frac{n_0^2 \varepsilon_0 c^2}{\omega} \beta \tag{3-18}$$

3.2.4 CdSe Open Z-scan results

A mode-locked YAG laser provided the laser pulses with 25-ps duration at 355 nm, 532 nm and 1064 nm at a 20-Hz repetition rate with energies per pulse ranging from few microjoules to several mJ [37]. The intensity of the incident beam was adjusted by an attenuation setup consisting of a half wave plate and two crossed Glan-Thomson polarizer. In the experiment, the laser beam was tightly focused to a $1/e^2$ beam radius of about 90 μm. The light through the aperture was detected and

recorded, using a fast detector (Thorlabs Inc., model 201/579-7227), Unidex^{TM} 11 and Stanford Research System interfaced with a computer.

Here is the CdSe Z-scan at 532nm and the fitting data where m=5 in 3-16.

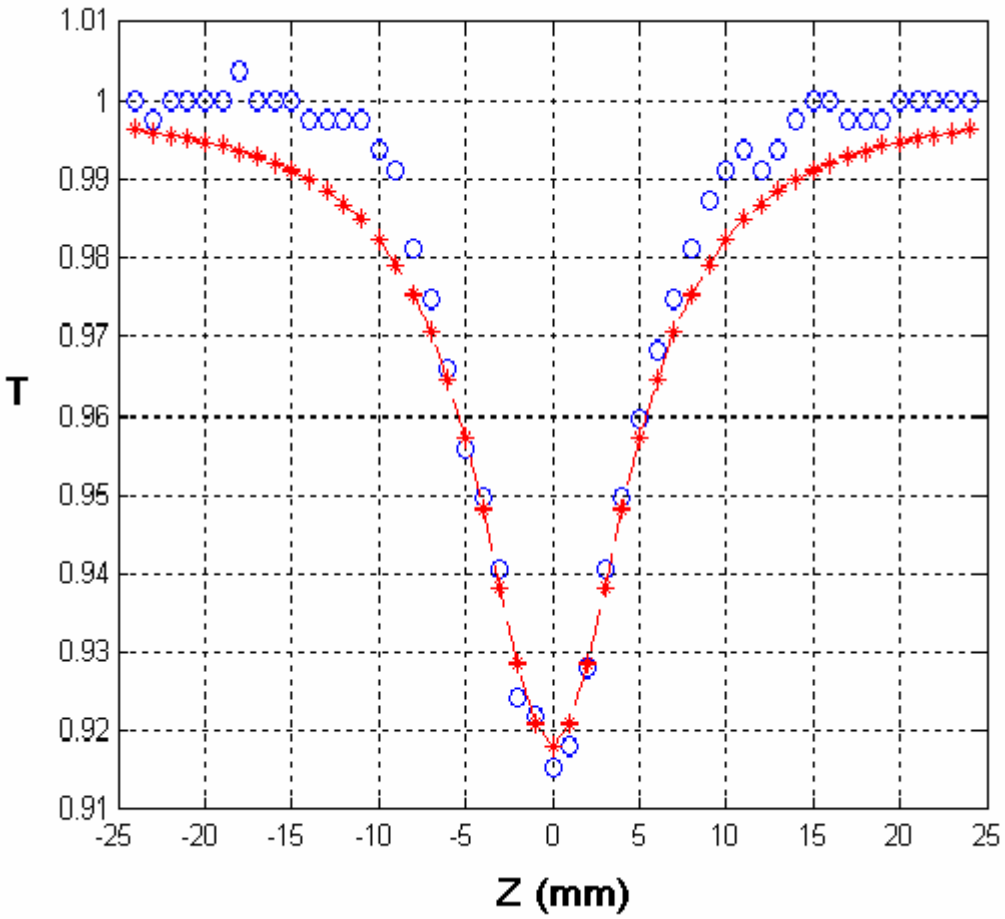

Fig.3-4 CdSe Open Z-scan

q=0.26, Io= 2.8923GW/cm^2, L=3x10^{-4}cm, and $\beta = 304$cm/GW.

These results show the large values for the magnitude of the nonlinear coefficient β. This strong two-photon absorption at wavelength 532 nm, is at least one order of magnitude bigger than all the previously reported values for similar nanocomposites system [39].

3.4.5 Transmission measurement of CdS QD film

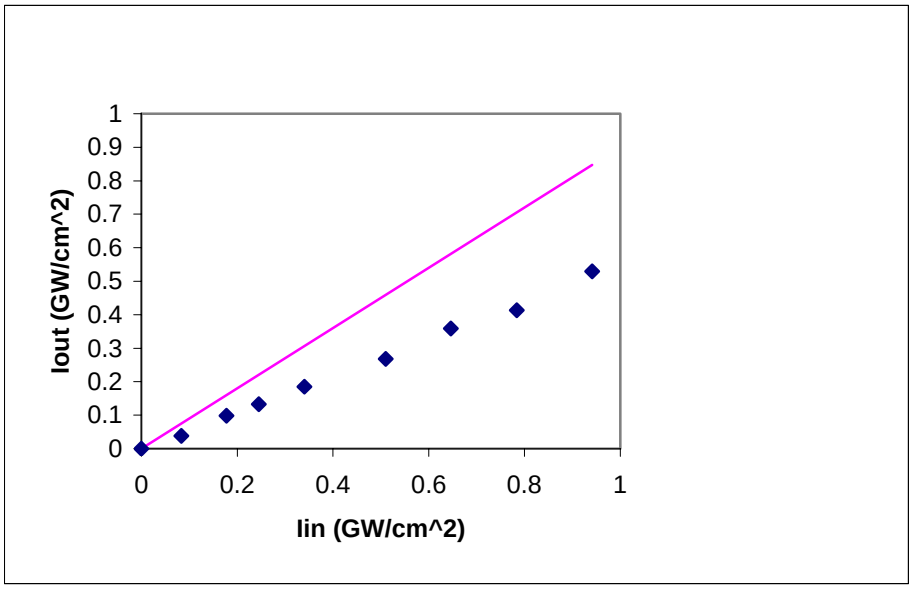

Fig. 3-5 Nonlinear transmission Measurement

Doted data is measured data, and solid line is the linear absorption curve

The result for the nonlinear transmission measurement for an approximately 9 μm-thick thin film is shown in Fig.3-5. The control of input intensity was obtained by a combination of half-wave plates and polarizer.

The optical limiting behavior comes from the two-photon absorption of the sample.

The experimental data were fitted with the expression:

$$I_{out} = I_{in} e^{-\alpha(I)L} \tag{3-19}$$

$$\alpha(I) = \alpha_0 + \beta I \tag{3-20}$$

where α_0 is the linear absorption coefficient, β, respectively, the two-photon absorption coefficients. We obtained a β value of 788cm/GW (the two-photon absorption coefficient, β, was reported to be 3.2 cm/GW for bulk CdS at wavelength 610 nm [34]).

This TPA coefficient is almost two orders of magnitude greater than that in the CdS-Nafion film measured by He et al. [18] who reported a β value of 9.5 cm/GW, at wavelength 780nm.

Reasons for high nonlinear absorption coefficient are considered to be due to quantum confinement effects. First, complete extraction of water in micelles by heat treatment produce strong modified surfaces at which the decylamine molecules are close to the cadmium atoms. This enhances the dielectric confinement effect, i.e. increase the excited state lifetime of capped CdS nanoparticles, and can lead to further enhancements of two-photon absorption.

Wang et al. reported a value of β for Chitosan-ZnS QDs films, which is of the same order of magnitude as our result. In both cases the surface of the inorganic nanoparticles was chemically modified by an organic capping agent. Thus one can deduce that well passivated QDs may show enhanced nonlinearity due to the chemically controlled surface.

In addition, we notice that the absorption spectrum of the self-standing surfactant micelles (i.e. without the capped inorganic nanocrystals) shows a resonant transition with the semiconductor excitonic peak. The intensity of this absorption is rather small if compared with the strong absorption of the composite material, however we cannot exclude the possibility of an interaction between organic/ inorganic excitons. Theoretical studies show that the Wannier exciton of 3-D ordered semiconductor QDs arrays incorporated in an organic host can be coupled with the Frenkel exciton of the organic medium and at resonance of the two exciton*s*, a hybrid exciton may appear in

the system. The mixed state has a large exciton radius, large oscillator strength, and very large optical nonlinearity. However, in order to fully describe the physics of our system, further investigation is required.

3.4.6 CdS in dendrimers

In CdS-DAB-QD, previous work [36] didn't observe large two-photon absorption phenomena, which may have been due to several factors including, but not limited to, a low concentration of QDs, dendrimer structure, and/or compatibility of materials. However, the results indicate relatively large values for the magnitude of the nonlinear coefficient ($|\chi^{(3)}| > 10^{-10}$ esu) for the pristine dendrimer and the composite QDs at several wavelengths. The pristine dendrimer nonlinear response coefficient is positive at 1064nm and 532 nm and negative at 355 nm. This sign reversal and the fact that the values are very close, strongly suggests that the 532nm and 355 nm excitations are at the opposite sides of the two photon absorption band. The G5-DAB-QD response is negative at all three wavelengths. The sign difference at 532 nm and 1064 nm suggests that the NLO response of the G5-DAB-QD is dominated by the QD exciton contribution to the nonlinear response through two photon resonance enhancement. The G5-DAB-QD shows a smaller response at 1064 nm compared to 532 nm and a significantly larger response at 355 nm. The enhanced response at 532 nm is expected since two-photon absorption is significantly stronger at this wavelength compared to measurement at wavelength 1064 nm. The 355 nm wavelength is close to the QD exciton band and shows significant linear absorption

and a significant enhancement of the nonlinear response related to exciton bleaching effects.

CdS-G5-QD shows a high value of n_2, hence it could be the ideal material for the optical switching device.

Table 3-1. Summary of nonlinear susceptibility results using 30 ps pulses [37]

Wavelength (nm)	*χ (3) G5-DAB (esu)*	*n_2 G5-DAB (cm^2/GW)*	*χ (3) G5-DAB-QD (esu)*	*n_2 G5-DAB-QD (cm^2/GW)*
1064	3.9×10^{-10}	9.1×10^{-3}	-7.5×10^{-10}	-1.7×10^{-2}
532	5.8×10^{-10}	13×10^{-3}	-2.2×10^{-9}	-5.1×10^{-2}
355	-2.8×10^{-10}	-6.5×10^{-3}	-5.3×10^{-9}	-12.4×10^{-2}

3.3 Conculsions

We have investigated three quantum dots material, CdS capped with reverse micelles, CdSe capped with reverse micelles, and CdS in dendrimers (most of this was done by Dorsinville). Considering the results it appears clear that they have large nonlinear properties. CdS and CdSe QDs capped with reverse micelles show strongest two-photon absorption. The β values we obtained up to 304cm/GW (CdSe) and 778cm/GW (CdS) are among the highest two-photon absorption coefficient in the same kinds of semiconductor nanomaterials. The CdS in dendrimer G5 sample shows high third-order nonlinear refraction, -5×10^{-10} esu [37]. This work was done before. However, further investigation needs to be preformed. For example,

analyzing the different polymers and increasing solution concentration in order to understand the physics of these promising nanostructures.

Chapter 4 Effects of Excited State Absorption on Two-photon Absorbing Materials

4.1 Introduction

Organic materials have very large two-photon absorption (TPA) cross-section [1-3], which are very useful in several applications. These applications include, but are not limited to, optical data storage [4-5], microfabrication [6-10], photoconductors and photovoltaics [11], markers for genomes and proteins [12-13], biological and medical detectors [14-15], optical limiters [16-18], biomimetric electromagnetic devices [19], nanopatterning of inorganic/organic materials [20-21] and photomedicine/photodynamic therapy [22]. To achieve high-density 3D data storage, one of the key elements is the size of the radius pulse shape at different depths in the materials. In microfabrication, high resolution requires small beam size to achieve high resolution.

The wide range of applications of two-photon absorption processes makes it particularly useful to have a detailed method for numerical investigation because many of the strongest TPA molecules are hybrid chromophores. These complex molecules exhibit a hybrid photo-activated energy level system in which the TPA level is coupled to an excited state absorption (ESA) level. This hybrid arrangement creates a complex dynamical system in which the electron concentration of every photo-activated energy level must be taken into account in order to determine the actual optical properties. We determine the details of both the spatial and temporal shapes at any propagation distance. This analysis enables us to determine any

distortions arising during propagation. Most traditional calculations of the laser matter interaction make simplifying assumptions [23-24] about the optical field and the energy states of the molecular system. In most cases, numerical calculations [25-27] solve the rate equations and propagation equation in the time and propagation distance, neglecting distortions that occur in the radial domain. Meanwhile, many papers [28-29] focus on the optical transmission; while neglecting the actual optical pulse shape. For example, we find that in some circumstances an enhancement of the absorption at high input energies can actually result in significant pulse distortion, which may actually result in poor device performance. In applications such as pulse shaping and microfabrication [30-32], understanding the pulse distortion is a key problem in achieving enhanced resolution. In this paper, we demonstrate the pulse shape distortion caused by electrons oscillating between the first and second excited state.

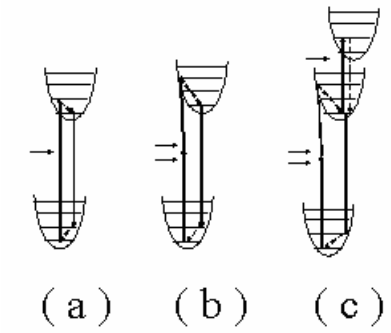

Fig. 4-1. Schematic diagrams of various photon absorption processes. (a) One photon absorption. (b) Two photon absorption. (c) Two photon absorption followed by one photon absorption.

We model optical beam propagation through multiphoton absorbing materials and

describe the numerical analysis of the complex interaction of the optical pulses with these hybrid systems. The numerical method presented here calculates the spatiotemporal details of the electron population densities of each photo-activated energy level as well as the pulse shape in space and time for a single pulse, which enables us to predict new properties. Fig.4-1 shows schematic diagrams of single photon absorption, two-photon absorption and two-photon absorption coupled to an excited state absorption.

4.2 Theoretical Description

Our numerical method is quite general and applies to a class of molecules exhibiting both TPA and ESA. For example, there is a series of symmetrical stilbene and triarylamine derivatives, which have very strong donor and strong acceptor, such as 4,4′-bis (diphenylamino) stilbene (BDPAS) [33], and N^4-diphenyl-4,4′ diaminobiphenyl [34]. These molecules exhibit similar values of TPA and ESA absorption over a broad spectral range in the visible and red-NIR region. The molecules have quadrupolar symmetrical structure and have excellent solution in nonpolar organic solvents. In this paper, we compare our results with the one example [1] of these series.

One of our efforts is to understand the electronic structure, decay system and the absorptive properties. The energy levels have the following properties. N_0 is the electron number density of the ground state, N_1 is the electron number density of the first excited state reached by two-photon absorption, and N_2 is the electron number density of the excited state reached by a single photon.

The rate equations for the system shown in Fig. 4-2 are given by

$$\frac{\partial N_0}{\partial t} = -\sigma_{TPA} N_0 \frac{I^2}{2\hbar\omega_0} + k_{10} N_1$$
$$\frac{\partial N_1}{\partial t} = \sigma_{TPA} N_0 \frac{I^2}{2\hbar\omega_0} - \sigma_{12} N_1 \frac{I}{\hbar\omega_0} - k_{10} N_1 + k_{21} N_2 \qquad (4\text{-}1)$$
$$\frac{\partial N_2}{\partial t} = \sigma_{12} N_1 \frac{I}{\hbar\omega_0} - k_{21} N_2$$

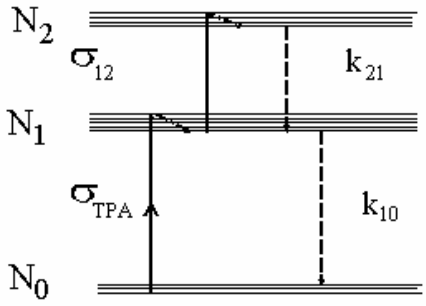

Fig. 4-2 Energy level diagram for the chromophore. The parameters are σ_{TPA} = 8.0×10^{-48} cm^4 s photon^{-1}, σ_{esa} = 2.0×10^{-16} cm^2, k_{10} = 1.8×10^{-3} ps^{-1}, k_{12}= 2×10^{-2} ps^{-1}. The solid lines represent the photon absorptions and the dashed lines are the photon decays.

where N_i is the electron number density of the state I, $\sigma_{i,j}$ is the absorption cross-section for electron pumping from N_j to the state j, and $k_{i,j}$ is the decay rate from the state i to the state j.

The propagation equation of the pulse intensity is given by

$$\frac{dI}{dz} = f'(z) = -\sigma_{TPA} N_0 I^2 - \sigma_{12} N_1 I \qquad (4\text{-}2)$$

Eqs. (4-1)-(4-2) are solved to obtain the optical beam properties and the molecular electron density properties. The approach described here may be significant for TPA problems in several applications because many molecular systems exhibiting TPA also involve some ESA either, within the molecule, or to its surroundings. Hence, these

calculations are useful for a wide range of problems and produce a more realistic result for many molecular systems than are now described solely by TPA equations. By discretizing both temporal and spatial dimensions at each z step, the detailed nature of the change in electron population densities can be described at each stage of the laser propagation through the material.

Next we describe the numerical method used in the calculations [35-37]. We define a discrete time, space and radius grid such as $t \to t_i$, $z \to z_n$, $r \to r_j$. For convenience, the total electron population density is normalized by the initial population density, N_T such that $\mathbb{N} = N_P / N_T$, where $\sum_{p=0}^{2} N_p / N_T = 1$.

The population density vector is given by [35-37]

and matrices $\hat{G}$, $\hat{H}$, and $\hat{F}$ contain the terms in Eq. (4-1) that are independent of the intensity, multiply the intensity itself, multiply the intensity squared, respectively, and $\hat{M}$ is the sum of the three matrices. We expand the Taylor series in Eq. (4-3) to second order, which we have found sufficient [35-37].

$$\vec{\mathbb{N}}(z_{n+\frac{1}{2}}, t_{i+\frac{1}{2}}) = \exp(t_0 \int_{t-\frac{1}{2}}^{t+\frac{1}{2}} \hat{M} dt') \vec{\mathbb{N}}(z_{n+\frac{1}{2}}, t_{i-\frac{1}{2}}) = \sum_{k=0}^{\infty} \frac{1}{k!} (\hat{R})^k \vec{\mathbb{N}}(z_{n+\frac{1}{2}}, t_{i-\frac{1}{2}}) \tag{4-3}$$

$$\begin{aligned} \hat{R} = {} & t_0 \Delta t \, \hat{G} + \hat{H} \frac{t_0 \Delta t}{\hbar \omega_0} \frac{1}{2} [I(z_n, t_i) + I(z_{n+1}, t_i)] \\ & + \hat{F} \frac{t_0 \Delta t}{2 \hbar \omega_0} \frac{1}{2} [I^2(z_n, t_i) + I^2(z_{n+1}, t_i)] \end{aligned} \tag{4-4}$$

The propagation equation is given by

$$f'(z_n, t_i) = -\frac{N_T}{2} \left[\sigma_{TPA} \tilde{\mathbb{N}}_0 I^2(z_n, t_i) + \sigma_{12} \tilde{\mathbb{N}}_1 I(z_n, t_i) \right] \tag{4-5}$$

where

$$\tilde{\mathbb{N}}_p = \mathbb{N}_p\left(z_{n+\frac{1}{2}}, t_{i-\frac{1}{2}}\right) + \mathbb{N}_p\left(z_{n+\frac{1}{2}}, t_{i+\frac{1}{2}}\right) \tag{4-6}$$

and p=0, 1.

Because the coupled Eqs. (4-3) and (4-5) are inter-related, we iterate them to obtain convergence. The kth and k+1th iteration are given by

$$\begin{aligned}\vec{\mathbb{N}}^{(k)}(z_{n+\frac{1}{2}}, t_{i+\frac{1}{2}}) = \exp(t_0 \Delta t\, \hat{G} + \hat{H}\frac{t_0 \Delta t}{\hbar\omega_0}\frac{1}{2}[I(z_n, t_i) + I^{(k)}(z_{n+1}, t_i)] \\ + \hat{F}\frac{t_0 \Delta t}{2\hbar\omega_0}\frac{1}{2}[I^2(z_n, t_i) + I^{(k)2}(z_{n+1}, t_i)])\vec{\mathbb{N}}(z_{n+\frac{1}{2}}, t_{i-\frac{1}{2}})\end{aligned} \tag{4-7}$$

$$\begin{aligned}I^{(k+1)}(z_{n+1}, t_i) = I^{(k)}(z_n, t_i) + f'^{(k)}(z_n, t_i)\Delta z \\ + f''^{(k)}(z_n, t_i)\frac{\Delta z^2}{2}\end{aligned} \tag{4-8}$$

We have found that two iterations are sufficient. In the next section we compare our numerical calculations with prior results and show excellent agreement. Then we investigate the relationship of the radial and temporal shapes of the pulse to the excited state lifetimes and transmission curves.

4.3 Results and Discussion

4.3.1 Comparison with Prior Results

We simulate a multiphoton process, two-photon absorption followed by an excited state absorption. The two photons are absorbed simultaneously, and pump electrons into energy N_1 from the ground state as shown in Fig.4-2. In the following discussion, we present the dynamics of the electron population redistribution in all energy levels, and show how the optical pulses evolve.

In the optical processes, the transmission as well as the temporal and spatial properties is very important. Here, we first validate our numerical simulations by calculating the transmission curve as a function of input energy and compare it to published results. It is convenient to define the transmission, T as the ratio of the output energy to the input energy

$$T = E_{out} / E_{in},$$
$$E_{out} = \int 2\pi dr \int dt\, I(r, L, t), \tag{4-9}$$
$$E_{in} = \int 2\pi dr \int dt\, I(r, 0, t),$$

where L is the thickness of the material. Silly et. al.[1] have investigated optimized chromophores combining high solubility, low linear absorption and large nonlinear absorption in the visible to near infrared region. These chromophores exhibit large TPA and ESA, where the parameters are given in the Table 4-1.

Table 4-1. Material Parameters for Used the Chromophore

Material Parameters[1]	
λ	740 nm
σ_{tpa}	8.0 x 10^{-48} cm^4 s $photon^{-1}$
σ_{esa}	2.0 x 10^{-16} cm^2
τ_{10}	550 ps
τ_{21}	50 ps

Using our numerical method, we have calculated the transmission as a function of incident energy for these chromophores. The solid line in Fig.4-3 shows our numerical calculation and the dots are obtained from the published results [1]. As

shown in Fig.4-3, our calculations are in very good agreement with published results for the same wavelength of 740nm, pulse duration (full width half maximum) of 0.11ns, beam diameter of 100μm and 1cm thickness.

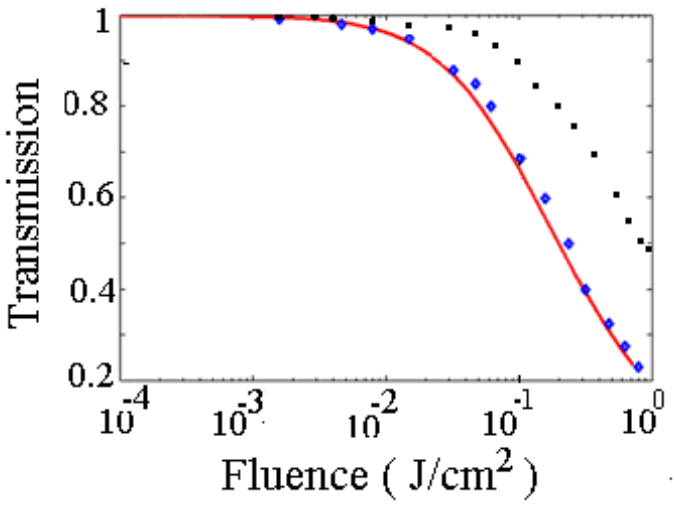

Fig.4-3. Comparison of our numerical code with published work. The solid line is our calculation. The diamonds were obtained from [1] and the squares correspond to the theoretical TPA calculation.

In Fig.4-3, we find that the absorption is nearly negligible up to a fluence (The fluence is defined as the integrated pulse over time and radius divided by the pulse area at the beam waist.) of about 10^{-2} J/cm^2. This is because there is little linear absorption in the material, which is one of the advantages of using TPA materials. As the fluence increases, the transmission decreases strongly due to nonlinear absorption. Fig.4-3 shows the TPA contribution [38] to the transmission, which reaches a maximum value of only ~0.5; therefore, we conclude the ESA absorption contributes substantially to the total transmission. We find that for an input fluence of 0.1 J/cm^2 the intensity drops approximately 50% within a thickness of 1mm. In

addition to the "traditional" transmission curve we calculate the spatiotemporal properties as the optical pulse propagates through the material, as well as details of the population density transitions to the various levels. In the next section we calculate the changes in the population levels for an input fluence of 1.25 J/cm^2.

4.3.2 Characteristics of population densities, optical pulse shapes

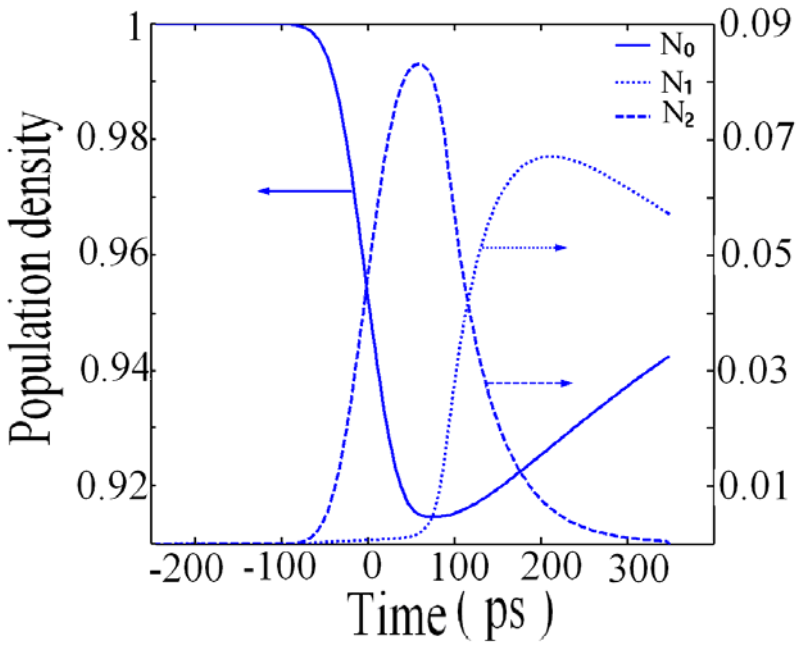

Fig. 4-4. Population density of the three levels of the molecular system as a function of time at r=0**.** The solid line corresponds to the population density on state N_0, the dotted line to state N_1, and the dashed line to N_2.

In Fig. 4-4, we show the population densities in each of the three levels at r=0. In order to compare the effects of the excited state lifetime and the pulse width we use an input laser pulse with a normalized intensity equal to one, a pulse width of 55 ps (1/e half-width) and a radial beam waist of 50 μm. We selected this pulse duration

because it is slightly greater than the lifetime of the ESA state, which enables us to examine the novel features of the ESA absorption following TPA absorption. When the pulse intensity is below its 1/e value, it is easy to observe the population oscillations between the ESA state and the TPA state, as described later in the paper. At a propagation distance of 1 mm (Fig. 4-4), we observe the leading edge of the pulse excites about 10% of the electrons from the ground state. First, TPA excites about 10% of the electrons to N_1, from where they are pumped to N_2 by ESA. This behavior results in a very low population in N_1 for the leading part of the pulse. The biggest value of N_2 and the smallest values of N_0 occur at about the same point in time (t~50 ps). At the leading edge of the pulse, the population of N_0 decreases, while the population of N_2 increases by almost the same amount. After the population of N_2 reaches its peak value, the population of N_1 increases because of electron relaxations from N_2, even though the absorption due to TPA is decreasing after the center of the pulse. In this case, electrons on N_1 either relax to N_0 or are excited to N_2. The lifetime of N_1 is eleven times greater than the lifetime of N_2. This difference leads to accumulation of the electrons in N_1. As the intensity at the trailing edge of the pulse decreases, TPA absorption decrease too; however, the ESA absorption still continues to increase because of increased population in N_1. At t~180 ps the population of N_1 reaches its peak value and then decreases because the number of electrons decaying from N_1 is greater than the number from N_2. However, after initially decreasing, the electrons on N_0 increase slowly (t~55 ps), and eventually all of them return to the ground state.

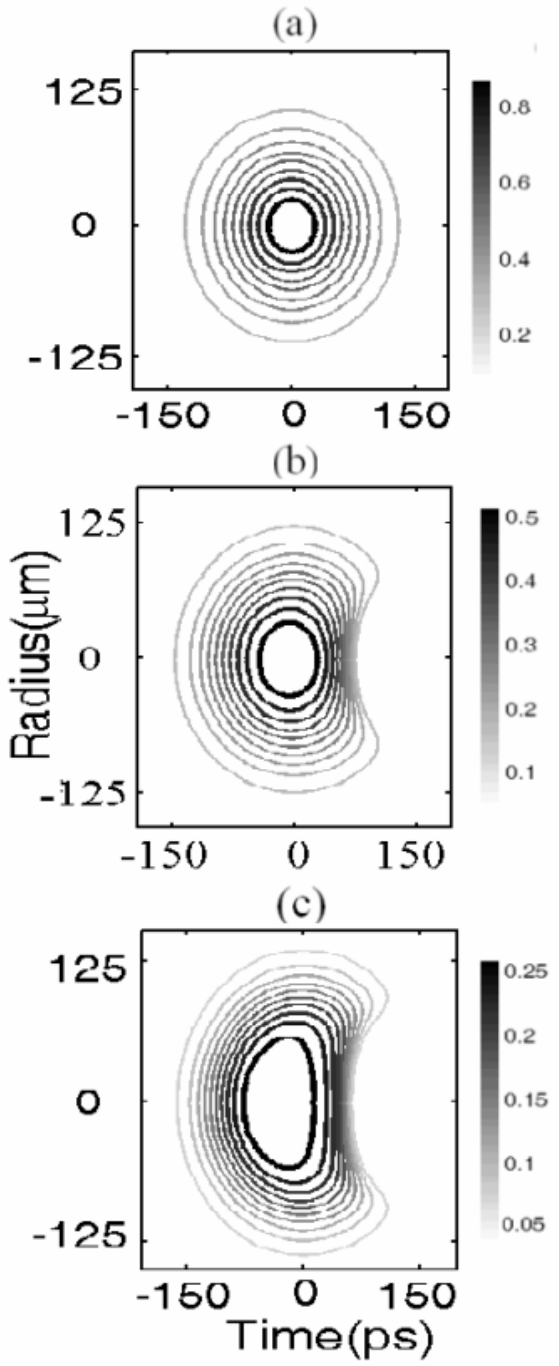

Fig.4-5. Contour plots of the pulse intensity for input fluence of 1.25 J/cm^2, pulse width of 55ps and pulse beam radius of 50μm at various sample thicknesses. The side bar gives the scale for the plots. (a): the pulse at a sample thickness of 0mm. (b): the pulse at a sample thickness of 2mm. (c): the pulse at a sample thickness of 10mm.

Next we investigate the spatiotemporal characteristics of the pulse. Previous results [38]have shown a time shift of the pulse with propagation distance; however, the radius was kept constant and there was no reported observation of the accompanying radial distortion. In Fig. 4-5, we present the pulse shape change in the time and radial domains. Contour plots in which all the points on a given line have the same the intensity represent the pulse shapes. As the pulse propagates, the intensity at the center decreases. The leading and trailing edges of the pulse show very different behavior as seen in Fig.4-5. As we discussed for Fig. 4-4, the population N_1 maintains a low value until t~55ps. The population of N_1 is responsible for the abnormal absorption at the trailing edge, i.e. the trailing edge of the contour plots shift towards the center. There is more distortion at the distance of 10mm compared to 2mm because of the accumulated affects during propagation. As we increase the fluence, the distortion becomes even more complex.

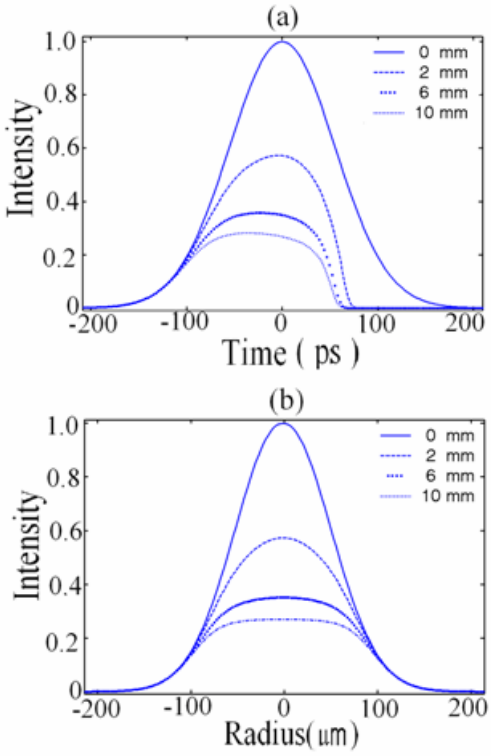

Fig. 4-6. Intensity as a function of time and radius for input fluence of 1.25 J/cm^2. The four propagation distances 0 mm, 2mm, 6mm, and 10mm are labeled in the figure. (a): intensity as a function of time at r=0. (b): intensity as a function of radius at t=0.

In Fig.4-6 we plot the intensity as a function of time at r=0, and as a function of radius at t=0. Figure 6(a) shows the pulse in the time domain. We plot the pulse at four distances: 0mm (solid line), 2mm (dash line), 6mm (dot line) and 10mm (dash-dot line). We find that both the peak value of the pulse and the trailing edge shift in time as the pulse propagates. In Fig.4-6(a) we see the peak value of the pulse shifts towards the leading edge of the pulse because there is more absorption at the trailing edge. As shown in Fig. 4, the electrons oscillate between N_1 and N_2 such that the intensity at the training edge of the pulse (Fig.4-6(a)) is depleted. As observed by

the trailing edge of the pulse in Fig.4-6(a), the time shift of the pulse tail varies throughout the thickness of the material. However, the largest time shift of the trailing edge or pulse tail occurs at a thickness of 2mm, and then it decreases with increasing thickness (i.e. 6mm and 10mm).

Fig.4-6 (b) shows the intensity as a function of radius. As can be seen from the figure, the initial Gaussian shape becomes flat-topped as it passes through the material with most of the absorption occurring in the center of the pulse.

4.3.3 Effects of the variation of ESA lifetime

We have shown that our numerical method gives good agreement with previous published results [1]. However we can also use our code to examine and/or predict new phenomena. In some materials, the lifetime of the excited state N_2 is on the order of a few picosecond [26][39]. The chromophore used in the fiber array [26], has an ESA lifetime of only ~1ps, which is 100 times faster than the lifetime of the TPA state. Therefore, we investigate the effects of shorter lifetimes for the ESA state, while keeping the TPA lifetime fixed. We find that a shorter lifetime leads to better absorption at high input energy, but results in greater pulse shape distortion. While most traditional calculations focus on the transmission curves, we find that, in some cases, this emphasis could be misleading. Fig. 4-8 shows transmission curves for two values of the excited state lifetime (τ_{21}=5ps and 50 ps) with the other parameters the same as those used in Fig. 4-3. When the excited state (N_2) lifetime is close to or smaller than the pulse duration, pulse distortion can occur especially for high input energy. From the above discussion, we observed only a small pulse distortion when

the excited state lifetime was close to the pulse duration, and the lifetime of N_1 was significantly greater than the pulse duration. In order to examine the effects of a shorter excited state lifetime, we change τ_{21} to 5ps, while maintaining the same values for the other parameters. Because the electrons oscillate faster between N_1 and N_2, the transmission is reduced at high input energy.

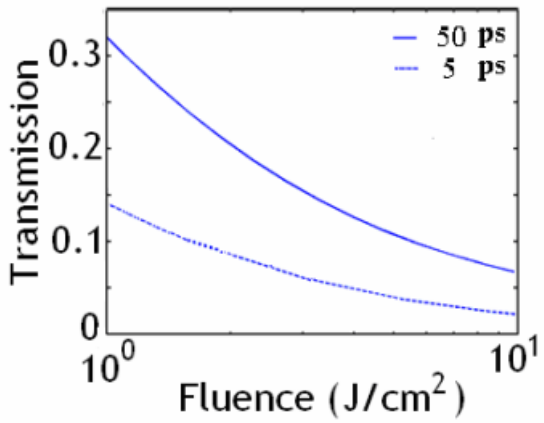

Fig. 4-7. Transmission as function of fluence at a wavelength of 740nm. The excited state decay times are $\tau_{21} = 50ps$ and $\tau_{21} = 5ps$.

As we see in Fig. 4-7, the transmission (dotted line) for τ_{21}=5 ps decreases by a factor of 2 to 3 relative to the transmission (solid line) for τ_{21} = 50ps. However this reduction in transmission is accompanied by severe distortion of the pulse, which may reduce the benefits of the increased average absorption. In order to examine this we calculate the contour plots for the two values of τ_{21} as shown in Fig.4-8.

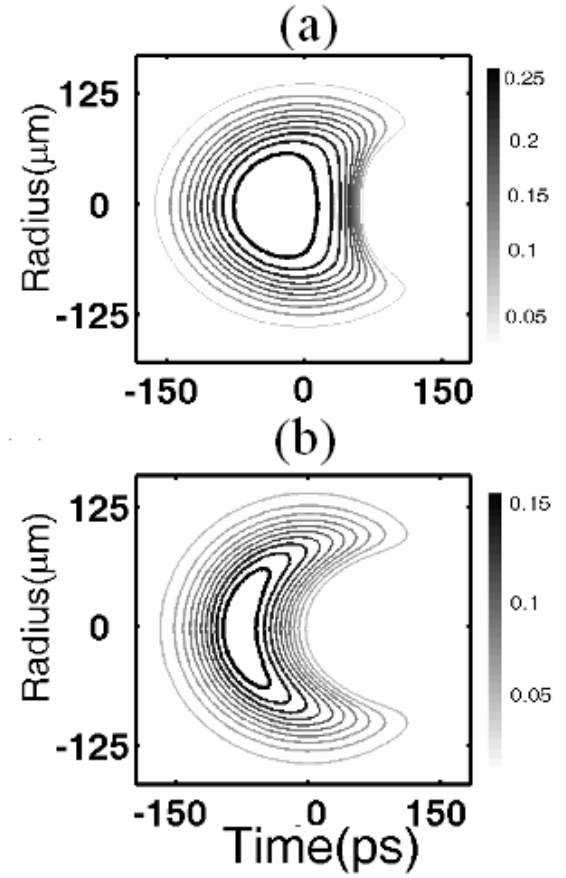

Fig.4- 8. Contour plots for different excited-state lifetimes for a wavelength of 740nm and input fluence of 2.5 J/cm^2 . The side bar gives the scale for the plots. (a): values of the decay rates are given by $\tau_{21} = 50 ps$ and $\tau_{10} = 550 ps$. (b): values of the decay rates are given by $\tau_{21} = 5 ps$ and $\tau_{10} = 550 ps$.

In Fig. 4-8 (a) and Fig. 4-8 (b), we compare the contour plots for an input fluence of 2.5 J/cm^2 at τ_{21} = 50 ps and 5 ps, respectively. Fig.4-8(a) shows some depletion of the pulse at the trailing edge. However in Fig.4-8 (b), the intensity drops off dramatically with spatial depletion occurring at the center of the pulse. At the trailing half of the pulse, only the outer edge of the intensity is left. Of course, the distortion is also related to the lifetime of N_1. If electrons cannot stay enough long enough on N_1, then there would be few electrons oscillating between N_1 and N_2 due to ESA

absorption, which is decreasing the transmission**.**

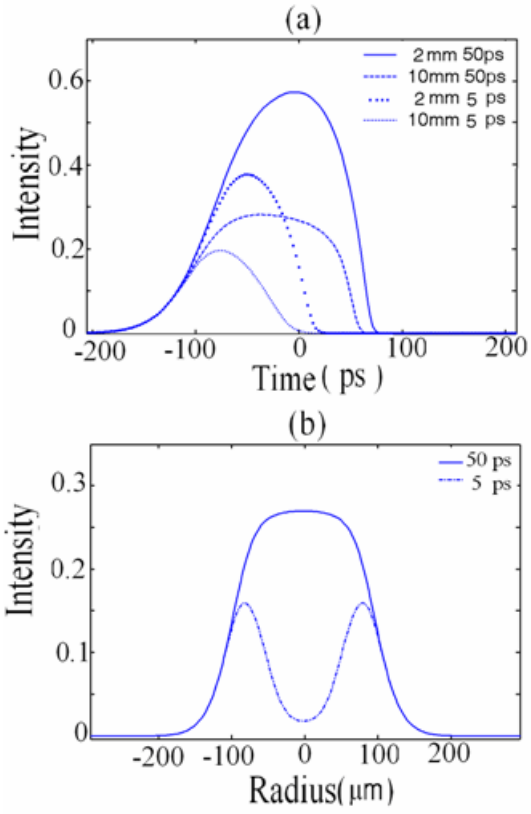

Fig. 4-9 Intensity plots as a function of time and radius for a wavelength of 740nm and input fluence of 2.5 J/cm^2. The excited state decay times are $\tau_{21} = 50 ps$ and $\tau_{21} = 5 ps$. The TPA decay time is $\tau_{10} = 550 ps$. (a) Intensity as a function of time at r=0 for sample thicknesses of 2mm and 10mm. (b) Intensity as a function of radius at t=0 for a sample thickness of 10mm.

Next we examine the pulse shapes in the time (Fig.4-9(a)) and radial (Fig.4-9 (b)) domains. In Fig. 4-9 (a), we give a comparison for two thicknesses: 2mm and 10mm. It is very clear that the smaller the excited-state lifetime and the thicker the material, the bigger the pulse shifts. We observe that as we change τ_{21} to 5ps the pulses decrease more on the trailing edge. In Fig. 4-9 (b), we examine the radial

dependence and show that the center of the pulse flattens for τ_{21}=50 ps; but the dotted line shows the pulse shape declines nearly to zero at the center when τ_{21}= 5 ps. Therefore when considering nonlinear absorption it may not be sufficient to investigate only the integrated pulse transmission.

4.4 Conclusions

We have derived a numerical method to dynamically analyze the multiphoton processes in TPA and ESA materials. The calculation agrees well with published work. We also investigated the population densities for every level. The optical pulse shape was shown to be distorted in both space and time. In the time domain the pulse shifts toward the leading edge and the trailing edge is absorbed. The changes in the radial domain ranged from pulse flattening to pulse depletion at the center. We also varied the excited state lifetime and found that while it improved the transmission curve, the pulse became dramatically distorted which may lead to poor device performance.

Chapter 5 Dynamics of a Multilevel Molecular Absorber Interacting with a Train of Optical Pulses

5.1 Introduction

Laser pulse interactions with multilevel systems are of considerable interest in many fields such as all optical processing for communications and computing [1-2], nonlinear absorbers [3], multiphoton microscopy for biological imaging [4], and semiconductor nanoparticles [5]. Since the nonlinear absorption and population dynamics in such systems can have a very complex behavior, most investigations of these systems often assume that a single optical pulse, or a very long repetition rate pulse train interacts with the material. Approximate analytical solutions have been shown to be useful in describing the level population dynamics, especially when the number of levels is assumed to be reduced and the input pulse widths fall within a specified range depending on certain level decay rates [6]. It has also been shown that the exact shape of the laser pulse (flat-topped, Gaussian, hyperbolic secant) has very little effect on the nonlinear absorption of the single pulse energy so that modeling can be simplified by assuming the pulse to be flat-topped [7]. However, when the form of the excitation is more complex than a simple single pulse excitation or the repetition rate is high compared to the rates describing the population dynamics, the previously mentioned approximations no longer apply.

The damage threshold for various photo detectors, including the cornea, can exhibit repetition rate dependence [8-9]. To protect such detectors, nonlinear

absorbers will need to be developed that are operable at high repetition rates or when subjected to complex excitations. Recent Z-scan experimental investigations have shown that multiple pulse excitation of some of the materials being investigated for nonlinear absorbers display dramatically different behavior than single pulse excitation [10-11]. There have been many studies of nonlinear absorbers using various pulse durations; therefore only some examples are given [3, 5-7, 10-22]. As lasers become more intense and exhibit increased repetition rates, a detailed quantitative description is required to describe the transient response of the material.

Because of the large number of variable parameters involved in these systems, experimental methods to explore the parameter space would be greatly enhanced by a detailed numerical model. A five level model involving singlet and triplet states is often used to describe the system [12, 15, 21-25]. In this paper, we describe a numerical model that solves the laser matter interaction in detail in three-dimensional space and time for all of the levels of the five level systems. The upper excited state levels that are frequently omitted in traditional calculations [3] are included in our numerical method. Furthermore, we show the significance of including the radial domain in the calculation, which is also traditionally neglected, and demonstrate the changes in the radial behavior of both the optical pulse shape and the population density for various input conditions. We provide initial results for multiple pulses with pulse widths of nanosecond and picosecond durations. To our knowledge, these results present the most detailed investigation of these systems under such complex excitation schemes and the knowledge provided here can greatly enhance the

understanding of the complex dynamics of the level populations and the evolving optical pulse shapes, making the interpretation of experimental results more concise. Additionally our numerical techniques can be used to predict new phenomena by examining a wide range of parameter space, allowing us to investigate novel engineered materials whose properties give rise to new behavior for optical pulse trains.

This paper is structured as follows: In section II we present our model for the propagation equation coupled to the multilevel rate equations with multipulse excitation. In section III we start by using a single pulse version of our numerical method to compare the results to experimental data on C_{60} [13]. This reference was selected, in part, because it contained experimental results for both nanosecond and picosecond pulses for a five level system. We then investigate the interaction of a train of pulses with a multilevel molecular system in a class of well-known materials, i.e. the phthalocyanines [14]. These materials were selected, in part, because they are quite representative of the class of five level reverse saturable absorbers. In section IV, we optimize the optical parameters to gain the best results. We show that the pumping rates, population density distribution with pulse width, repetition rate, beam waist, intensity of the laser, and the kinetics of the multilevel system dominate the physical behavior.

5.2 Model

We model the interaction of multiple pulses with the nonlinear material by first considering a description of the light pulses. This description is motivated by an

understanding of the possibilities for creating such pulses including mode-locking or Q-switching, as well as other techniques for creating pulse trains with a wide range of repetition rates and pulse widths that use optical modulators, beam splitters, optical delay lines and booster amplifiers. The incident pulse train can be expressed by

$$I(r,0,t)=\sum_{n=0}^{\mathbb{N}} I_n f(r,t-nt_r) \tag{5-1}$$

where I_n is the initial peak intensity of the nth pulse, t_r is the pulse separation and $f(r,t-nt_r)$ describes the incident pulse shape.

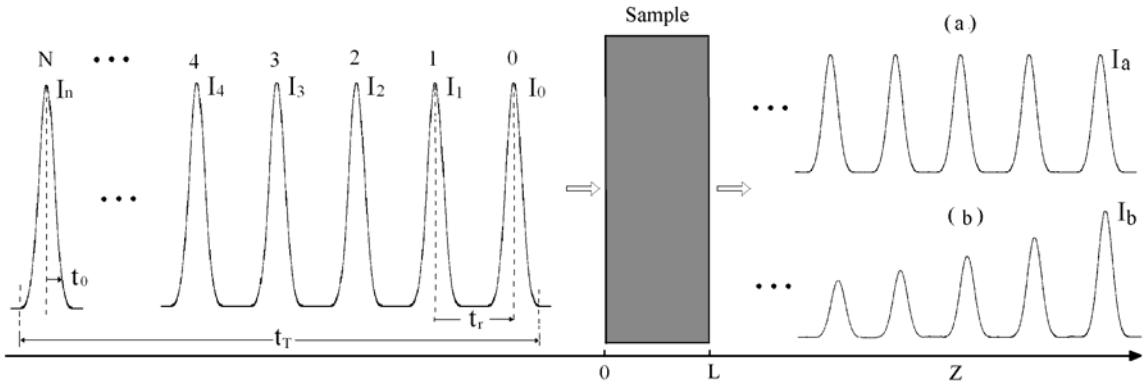

Fig.5-1. Schematic diagram of multi-pulse train system:

(a) linear absorptions pulse train (b) nonlinear absorption pulse train.

There are many types of pulse shapes and pulse sequences that can be described by Eq. (5-1). However, for the investigations of this paper, we will use a sequence of pulses as shown in Fig. 5-1, which illustrates an input pulse train as it propagates in space, approaching the nonlinear material from the left. On the right side of this figure we show the pulses as they exit the sample where part (a) shows the output in the linear absorbing region and part (b) shows the output in the nonlinear absorbing region.

As noted in the figure, t_0 and t_T represent the 1/e temporal pulse half width and the time of the entire pulse train respectively. On the right hand side we show the output of the pulse train for (a) linear absorption where the output intensity is $I_a < I_n$ and (b) nonlinear absorption where the output intensity of the leading pulse is $I_b < I_n$. In general I_a does not equal I_b. An input pulse can be described by the function given by

$$I(r,0,t) = I_0 \exp\left(-t^2 / t_0^2\right) \exp\left(-r^2 / r_0^2\right) \tag{5-2}$$

where I_0 is the peak intensity, r_0 is the 1/e pulse radius, t_0 is the 1/e temporal pulse half width. For multiple pulses the input intensity is given by

$$I(r,0,t) = \sum_{n=0}^{\mathbb{N}} I_n \exp-\left[\left(t - nt_r\right)^2 / t_0^2\right] \exp-\left[r^2 / r_0^2\right] \tag{5-3}$$

We use a nonlinear absorber (i.e. chromophore) for the material in Fig. 5-1. A schematic energy level diagram for a typical chromophore [15], [22] is shown in Fig. 5-2.

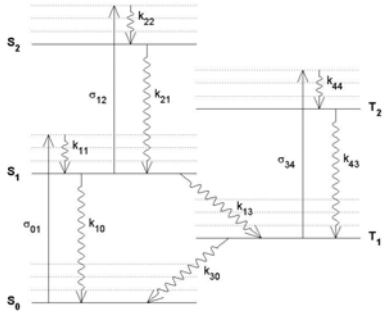

Fig. 5-2. Schematic energy level diagram for a general five level chromophore

The labels S_0-S_2 correspond to the singlet states and the labels T_0 and T_1 correspond

to the triplet states of the chromophore. Additionally, each level is labeled by N_0-N_4 corresponding to the population densities for each level. The $\sigma's$ are absorption cross-sections and the k's are the decay rates for the chromophores.

Material parameters, referred to in Fig. 5-2 include the cross-sections for absorption ($\sigma_{01}, \sigma_{12}, \sigma_{34}$), and the decay rates ($k_{10}, k_{21}, k_{13}, k_{43}, k_{30}$) which are related to the decay rates t_{ij} as $k_{ij}=1/t_{ij}$. The decay channels, with decay rates k_{11}, k_{22}, k_{44}, are assumed to be instantaneous. The initial population density (i. e. chromophore concentration) N_T and the material thickness L are also included in the calculation. The optical beam parameters include the pulse intensity, width, radius, shape, repetition rate and number of pulses in the train. The calculation parameters include the number of radial, temporal and propagation steps as well as the radial, temporal and propagation step size. The numerical method fully discretizes the optical pulse and material property at each propagation step in the calculation. The material and optical parameters are defined in Table 5-1.

Table 5-1. Definitions of parameters used in the calculation.

Parameters	Description	Symbol
Material Parameters	Concentration of the chromophore	N_T
	Absorption coefficient from state 0 to state 1	σ_{01}
	Absorption coefficient from state 1 to state 2	σ_{12}
	Absorption coefficient from state 3 to state 4	σ_{34}
	Decay rate from state 1 to state 0	k_{10}
	Decay rate from state 1 to state 3	k_{13}
	Decay rate from state 2 to state 1	k_{21}
	Decay rate from state 3 to state 0	k_{30}
	Decay rate from state 4 to state 3	k_{43}
	Material thickness	L
Optical parameters	Temporal 1/e pulse half-width	t_0
	Temporal interval between pulses	t_r
	Temporal length of pulse train	t_T
	Number of pulses in the pulse train	$\mathbb{N}$
	Radial 1/e pulse width	r_0
	Input energy of the nth pulse	E_n
	Input intensity of the nth pulse	I_n
	Wavelength of the laser beam	λ

The laser matter interaction is described by the coupled propagation equation (laser) and rate equations. Because there a variety of methods and approximations for these equations, we present a sampling of references [3, 15, 19, 21-25]. The propagation equation is given by [21-25]

$$\frac{\partial I(r,z,t)}{\partial z} = -\left(\vec{\sigma}\bullet\vec{N}(r,z,t)\right) I(r,z,t) \tag{5-4}$$

where

$$\vec{\sigma}\bullet\vec{N}(r,z,t) = \sigma_{01}N_0(r,z,t) + \sigma_{12}N_1(r,z,t) + \sigma_{34}N_3(r,z,t)\,, \tag{5-5}$$

and $N_i(r,z,t)$ are the populations of the i^{th} energy level and $\vec{\sigma}$ are the cross-section of absorption. This equation is coupled to the rate equations given by

$$\frac{\partial\vec{\mathbb{N}}(r,z,t)}{\partial t} = \left(\hat{G} + \frac{I(r,z,t)}{\hbar\omega_0}\hat{H}\right)\vec{\mathbb{N}}(r,z,t)\quad, \tag{5-6}$$

where the matrices $\hat{G}$ and $\hat{H}$ are given in Appendix A. Experiments involving the

transmission of light through the nonlinear absorber are often performed to measure the absorption as a function of incident light. The transmission is defined as the ratio of the output light energy to the input light energy as given below

$$T = \frac{E_{out}}{E_{in}} = \frac{\int I(r,L,t) r dr dt}{\int I(r,0,t) r dr dt} \tag{5-7}$$

The relationship between the time constants of the laser pulses and the dynamics of the material is quite complex. Table 5-2 gives the actual values for the material parameters considered in this paper. From this table we see that the decay times t_{21} and t_{43} are the fastest and are about a psec, t_{10} and t_{13} are about 1-30 nsec, and the slowest decay time is t_{30} which is around 20 to 40 sec. For single pulse excitations it is convenient to introduce a dimensionless parameter ρ defined as $\rho = t_0 \left(t_{10}^{-1} + t_{13}^{-1} \right)$ [5-7]. This allows us to group single pulse excitations in to three sets corresponding to $\rho < 1$, for transitions populating the singlet states; $\rho \sim 1$, for transitions populating both the singlet and triplet states; and $\rho > 1$, for transitions populating the triplet states. When we consider multipulse excitations, the situation is much more complicated and we must consider both how the repetition rate of the excitation and how the strength of the excitation relates to these decay rates. We also introduce time regimes $t_g < t_r < t_T$ (i.e. effective single pulse regime) and $t_r < t_g < t_T$ (i.e. effective multiple regime), where t_g is the decay time to the ground state from either the singlet or the triplet state.

Table 5-2. Values of parameters used in the calculation.

Parameters	Material	
	SiPc	C_{60}
N_T (10^{18} cm^{-3})	4.8	1.5[b]
σ_{01} (10^{-18} cm^2)	2.4[a]	3.1[b]
σ_{12} (10^{-18} cm^2)	30.0[a]	16.0[b]
σ_{34} (10^{-18} cm^2)	48.0[a]	14.0[b]
k_{10} (ns^{-1})	0.144[a]	0.03[b]
k_{13} (μs^{-1})	77.8[a]	740.0[b]
k_{21} (ps^{-1})	1.0[a]	1.0[b,c,d]
k_{30} (ms^{-1})	50.0[a]	25.0[b]
k_{43} (ps^{-1})	1.0[a]	1.0[b,c,d]
L (mm)	0.6	1.0[b]
t_0 (ns)	20.0	
t_0 (ns)	1.0	
t_0 (ps)	40.0	
t_{FWHM} (ns)		8[b]
t_{FWHM} (ps)		30[b]
r_0 (μm)	40	33.4[b]
λ (nm)	532	532[b]

[a]Ref.[12]
[b]Ref. [13]
[c]Ref. [26]
[d]Ref. [27]

In addition we examine four optical intensity domains: (1) I_n corresponding to linear absorption, (2) I_n corresponding to nonlinear absorption, (3) I_n near the onset of saturation, and (4) I_n corresponding to highly saturated nonlinear absorption. Since the population of each level depends on several factors including the cross-sections for absorption, the population density and the decay time/rate of each level, it is convenient to introduce dimensionless optical pumping parameters defined as

$$\eta_i = t_{ji}\sigma_{ij}I_iN_i/\hbar\omega \tag{5-8}$$

where the σ_{ij} are the absorption cross sections given in Table 5-1.

5.3 Results and Discussion

In this section we first compare our numerical results to previous single pulse experiments[13] for the transmission as a function of input energy and plot the normalized population densities vs. time and radius. We define the full width half maximum (FWHM) pulse width by t_{FWHM} ($t_{FWHM} = 2t_0\sqrt{\ln 2}$) and show that for t_{FWHM} =30 ps (ρ < 1) the population remains primarily in the singlet states whereas, for t_{FWHM} =8 ns pulses (ρ > 1) the population is transferred to the manifold of triplet states, in agreement with experiments.[13] We then investigate the effects of multiple pulses on a class of nonlinear absorbers, the phthalocyanines. We investigate pulse widths of t_0= 40 ps (ρ < 1), t_0= 1 ns (ρ ~ 1) and t_0= 20 ns (ρ > 1), and show the transmission curves as a function of input energy. The temporal and radial pulse shapes for various input energies are given and the radial dependence of the population densities is presented to illustrate their relationship with the pulse shapes. Additionally, the code enables us to vary a chromophore's photo-physical properties so that the absorption action may be optimized for any repetition rate.

5.3.1 Comparison with Prior Experimental Results

First we demonstrate our numerical method using experimental data from a 2.59 mM C_{60} toluene solution [13]. The laser repetition rates for these experiments were sufficiently long so that the system behaved as if it were in the single pulse regime (i.e. $t_g<t_r<t_T$). The measurements were made with a nanosecond/picosecond Nd:YAG laser system consisting of a Q-switched oscillator producing t_{FWHM} = 8 ns pulses and a

mode-locked oscillator producing t_{FWHM} = 30 ps pulses. The Nd:YAG output was frequency doubled to produce a wavelength of 532 nm. The laser outputs were focused down to spots with $1/e^2$ diameters, $2w_0$ ($w_0 = \sqrt{2}r_0$) of 94.4 and 96 μm for the nanosecond and picosecond beams, respectively[13] so that the interaction region was essential collimated over the sample length.

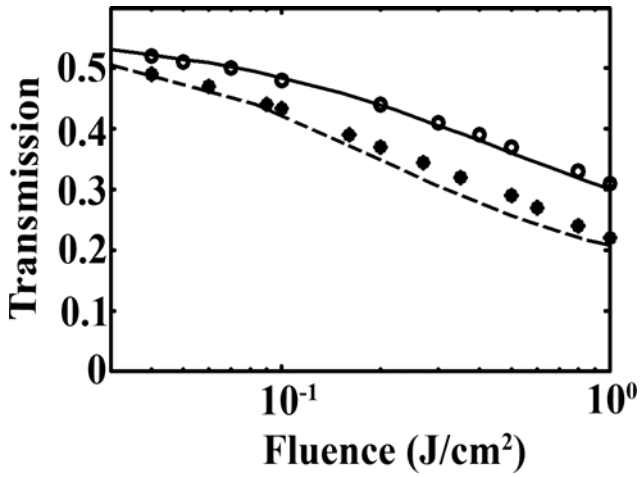

Fig. 5-3. Transmission data as a function of input fluence for t_{FWHM} = 8 ns (open circles). t_{FWHM} =30 ps (closed circles) obtained from experimental results given in ref. [13]. The solid (dashed) line is our numerical calculation for the 8 ns (30 ps) data

We use Eqs. (5-4) and (5-6) to calculate the transmission curve as a function of input fluence with the parameters[13,18,19] given in the Table 5-2**.** In Fig. 5-3, the solid line is our numerically calculated curve and the open circles are the experimental data for ρ >1 (t_{FWHM} = 8 ns) pulses; whereas, the dashed line is our calculated curve and the closed circles are the experimental data for ρ <1 (t_{FWHM} = 30 ps) pulses. Our numerical method shows good agreement with the experimental data obtained from ref. [13]. In Fig. 5-4 we show a comparison of our numerical calculation to calculations from ref. [13] for the population density as a function of

time. Again we show excellent agreement with prior results.

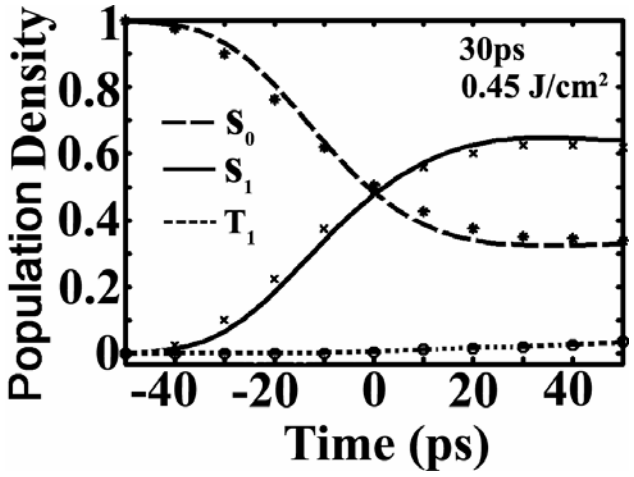

Fig. 5-4. Population density as a function of time for C_{60}. Calculations are indicated by the solid, dashed and dotted lines and the dots, crosses and open circles correspond to the experimental data. The input parameters are $\rho < 1$ (t_{FWHM}=30 ps) and input fluence=0.45 J/cm^2.

5.3.2 Investigation of the Effective Multipulse Regime

In this section we investigate the effective multipulse regime (i.e. $t_r < t_g < t_T$). Our model and numerical method is applicable to a wide range of excitation conditions. The main factors for consideration in the optical pulse-material dynamics are: (1) the normalized optical pumping parameters described by $t_{ij}\sigma_{ij}I_iN_i/h\omega_0$. (In this paper we will let all pulse intensities be equal such that $I_n = I_0$ to simplify the discussion.) and (2) the time constants of the chromophore which include $k^{-1}_{ij} = t_{ij}$ where the t_{ij} are the time decays corresponding to the decay rates given in Table 1, and the optical pulse parameters which include the pulse width (t_0), the pulse separation (t_r) and the total duration of the pulse train ($t_T =$ $\sum_N t_r$).

For the purpose of illustration we keep the absorption coefficients of the chromophore constant, as given in Table 1, where the relationship is $\sigma_{12}/\sigma_{10} \cong \sigma_{34}/\sigma_{10} \cong 10$ and is consistent with many chromophores[12]. We selected three different pulse widths; namely, $\rho < 1$ (40 ps), $\rho \sim 1$ (1 ns) and $\rho > 1$ (20 ns). The three different pulse widths were selected in order to demonstrate and validate the pulse width dependence on the intersystem crossing rate of the molecular system**.** The physical values used for our calculations are taken from the literature for metallophthalocyanine (SiPc)[12] and are presented in Table 2 along with the other parameters used in our calculation namely the chromophore concentration (0.0048 nm^{-3}), the laser beam waist (40 μm), the laser wavelength (532 nm) and the material thickness (0.6 mm). These parameters are summarized in Table 5-2.

In this section we investigate the transmission curves as a function of energy as well as the temporal and radial pulse changes for cases: $\rho < 1$ (40 ps), $\rho \sim 1$ (1 ns) and $\rho > 1$ (20 ns). In order to focus on the relationship of the pulse width versus the molecular kinetics, we use a sequence of five pulses ($t_T/t_0 = 25$) and a pulse separation of $t_r/t_0 = 5$. In other words, we vary t_0 while keeping the other time constants fixed. Using the numerical method described in Sec. II, the transmission curves show a significant difference between the pulse sequences with pulse widths of $\rho < 1$ (40 ps), $\rho \sim 1$ (1 ns) and $\rho > 1$ (20 ns). Fig. 5-5 shows the transmission curves vs. input energy for these pulse sequences.

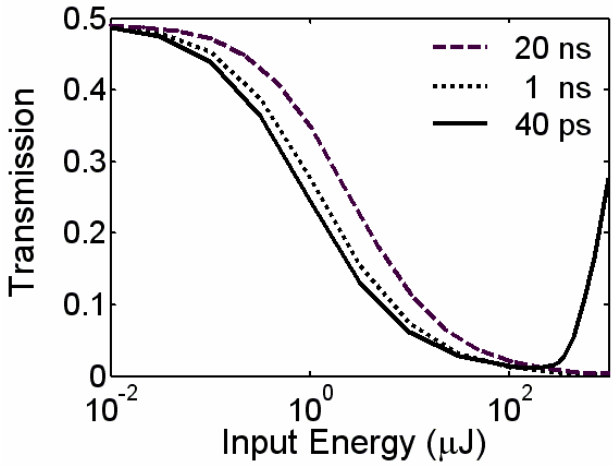

Fig. 5-5. Transmission curves as a function of input energy (E_n) into the phthalocyanine chromophore (SiPc) for t_r/t_0 =5, t_T/t_0=25, and z=L=0.6 mm and ρ <1 (40 ps) (solid line), ρ ~1 (1 ns) (dashed line), ρ >1 (20 ns) (dot-dashed line).

From Fig. 5-5, we see that the transmission decreases with increasing energy for all pulse width sequences within the range of 0.01 μJ to 100 μJ due to excited state absorption. Beyond 100 μJ, the pulse sequence for ρ <1 (40 ps) experiences saturation; whereas, those for ρ ~1 (1ns) and ρ >1 (20 ns) do not. Therefore it is of interest to examine the behavior of the pulse shapes and population densities for four regions: 0.01 μJ, 32 μJ, 100 μJ and 1000 μJ. At 0.01 μJ the transmission is linear for all pulse widths, at 32 μJ the transmission is nonlinear for all pulse widths, but the transmission is different at ~100 μJ and 1000 μJ for the various pulse widths (i.e. for ρ <1 the transmission is near saturation for 100 μJ and highly saturated at 1000 μJ, but for ρ ~1 and ρ >1 the transmission does not saturate.) Since the behavior for ρ <1 differs from both ρ ~1 and ρ >1, we shall first examine both the temporal and radial shapes of the output pulses for selected input energies of the 40 psec pulses.

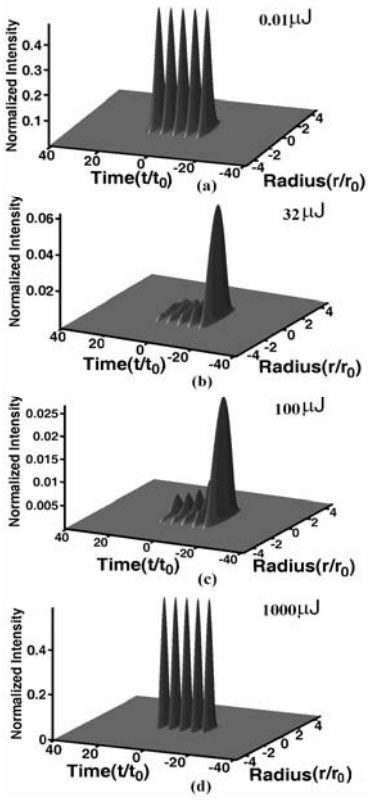

Fig. 5-6. Plots of intensity vs time and radius at z=L, ρ <1 (40 ps) , t_r/t_0=5 and t_T/t_0=25. The plots show the negative time axis going to the right to represent pulses propagating in space. The time t=0 corresponds to the center of the middle pulse.

In Fig. 5- 6, we present the output pulse shape vs. both time and radius, for pulse energies of 0.01 μJ , 32 μJ, 100 μJ and 1000 μJ for the pulse sequence consisting of 40 psec pulses. The output energy drops dramatically as the input pulse energy increases from 0.01 μJ to 32 μJ. This basic mechanism of reverse saturable absorption is due to the fact that the excited state absorption cross section is much larger that the ground state absorption cross-section. In addition, we see from Fig. 5-6 that for the 32 μJ and 100 μJ cases, the leading pulse is much stronger than the trailing pulses. This effect, as well as the reverse saturable absorption is understood by looking at the first column of Fig. 5-7. This figure is a plot of the on axis population densities vs.

time for various pulse energies and various values of ρ. The first column is related to the case of 40 psec pulses. Only the populations of states S_0, S_1 and S_2 are shown on these plots. N_3 and N_4 remain negligible and therefore are not shown in the ρ<1 (40 ps) case. From Fig. 5-7, the dramatic drop in output energy as the input energy is increased to 32 μJ is because the excited state, S_1, is becoming populated and the absorption between this state and state S_2 is large whereas the population of upper excited state S_2 remains small due to the fast relaxation from this state. As the input energy is increased to 100 μJ, we see that the first pulse in the sequence transfers most of the population out of the ground state and significantly populates the excited state S_1. Note that S_2 begins to show signs of being populated even at this energy. As the input energy is increased to 1000 μJ, the situation of the electron populations changes dramatically. The ground state population is totally extinguished during the first pulse and remains so throughout the rest of the pulse sequence. Also, the pulse energy is so large that the fast relaxation from S_2 can not keep up with pumping to that level from S_1. As soon as the pulse excitation ceases, S_2 relaxes quickly. This leads to the strong population oscillations observed in the ρ<1 1000 μJ case. The result is that bursts of light get transmitted through the material, as shown in Fig. 5-6d, and this explains the increased transmission beyond 100 μJ shown in Fig.5-5

Whereas relaxation to the triplet states was not significant for the psec excitations, intersystem crossing experienced by the nanosecond pulses enables the continued RSA. Since the relaxation time from level III to level 0 is about 0.02 ms, absorption from level III to level IV is possible for the nanosecond duration

pulses. Because the excited state absorption cross-section σ_{34} is larger than that of the ground state absorption cross-section σ_{01}, additional light is absorbed if the population has accumulated at N_3. These effects contribute to the nonlinear absorption up to 1mJ for the nanosecond pulses.

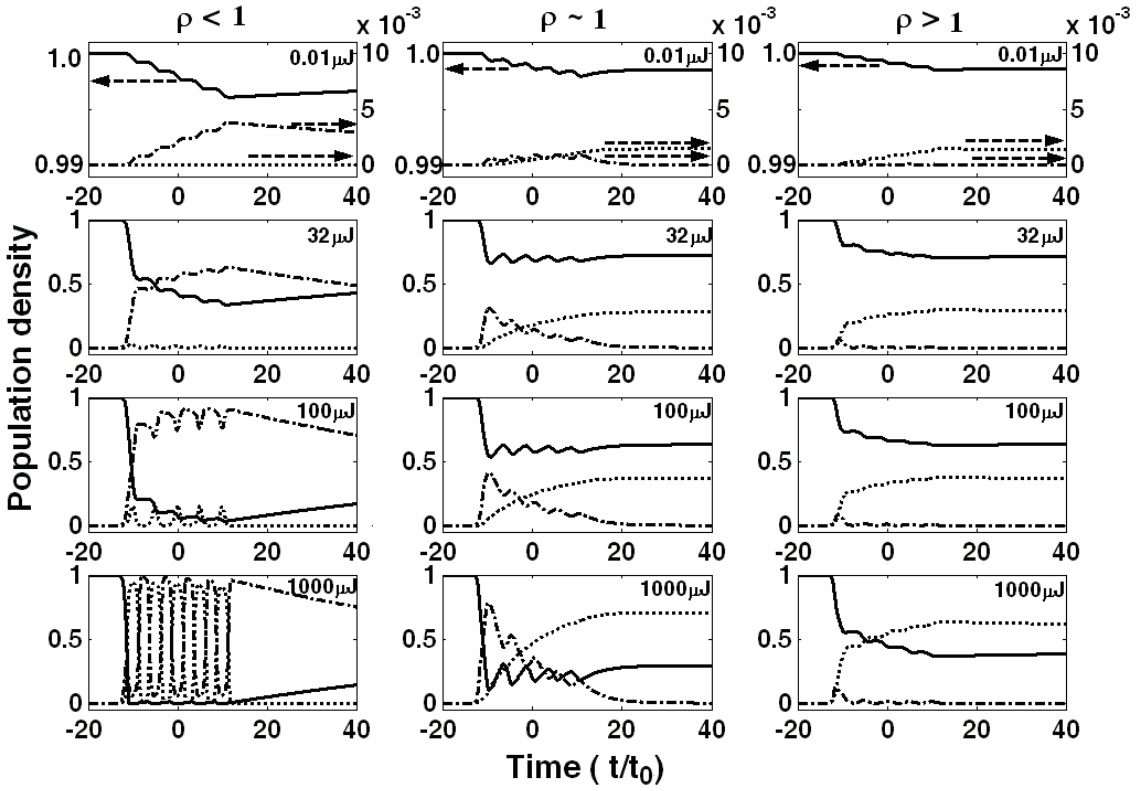

Fig. 5-7. Population densities vs time for ρ<1 (40 ps), ρ~1 (1 ns) and ρ>1 (20 ns) pulse train at z=0, and r=0. Left column: ρ<1, we show the population on the ground state N_0 (solid line), level I N_1 (dashed line) and level II N_2 (doted line); Center column: ρ~1, we show the population on the ground state N_0 (solid line), level I N_1 (dashed line) and level III N_3 (doted line); Right column: ρ>1, we show the population on the ground state N_0 (solid line), level I N_1 (dashed line) and level III N_3 (doted line).

Level II is not significantly populated in the 1 ns and 20 ns pulse train excitations

however, Level III is. Therefore, we show N_0, N_1 and N_3 in the second and third columns of Fig. 5-7. Again, as we compare Fig. 5-6 to Fig. 5-7, we can clearly see the effects that the level populations have on the output pulse train. At low energy, there is little population change, consistent with linear absorption. As the input increases to 32μJ, there is significant amount population on the level I. When the input is increased to 100 μJ, the ground state population is still depleted by the first pulse however, for these longer ns range pulse train excitations, the population is able to be transferred to the triplet state T1 (i.e. level III) due to the longer time interval between pulses as compared to the psec pulse excitation case. As level III becomes more populated, it will contribute more to the absorption. For the 20 nsec pulse sequence cases, shown in the third column of Fig. 5-7, it is clear that the level populations are such that the absorption continually increases as the input energy increases. And for the 1 nsec pulse sequence case, the significant population of Level I that takes place due to the first pulse in the 1000 μJ sequence does not lead to increased transmission due to the absorption resulting from populating levels I and III.

In another attempt to understand the differences in the transmission curves shown in Fig. 5-5 and to relate these to the population density curves of Fig. 5-7, we investigate both the temporal and spatial aspects of the pulse sequences. We start with an investigation of the temporal aspects. Fig. 5-8 shows the output pulse intensities for 40 ps, 1 ns and 20 ns pulse sequences as a function of time and radius for the various input energies that were considered in Fig. 5-7. The first energy shown is 0.01 μJ, which we can see from Fig. 5-3 corresponds to the linear

absorption region. In this case the normalized peak intensity for each of the pulses is 0.46 in agreement with Fig. 5-3. The next input energy is 32 μJ and all the 40 ps, 1 ns and the 20 ns pulse sequences show similar behavior which is the onset of RSA. At this onset of RSA, it is interesting to note that the trailing pulses are more absorbed than the leading pulses because of the accumulation of population in N_1 due to the leading pulses. This cumulative effect results from the long decay rate of N_1. Since the excited state absorption cross section is larger than that of the ground state, there is more than enough population in the excited state to allow the trailing pulses to be excited to the next level, which causes more and more absorption of energy from the trailing pulses. At an input energy of 100 μJ Fig. 5- 7 shows that most of the population transfer to level I happens during the first pulse (for the 40 psec, 1 nsec and 20 nsec cases), and the absorption between level I and level II dominates for the rest of the pulse train. Although the total absorption increases, Fig.5- 8 shows that the profile for the 20 nsec pulse sequence remains basically the same as the input energy is increased. The corresponding column in Fig. 5-7 indicates that the level populations simply lead to increased RSA as the input energy is increased. The temporal profiles for the 1 nsec pulse sequence ($\rho \sim 1$) shows similar behavior to the 20 nsec pulse sequence ($\rho > 1$). The reason for this is seen by comparing the corresponding columns in Fig. 5- 7 and observing that the population of level III is similar in both cases. This explains why we see the onset of saturation for the 40 ps pulse sequence and at 1000 μJ the transmission returns to the linear absorption yet, the behavior of the 1 ns and 20 ns pulse sequences are different. They do not

saturate and we continue to see the decay of the trailing pulses even at 1000 μJ input.

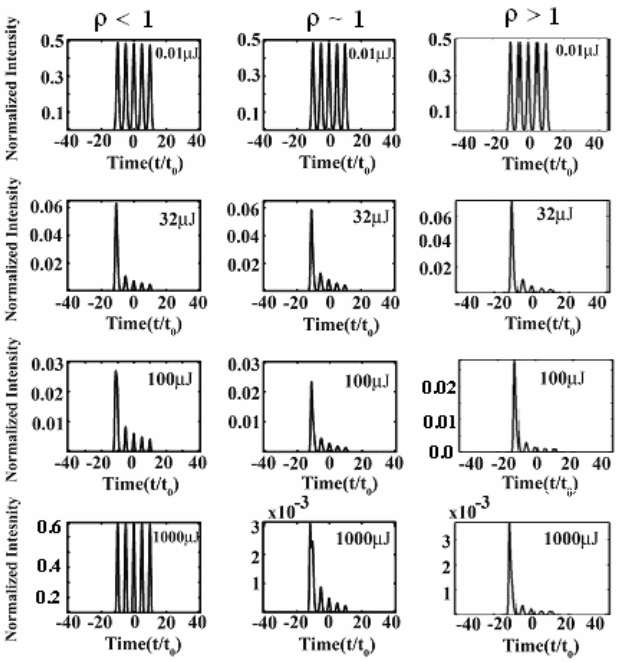

Fig. 5-8. Normalized pulse intensity as a function of time at z=L, r=0, t_0= 40 ps , t_0=1 ns and t_0= 20 ns, t_r/t_0 =5 and t_T/t_0=25 .

We now examine the behavior of the intensity as a function of radius for the same input energies as above. This is shown in Fig. 5-9 where we plot the intensity of the central pulse after it exits the material as a function radius for various input energies. At an input energy of 0.01 μJ the transmission value is 0.48 in agreement with Fig. 5-5. As the input energy increases (e.g. 32 μJ) the intensity decreases and the pulse profile begins to flatten in the radial domain.

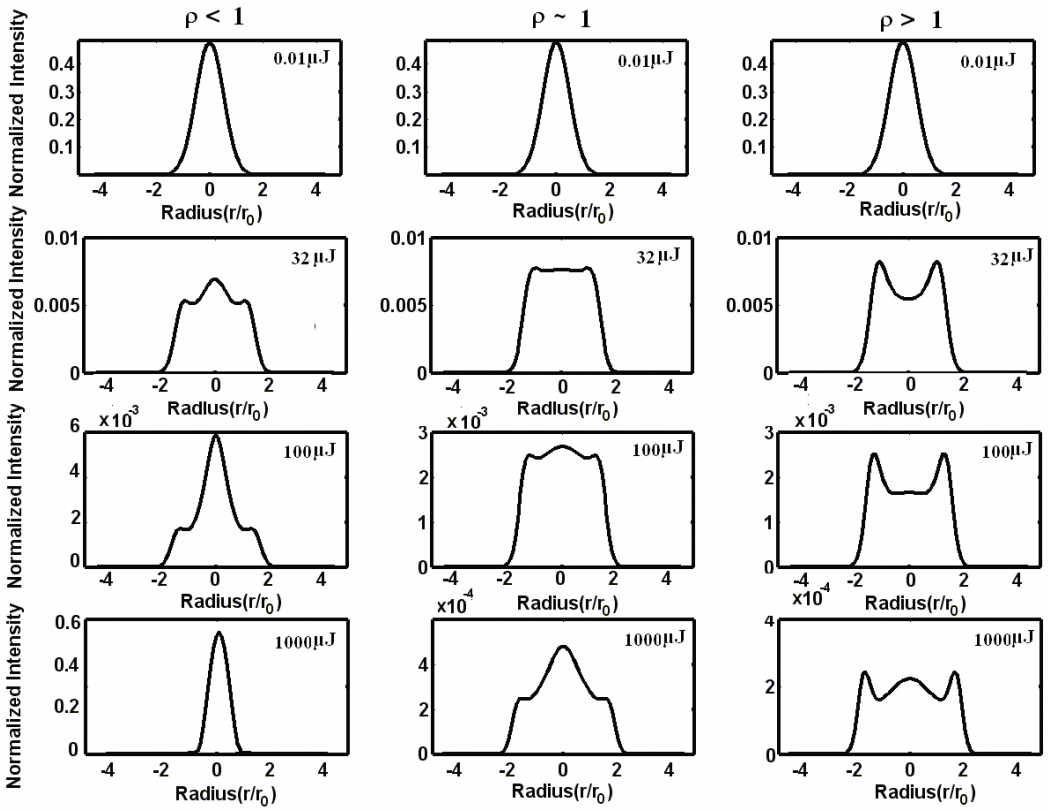

Fig. 5-9 Normalized pulse intensity as a function of radius at z=L, t=0 for ρ <1 (40 ps), ρ ~1 (1 ns) and ρ >1 (20 ns), t_r/t_0 =5 and t_T/t_0=25.

However at 100 μJ, the 40 ps pulse shows a small increase at its center. This energy value corresponds to the minimum transmission value for the 40 ps curve in Fig. 5-5. Comparison of the corresponding curve for the 1 ns and 20 ns shows that the intensity does not exhibit this increase in the center of the pulse. Then at 1000 μJ we see that the 40 ps pulse transmission corresponds to the linear absorption value; while the 1 ns and 20 ns pulses remain low. The radial domain plots clearly demonstrate the effects of saturation shown in Fig. 5-5. When we look into the radius distortion for the 1 ns and 20 ns pulses, the effect of the population N_3 is observed. Therefore both the temporal and spatial domains contain significant information about the laser-matter interaction.

5.4 Effects of Variation of Photophysical Parameters

As mentioned previously, the versatility of this numerical code enables us to vary the molecular parameters, such as absorption cross-sections, decay rates, concentration and material thickness as well as laser properties, such as intensity, pulse shape, temporal pulse width, beam waist, number of pulses, and pulse separation or repetition rate. This allows us to perform any number of numerical experiments that would be too time-consuming or costly to perform in the laboratory.

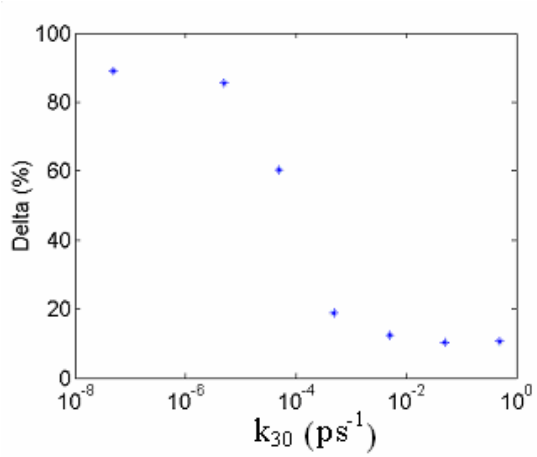

Fig. 5-10. Percentage difference between the intensity of the first (largest) and fifth (smallest) pulse in the sequence, after the pulses exit the material, as a function of k_{30} holding all other parameters fixed.

As an example of parameter variation, we calculate new values for the decays to the ground state so that the output intensity of the pulses is uniform by insuring that the population returns completely to the ground state before the next pulse arrives. The longest decay time in the system, by several orders of magnitude, is $1/k_{30}$. Therefore we adjust this parameter first. The laser input parameters assumed here are 10 μJ pulse energy, $t_r/t_0=10$, and $\rho \sim 1$ (1 ns). To illustrate the variation with respect

to k_{30} we plot in Fig. 5-10 the quantity delta, which is the percentage difference between the intensity of the first (largest) and fifth (smallest) pulse in the sequence, after the pulses exit the material, as a function of k_{30}, holding all other parameters fixed. We see that delta reaches a limiting value of around 10 percent.

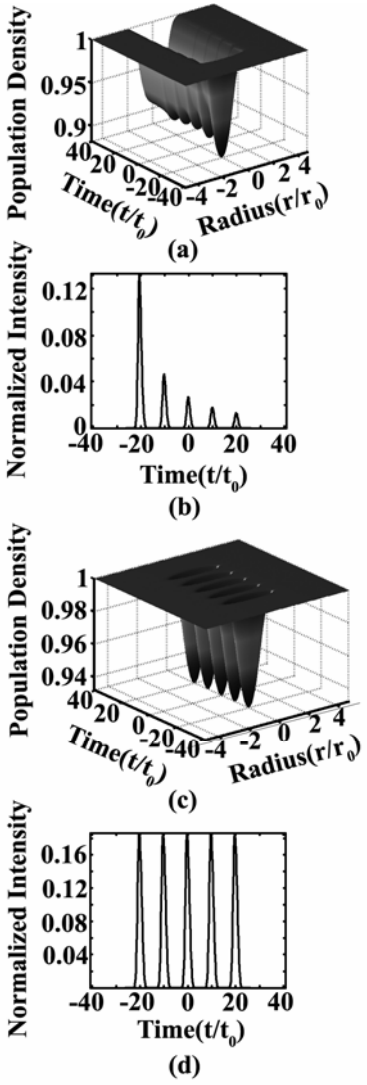

Fig. 5-11. Plots using the parameters E_{in}=10 μJ, t_r/t_0 =10, ρ ~1 (1 ns), z=L; (a) Normalized population density for vs. radius and time and (b) intensity vs. time, both plots assume k_{30} and k_{10} for the original values $k_{30} = 5x10^{-8}$ ps^{-1} and k_{10} =1.44 x 10^{-4} ps^{-1}. (c) Normalized population density vs. radius and time (d) output intensity vs. time for $k_{30} = 5x10^{-3}$ ps^{-1} and k_{10} =1.44 x 10^{-3} ps^{-1}.

Therefore it is not sufficient to change only k_{30} in order to have all the population density return to the ground state before the next pulse arrives. From Fig. 5-2 we see that the other parameter that determines the population return to the ground state is k_{10}. Fig. 5-11 shows the population density for the old values of k_{30} and k_{10}. We see that the population density does not return to the ground state before the next pulse arrives and as a result, the output intensity, as shown in Fig. 5-11 (b), exhibits a dramatic transient response. By making parameter adjustments $k_{30} = 5x10^{-3}$ ps^{-1} (an increase of five orders of magnitude) and $k_{10} = 1.44 \times 10^{-3}$ ps^{-1} (an increase of one order of magnitude) we are able to insure that the population density returns to the ground state before the next pulse arrives, as shown in Fig. 5-11 (c). This results in very uniform output pulse intensity as shown in Fig. 5-11 (d). Optimization of parameters could easily be implemented and is the subject of a future planned study. We can vary parameters to obtain various desired results for a specific application. For example, we can determine the optical pulse shape that may be of interest in laser pulse shaping in applications varying from laser machining to femtosecond laser medicine.

5.5 Conclusion

Our numerical method is able to quantify both the temporal and spatial properties at every propagation step through the material; thus, providing information unavailable from many other computational methods. This method has advantages over other commonly used techniques that use an approximate formula to fit the

transmission curve and a limited set of rate equations that (usually) depend on temporal but not radial dimensions. The rapid development of pulsed lasers and methods to increase the repetition rates makes it increasing important to determine how the variations of pulse width, pulse repetition rate, and material parameters affect transmission and optical pulse shaping. We observe dramatically different pulse train behaviors as the repetition rates of psec pulses become very fast as compared to the behavior using nanosecond and larger pulses at lower repetition rates. As we study the relaxation time and population distribution of all energy levels, we optimize those material parameters to obtain pulse trains with desired shapes.

Chapter 6 Conclusion and future work

6.1 Conclusions

We have discussed two topics: the third order nonlinearity of CdS and CdSe quantum dots composites and optical pulse simulation on organic materials. In the first topic, we investigated novel materials with large third order nonlinearity consisting of 3D semiconductor nanocrystals in an organic medium. We also discussed the synthesis method of CdSe and CdS quantum dots in reverse micelle systems, the fabrication of their thin films, and their linear characterizations. To analyze the nonlinear optical properties, we perform open aperture Z-scan and transmission measurements. We observe strong two-photon absorption effects on these two new materials.

We successfully formed a new CdS nanocomposite material using the reverse micelle synthesis method. Fine adjustments of the preparation conditions allow one to tune the absorption properties of the sample, so that one type of material may be used for different optical devices through the use of simple changes at the fabrication stage. We also developed a new fabrication method for optical thin film. This method can solve the opaque film problem, which happens to most of the high concentrated quantum dots in reverse micelle materials. By using this method, the transparent thin film of CdS and CdSe quamtun dots in reverse micelle systems was successfully formed. These new materials with strong two-photon absorption are ideal for such applications as microfabrication, fluorescence imaging, optical data storage, sensors,

optical limiters, biological and medical detectors.

We measured the two-photon absorption coefficient of CdS QD material at 532nm, and obtained the novel β value. For β values at other wavelengths, we can predict that there will be strong two-photon effects between 500nm and 700nm because the single photon absorption spectrum between 370nm and 250nm is similar to that at 266nm (half of 532nm) as showed in Fig. 6-1.

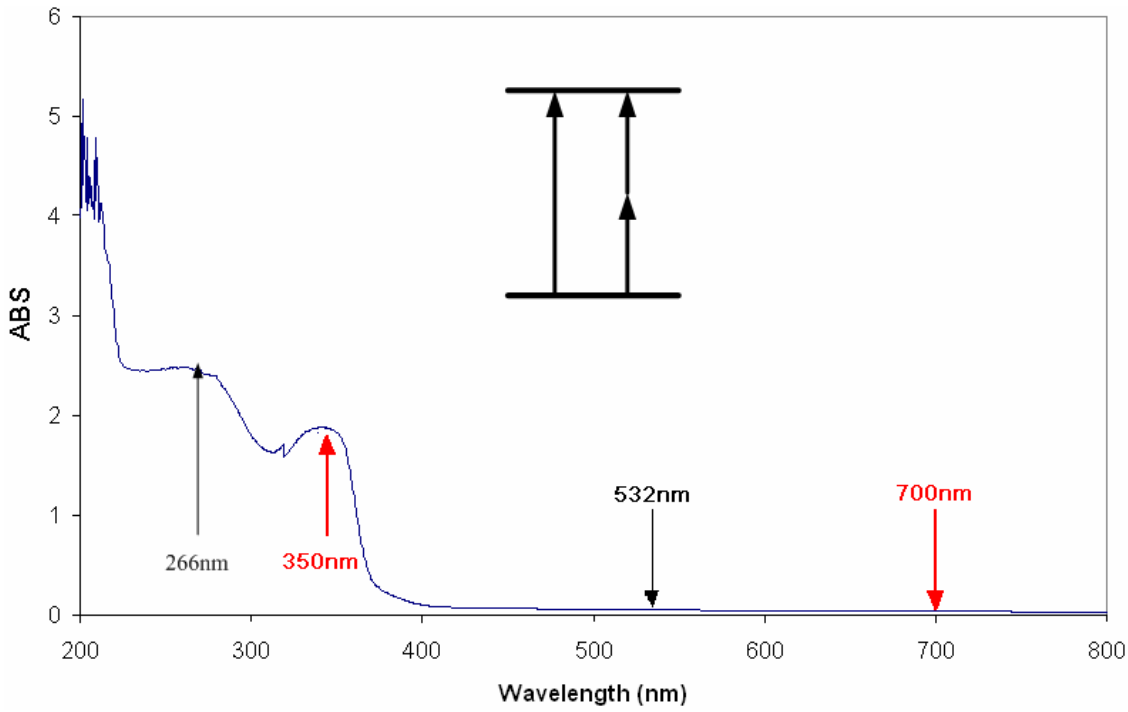

Fig. 6-1 The β value and CdS absorption spectrum

We also applied the same technique on CdSe QD capped with reverse micelle, and we observed the β value of 304cm/GW at 532nm. This novel material could have the large nonlinearity in the whole visible range too. Other properties such as energy levels and electronic lifetime about these two new quantum dots materials are of great interest for further study.

In the second topic, we demonstrated the simulation of a single pulse absorption

and multipulse train absorption on organic materials (stilbene and triarylamine derivatives). For a single pulse simulation process, we simulated the effects of excited state absorption on two-photon absorbing materials. The multipulse process is about a train of optical pulses interacting with a multilevel molecular absorber. We described a single pulse simulation theory, characteristics of population densities, and optical pulse shapes. To investigate the hybrid two-photon absorption coupled to an excited state absorber, we used current organics materials as samples in multiphoton processes. Our numerical calculations show good agreement with published results on the transmission of various input energies through these materials. Valuable insight into the photon excitation mechanism is revealed through our detailed analysis of the carrier dynamics for each level of the system. In this respect our numerical analysis is also in agreement with published experimental results for femtosecond incident pulses. Additionally, we investigated the multipulse train interacting with the nonlinear materials. The simulation showed more inside information of the optical pulse shapes as a function of space and time, and how the optical pulse was distorted as it penetrated the material. This distortion can affect the device structure by reducing the quality of the small spot size required to form high-resolution features.

6.2 Future directions

In Fig. 6-1, we can clearly observe there is a large distribution of quantum dot size from the absorption peaks. Based on the quantum dots size calculation, the radius is between 0.6nm and 1.2nm. To further study quantum dot size effects, we need to synthesize the materiel with unique size Quantum dot. To obtain the quantum dot with unique size, the low temperature synthesis is necessary.

The synthesis method could be good for other fast reaction quantum dots composites. For example, we can replace the Cd^{2+} ion by Zn^{2+} ion.

$$Cd^{2+} + S^{2-} \rightarrow CdS$$

$$Zn^{2+} + S^{2-} \rightarrow ZnS$$

By this way, we can synthesize ZnS in reverse micelle, which is possible to show the novel nonlinearity too.

Publications

We plan to send one paper about the nonlinearity of CdSe Quantum dots composite.

“Large optical nonlinearity of CdS nanocrystal in reverse micelle embedded in a thin film”, Y. Gao, A. Tonizzo, A. Walser, R. Dorsinville, and M. Potasek

It was just sent out to J. Phys. Chem.

“Dynamics of a Multilevel Molecular Absorber Interacting with a Train of Optical Pulses**”,** M. J. Potasek, M. Arend and Y. Gao, JOSA B, accepted (2006).

“Effects of excited-state absorption on two-photon absorbing materials”, Y. Gao, M. J. Potasek, App. Opt. 45, 2521 (2006)

“Highly effective thin film optical filter constructed of semiconductor quantum dot 3D arrays in an organic host”, Y. Gao, Q. Huang, J. Birman and M. J. Potasek, Photonics East, Proc. SPIE 5592, 272 (2005)

“Detailed simulation of two-photon absorption for 3D micro-nano engineering and patterning”**,** Mary J. Potasek and Yongwang Gao Proc. SPIE 5592, 389 (2005)

“Large nonlinear optical properties of semiconductor quantum dot arrays embedded in an organic medium”, Y. Gao, N. Q. Huong, J. L. Birman, and M. J. Potasek, J. Appl. Phys. 96, 4839 (2004)

“Equalization of intensity in a train of pulses using passive optical limiting in a thin film”, Y. Gao and M. J. Potasek, Photonics East, Proc. SPIE 5595, 383 (2004)

“Experimental and theoretical investigation of the third-order nonlinearity in CdS quantum dots in a dendrimer matrix”, M. J. Potasek, Y. Gao, M. Etienne, R. Dorsinville, D. Bauer, and V. Balogh-Nair, Proc. SPIE 6129, 61290H (2006)

Chapter 1 References

[1]. A. P. Alivisatos, J. Phys. Chem. 100, 13226 (1996)

[2]. D. H. Welch, D. O. McNulty, I. Alivisatos. A. P. Averback, R. S. Nozik, A. J. Alper, M. Michalske, T. A. Eastman, J. A. Russell, T. Po. Doe, Nanoscale Science, 2 (2001)

[3]. J. H. Fendler, Springer-Verlag, Berlin, 113 (1992)

[4]. J. H. Fendler, and Meldrum, F. C., Adv. Mater. 7 607 (1995)

[5]. E. Matijevie, Langmuir 10, 8 (1994)

[6]. X. Peng, L. Manna, W. Yang, J. Wickhan, E. Scher, A. Kadavanich, and A. P. Alivisatos, Nature, V 404, 59 (2000)

[7]. I. Gerdova, A. Hache. Opt. Comm. 246, 205 (2005)

[8]. V. Agranovich, Solid State Comm. 92, 295 (1994).

[9] V. I. Yudson, P. Reineker, V. M. Agranovich, Phy. Rev. B, 52, R5543 (1995).

[10].J. He, J. Mi, H. Li, and W. Ji**,** J. Phys. Chem*. B***,** 109*,* 19184 (2005)

[11]. M.Y. Han, L.M. Gan, W. Huang. C.H. Chew, B.S. Zou, C.H. Quek, G.Q. Xu, W. Ji, X.J. Zhang, S.C. Ng, Talanta 45, 735 (1998)

[12]. R. A. Ganeev, M. Baba, M. Morita, D. Rau, H. Fujii, A. I. Ryasnyansky, N. Ishizawa, M. Suzuki, M. Turu and H. Kuroda, Appl. Phys. B 78 433 (2004)

[13]. Ganeev R A, Baba M, Ryasnyansky A I, Suzuki M and Kuroda H Appl. Phys. B 80 595 (2005)

[14]. R. W. Boyd, “Nonlinear Optics”

[15]. V. Agranovich, Solid State Comm. 92, 295 (1994).

[16]. V. Agranovich, G.C. La Rocca, F. Bassani and P. Reineker, Appl. Chem. V69, 1203 (1997)

[17]. V. I. Yudson, P. Reineker, V. M. Agranovich, Phy. Rev. B, 52, R5543 (1995).

[18]. A. Engelmann, V. I. Yudson, P. Reineker, Phy. Rev. B, 57, 1784 (1998).

[19]. V. M. Agranovich, D. M. Basko, G. C. La Rocca, F. Bassani, J. Phys. Condens. Matter. 10, 9369 (1998).

[20]. N. Q. Huong and J. L. Birman, Phys. Rev. B 61, 13131 (1999).

[21]. P. K. Basu, "Theory of Optical Processes in Semiconductors: Bulk and Microstructures", Clarendon, Oxford, 352

[22]. N. Peyghambarian, B. Fluegel, D. Hulin, A. Migus, M. Joffre, A. Antonetti, S. W. Koch, and M. Lindberg, IEEE J. of Quan. Elect. 25, 2516 (1989)

[23]. http://users.ox.ac.uk/~ball2336/schrodinger.htm

Chapter 2 References

[1].G. Schmid, Editor, Clusters and Colloids: from Theory to Applications, VCH, Weinheim (1994)

[2]. A. Henglein, Small-particle research: physicochemical properties of extremely small colloidal metal and semiconductor particles, Chem. Rev. 89, 1861 (1989)

[3]. T. O'Mahony, V.P. Owens, J.P. Murrihy, E. Guihen, J.D. Holmes and J.D. Glennon, Alkylthiol gold nanoparticles in open-tubular capillary electrochromatography, J. Chromatogr., A 1004 181 (2003)

[4] U.A. Paulus, U. Endraschat, G.J. Feldmeyer and T.J. Schmidt, New PtRu alloy colloids as precursors for fuel cell catalysts, J. Catal. 195, 383 (2000)

[5] R.F. Ziolo, E.P. Giannelis, B.A. Weinstein, M.P. O'Horo, B.N. Ganguiy, V. Mehrotra, M.W. Russell and D.R. Huffmann, Matrix-mediated synthesis of nanocrystalline γ-ferric oxide: a new optically transparent magnetic material, Science 257, 219 (1992)

[6] U. Simon, G. Schon and G. Schmid, The application of Au55 clusters as quantum dots, Angew. Chem., Int. Ed. Engl. 32, 250 (1993)

[7]. S. H. Wang, S. H. Yang, Langmuir, 16, 389 (2000)

[8]. A. Lipovskii, E. Kolobkova, V. Petrikov, I. Kang, A. Olkhovets, T. Krauss, M. Thomas, J. Silcox, F. Wise, Q. Shen, S. Kycia, Appl. Phys. Lett., 71, 3406 (1997)

[9]. Kaito, C.; Saito, Y.; Fujita, K. Jpn. J. Appl. Phys. 1987, 26, (1973)

[10]. Ge, J. P.; Wang, J.; Zhang, H. X.; Wang, X.; Peng, Q.; Li, Y. D. Chem. Eur. J., 11, 1889 (2005)

[11]. Wang, W.; Liu, Y.; Zhan, Y.; Zheng, C.; Wang, G. Mater. Res. Bull., 36, 1977 (2001)

[12]. Nenadovice, M. T.; Comor, M. I.; Vasic, V.; Micic, O. I. J. Phys. Chem., 94, 6390 (1990)

[13]. Wang, C.; Zhang, G.; Fan, S. S.; Li, Y. D. J. Phys. Chem. Solids, 62, 1957 (2001)

[14]. http://en.wikipedia.org/wiki/Surfactant

[15].G. Chang, T. Huang and H. Hung, Proc. Natl. Sci. Counc. Poc(B), V24, 89 (2000)

[16]. Motte, L.; Petit, C.; Boulanger, L.; Lixon, P.; Pileni,M.P.Langmuir, 8, 1049 (1992)

[17]. Sato, H.; Hirai, T.; Komasawa, I. Ind. Eng. Chem. Res., 34, 2493 (1995)

[18]. Tanori, J.; Duxin, N.; Petit, C.; Veillet, P.; Pileni, M. P. Colloid Polym. Sci., 273, 886 (1995)

[19]. (a) Cizeron, J.; Pileni, M. P. J. Phys. Chem., 99, 17410, 1995 (b) Cizeron, J.; Pileni, M. P. J. Phys. Chem. B, 101, 8887 (1997)

[20].G. Chang, T. Huang and H. Hung, Proc. Natl. Sci. Counc. Poc(B), V24, 89 (2000)

[21]. Haram, S. K.; Mahadeshwar, A. R.; Dixit, S. G. J. Phys. Chem., 100, 5868 (1996)

[22]. Pileni, M. P. Langmuir, 13, 3266 (1997)

[23]. M. L. Curri, A. Agostiano, L. Manna, M. Monica, M. Catalano,L. Chiavarone, V. Spagnolo, M. Lugara, J. Phys. Chem. B, 104, 8391 (2000)

[24]. L. E. Brus, *J.* Chem. Phys., 80, 4403 (1984)

[25]. Nair, S. V.; Sinha, S.; Rustagi, K. C. Phys. Rev.B, 35, 4098 (1987)

[26]. A. Henglein, Chem. Rev., 89, 1861 (1989)

[27]. P. E. Lippens, M. Lannoo, Phys. Rev. *B*, 39, 10935 (1989)

[28]. Y. Wang, N. Herron, Phys. Rev. B, 42, 7253 (1990)

[29]. C. B, Murray, D. J. Norris, G. M. Bawendi, J. Am. Chem. Soc., 115, 8706 (1993)

[30]. Vossmeyer, T.; Katsikas, L.; Giersig, M.; Popovic, I. G.; Diesner, K.; Chemseddine, A.; Eychemuller, A.; Weller, H. J. Phys. Chem., 98, 7665 (1994)

[31]. Alivisatos, A. P. J. Phys. Chem. 100, 13226 (1996)

[32].L. L. Beecroft and C. K. Ober, Chem. Mater. 9, 1302 (1997)

[33].Nosaka, Y.; Yamaguchi, K.; Miyama, H.; Hayashi, H. Chem. Lett., 605 (1988)

[34]. Steigerwald, M. L.; Alivisatos, A. P.; Gibson, J. M.; Harris, T.D.; Kortan, R.; Muller, A. J.; Thayer, A. M.; Duncan, T. M., Douglass, D. C.; Brus, L. E. J. Am. Chem. Soc., 110, 3046 (1988)

[35]. Fischer, C.; Heinglein, A. J. Phys. Chem. 93, 5578 (1989)

[36]. V. Swayambunathan, D. Hayes, K. H. Schmidt, Y.X. Liao, D. Meisel, J. Am. Chem. Soc. 112, 3831 (1990)

[37]. D. Lawless, S. Kapoor, D. Meisel, J. Phys. Chem. 99, 10329 (1995)

[38]. Y. Wang, N. Herron, W. Mahler, A. Suna, J. Opt. Soc. Am. B, 6, 808 (1989)

[39]. N. Herron, Y. Wang, H. Eckert, J. Am. Chem. Soc. 112, 1322 (1990)

[40]. Z. A. Peng, and X. Peng, J. Am. Chem. Soc. 123 183 (2001)

[41]. S. A. Majetich, A. C. Carter, J. Phys. Chem., 97, 8727 (1993)

[42]. R. Rosetti, R. Hull, J. M. Gibson, and L. E. Brus, J. Chem. Phys. 82, 552 (1985)

[43]. M. Lazell, and P. J. O'Brien, Mater. Chem. 9, 1381 (1999)

[44]. P. Lianos and J. K. Thomas, Chem. Phys. Lett. 125, 299 (1986)

[45]. A. Kasuya1,A, Y. Noda1, I. Dmitruk1, V. Romanyuk1, Y. Barnakov1, K. Tohji2, V. Kumar1, R. Belosludov, Y. Kawazoe, and N. Ohuchi, Eur. Phys. J. D 34, 39 (2005)

[46]. M. Shen et al., Powder Technology 162, 64 (2006)

[47]. C.A. Leatherdale, W. K. Woo, F. V. Mikulec, and M.G. Bawendi, J. Phys. Chem. B, 106, 7619 (2002)

[48]. Takayuki Hirai, Yoko Bando, and Isao Komasawa, J. Phys. Chem. B, 106, 8967 (2002)

[49]. Jun He, Jun Mi, Heping Li, and Wei Ji, J. Phys. Chem. B, 109, 19184 (2005)

[50]. H. Du, G. Q. Xu, and W. S. Chin, Chem. Mater., 14, 4473, (2002)

[51]. Shalaev V. M. Polyakov, E Y and Markel, V. A., Phys. Rev. B. 53, 2437 (1996)

[52]. Bindra, K. S, Kar, A. K Appl. Phys. Lett., 79 3761 (2001)

[53]. M. Chamarro, V. Voliotis, M. Dib, T. Gacoin, C. Delerue, G. Allan and M. Lannoo, Proc. Mat. Res. Soc. 571, 57 (2000)

[54]. M. E. Dickinson, E. Simbuerger, B. Zimmermann, C. W. Waters and S. E. Fraser, J. Biomed Optics 8, 329 (2003)

[55].F. Stellacci, C.A. Bauer, T. Meyer-Friedrichsen, W. Wenseleers, V. Alain, S. M. Kuebler, S.J.K. Pond, Y. Zhang, S.R. Marder, J.W. Perry, Advan. Mat. 14, 194 (2002)

[56]. M. Chamarro, V. Voliotis, M. Dib, T. Gacoin, C. Delerue, G. Allan and M. Lannoo, Proc. Mat. Res. Soc. 571, 57 (2000)

[57]. http://www.dendritech.com/

Chapter 3 References

[1]. L. W. Tutt and A. Kost, Nature, 356, 225 (1992)

[2]. W. Ji, H. Du, S. H. Tang and S. Shi, J. Opt. Soc. Am. B 12, 876 (1995)

[3]. J. Staromlynska, T. J. McKay and P. J. Wilson, Appl. Phys. 88, 1726 (2000)

[4]. H. E. Pudavar, M. P. Joshi, P. N. Prasad and B. A. Reinhardt, Appl. Phys. Lett. 74, 1338 (1999)

[5]. B. H. Cumpston, S. Ananthavel, S. Barlow, D. L. Dyer, J.E. Ehrlich, L. L. Erskine, A. A. Heikal, S. M. Kuebler, I. Y. Lee, D. McCord-Maughon, J. Qin, H. Rockel, M. Rumi, X. L. Wu, S. R. Marder, and J. W. Perry, Nature 398, 51 (1999)

[6]. W. Denk, J. H. Strickler and W. W. Webb, Science 248, 73 (1990)

[7]. S. Maruo and S. J. Kawata, J. Microelectromechanical Systems **7**, 411 (1998)

[8]. S. M. Kirkpatrick, J. W. Baur, C. M. Clark, L. R. Denny, B. R. Reinhardt, R. Kannan, M. O. Stone, Appl. Phys. A 69, 461 (1999)

[9]. C. Diamond, Y. Boiko, and S. Esener, Optics Express 6, 64 (2000)

[10]. S. Kawata, H. B. Sun, T. Tanaka, K. Takada, Nature 412, 697 (2001)

[11]. M. O. Stone, J. W. Baur, L. A. Sowards, and S. M. Kirkpatrick, Proc. SPIE, 3934, 36 (2000)

[12]. S. M. Kirkpatrick, E. K. Peterman, G. T. Anderson, J. E. Franklin, and J. W. Baur, K. D. Belfield, S. J. Caracci, F. Kajzar, C. M. Lawson and A. T. Yeates, eds. Proc. SPIE, 4797, 220 (2003)

[13]. F. K. Chan, R. M. Siegel, D. Zacharias, R. Swofford, K. L. Holmes, R. Y. Tsien, M. J. Lenardo, Cytometry. 44, 361 (2001)

[14]. T. Misteli, D.L. Spector, Nat. Biotechnol. 15, 961 (1997)

[15]. M. E. Dickinson, E. Simbuerger, B. Zimmermann, C. W. Waters and S. E. Fraser, J. Biomed Optics 8, 329 (2003)

[16]. B. J. Bacskai, J. Skoch, G.A. Hickey, R. Allen and B. T. Hyman, J. Biomed Optics 8, 368 (2003)

[17]. J. W. Perry, Nonlinear Optics of Organic Molecules and Polymers, H. S. Nalwa and S. Miyata, Ed. Boca Raton, Fl:CRC, 813 (1997)

[18]. G. S. He, J. D. Bhawalkar, C. F. Zhao, and P. N. Prasad, Appl. Phys. Lett. 67, 2433 (1995)

[19]. M. Stone and R. Naik, "Encyclopedia of Smart Materials", John Wiley & Sons, New York (2000)

[20]. L. L. Brott, R. R. Naik, D. J. Pikas, A. M. Kirkpatrick, D. W. Tomlin, P. W. Whitlock, S. J. Clarkson, and M. O. Stone, Nature 413, 291 (2001)

[21].F. Stellacci, C.A. Bauer, T. Meyer-Friedrichsen, W. Wenseleers, V. Alain, S. M. Kuebler, S.J.K. Pond, Y. Zhang, S.R. Marder, J.W. Perry, Advan. Mat. 14, 194 (2002)

[22].F. Wise, ed. Selected papers on Semiconductor Quantum Dots, SPIE, 1-455 (2005)

[23]. L.L. Beecroft and C. K. Ober, Chem. Mater. 9, 1302 (1997)

[24]. H. Weiler, Angew. Chem. Int. Ed. Engl. 30, 1079 (1996).

[25]. C. Murray, C. Kagan, and M. Bawendi, Annu. Rev. Mater. Sci. 30, 545 (2000)

[26]. C. Murray, D. Norris, and M. Bawendi, J. Amer. Chem. Soc. 115 8706 (1993)

[27]. C. Murray, C. Kagan, and M. Bawendi, Science 270, 1335 (1995).

[28]. N. F. Borelli, D. W. Hall, H. J Holland and D. W. Smith, J. Appl. Phys. 61, 5399 (1987)

[29]. Y. Nosaka, K. Yamaguchi,H. Miyama, and H. Hayashi, Chem. Lett.605 (1988).

[30]. D. Lawless, S. Kapoor, D. J. Meisei, J. Phys. Chem. 99, 10329 (1995).

[31]. V. Agranovich, Solid State Comm. 92, 295 (1994).

[32]. V. I. Yudson, P. Reineker, V. M. Agranovich, Phy. Rev. B, 52, R5543 (1995).

[33]. A. Engelmann, V. I. Yudson, P. Reineker, Phy. Rev. B, 57, 1784 (1998).

[34].T. D. Krauss, F. W. Wise, Appl. Phys. Lett. 65, 1739 (1994)

[35]M. Sheik-Bahae, A.A. Said, T.H. Wei, D.J. Hagan, and E.W. Van Stryland, Journal of Quantum Electronics, JQE QE-26, 760 (1990)

[36].A. Walser, S. G. Demos, M. Etienne, R. Dorsinville, Optics Communications, 240, 417 (2004)

[37]. M. Etienne, A. Biney, A. D. Walser, R. Dorsinville, D. L. V. Bauer and V. Balogh-Nair, Appl. Phys. Lett., 87, 181913 (2005)

[38]. D. Weaire, B.S. Wherrett, D.A.B. Miller, S.D. Smith: Opt. Lett. 4, 331 (1979)

[39]. I. Gerdova, A. Hache, Opt., Comm. 246, 205 (2005)

Chapter 4 References

[1]. M. G. Silly, L. Porres, O. Mongin, P. A. Chollet, M. Blanchard-Desce, Chem. Phys. Lett. 379**,** 74 (2003)

[2]. K. Ogawa, A. Ohashi, Y. Kobuke, K. Kamada, and K. Ohta, Chem. Soc. 125, 13356 (2003)

[3]. J. Yoo, S. K. Yang, M. Jeong, H. C. Ahn, S. Jeon, and B. R. Cho, Organic Lett, 5, 645 (2003)

[4]. H. E. Pudavar, M. P. Joshi, P. N. Prasad and B. A. Reinhardt, Appl. Phys. Lett. 74, 1338 (1999)

[5]. B.H. Cumpston, S. Ananthavel, S. Barlow, D. L. Dyer, J.E. Ehrlich, L. L. Erskine, A. A. Heikal, S. M. Kuebler, I. Y. Lee, D. McCord-Maughon, J. Qin, H. Rockel, M. Rumi, X. L. Wu, S. R. Marder, and J. W. Perry, Nature 398, 51 (1999)

[6]. W. Denk, J. H. Strickler and W. W. Webb, Science 248, 73 (1990)

[7]. S. Maruo and S. J. Kawata, J. Microelectromechanical Systems **7**, 411 (1998)

[8]. S. M. Kirkpatrick, J. W. Baur, C. M. Clark, L. R. Denny, B. R. Reinhardt, R. Kannan, M. O. Stone, Appl. Phys. A 69, 461 (1999)

[9]. C. Diamond, Y. Boiko, and S. Esener, Optics Express 6, 64 (2000)

[10]. S. Kawata, H. B. Sun, T. Tanaka, K. Takada, Nature 412, 697 (2001)

[11]. M. O. Stone, J. W. Baur, L. A. Sowards, and S. M. Kirkpatrick, Proc. SPIE, 3934, 36 (2000)

[12]. S. M. Kirkpatrick, E. K. Peterman, G. T. Anderson, J. E. Franklin, and J. W. Baur, K. D. Belfield, S. J. Caracci, F. Kajzar, C. M. Lawson and A. T. Yeates, eds. Proc.

SPIE, 4797, 220 (2003)

[13]. F. K. Chan, R. M. Siegel, D. Zacharias, R. Swofford, K. L. Holmes, R. Y. Tsien, M. J. Lenardo, Cytometry. 44, 361 (2001)

[14]. T. Misteli, D.L. Spector, Nat. Biotechnol. 15, 961 (1997)

[15]. M. E. Dickinson, E. Simbuerger, B. Zimmermann, C. W. Waters and S. E. Fraser, J. Biomed Optics 8, 329 (2003)

[16]. B. J. Bacskai, J. Skoch, G.A. Hickey, R. Allen and B. T. Hyman, J. Biomed Optics, 8, 368 (2003)

[17]. J. W. Perry, in Nonlinear Optics of Organic Molecules and Polymers, H. S. Nalwa and S. Miyata, Ed. Boca Raton, Fl:CRC, 813 (1997)

[18]. G. S. He, J. D. Bhawalkar, C. F. Zhao, and P. N. Prasad, Appl. Phys. Lett. 67, 2433 (1995)

[19]. M. Stone and R. Naik, *Encyclopedia of Smart Materials,* John Wiley & Sons, New York, 2000

[20]. L. L. Brott, R. R. Naik, D. J. Pikas, A. M. Kirkpatrick, D. W. Tomlin, P. W. Whitlock, S. J. Clarkson, and M. O. Stone, Nature 413, 291 (2001)

[21]. F. Stellacci, C.A. Bauer, T. Meyer-Friedrichsen, W. Wenseleers, V. Alain, S. M. Kuebler, S.J.K. Pond, Y. Zhang, S.R. Marder, J.W. Perry, Advan. Mat. 14, 194 (2002)

[22]**.** S. M. Kirkpatrick, C. Clark, R. L. Sutherland, Mat. Res. Soc. Symp. Proc. 598, 77 (2000)

[23]. D. G. Mclean, R.L. Sutherland, M. C. Brant, D. M. Brandelik, P. A. Fleitz, T. Pottenger, Opt. Lett. 18, 858 (1993)

[24]. K. R. Welford, S. N. R. Swatton, S. Hughes, S. J. Till, G. Spruce, R. C. Hollins, B. S. Wherrett, Mater. Res. Soc. Symp. Proc. 374, 239 (1995)

[25]. C. Li, L. Zhang, M. Yang, H. Wang, Y. Wang, Physical Review A 49, 1149 (1994)

[26]. I. C. Khoo, A. Diaz, J. Ding, J. Opt. Soc. Am. B 21, 1234 (2004)

[27]. R. Lepkowicz, A. Kobyakov, D. J. Hagan, E. W. Van Stryland, J. Opt. Soc. Am. B 19, 94 (2002)

[28]. T. Xia, A. Dogariu, K. Mansour, D. J. Hagan, A. A. Said, E. W. Van Stryland, J. Opt. Soc. Am. B 15, 1497 (1998)

[29]. I. C. Khoo, A. Diaz, M.V. Wood, P. H. Chen, IEEE, Quantum Electronics 7, 760 (2001)

[30]. G. Witzgall, R. Vrijen, E. Yablonovitch, Opt. Let. 23 1745 (1998)

[31]. C. Martineau, R. Anemian, C. Andraud, I. Wang, M. Bouriau, P. L. Baldeck, Chem. Phys. Lett. 362, 291 (2002)

[32]. L. Shah, J. Tawney, Martin Richardson, K. Richardson, IEEE J. of Quant Electron 40, 57 (2004)

[33]. J. E. Ehrlich, X. L. Wu, I.-Y. S. Lee, Z.-Y, Hu, H. Rochel, S. R. Marder, and J. W. Perry, Opt. Let. 22 1843 (1997)

[34]. R. Anemian, Y. Morel, P. L. Baldech, B. Paci, K. Kretsch, J. M. Nunzi, C. Andraud, J. Mater. Chem. 13, 2157 (2003)

[35]. M. J. Potasek and Y. Gao, Nanofabrication: Technologies, Devices, and Applications, eds. W. Y. Lai, S. Pau, O. D. Lopez, Proc. SPIE 5592, 389 (2005)

[36]. S. Kim, D. McLaughlin and M. Potasek, Phys. Rev. A 61, 025801 (2000)

[37]. M. J. Potasek, S. Kim, D. McLaughlin, J. Nonlinear Optical Physics and Materials, 9, 343 (2000)

[38]. G. S. He, J. Swiatkiewicz, Y. Jiang, P. N. Prasad, J. Phys. Chem. A 104, 4805 (2000)

[39]. S. Delysse, P. Filloux, V. Dumarcher, C. Fiorini, J.–M. Nunzi, Opt. Mat. 9**,** 347 (1998)

Chapter 5 References

[1]. P. Sharma, S. Roy, C. P. Singh, Thin Solid Films, 477, 42 (2005)

[2]. F.M. Raymo and S. Giordani, Proc. Natl. Acad. Sci. 99, 4941 (2002)

[3]. L. W. Tutt and T. F. Boggess, Prog. Quantum. Elect. 17, 299 (1993)

[4]. W. R. Zipfel, R. M. Williams, W. W. Webb, Nature Biotech. 21, 1368 (2003)

[5]. W. Jia, E. P. Douglas, F. Guo, and W. Sun, Appl. Phys. Lett. 85, 6326 (2004)

[6]. A. Kobyakov, D. J. Hagan, and E. W. Van Stryland, J. Opt. Soc. of Am. B 17, 1884 (2000)

[7]. R. Lepkowicz, A. Kobyakov, D. J. Hagan, and E. W. Van Stryland, J. Opt. Soc. of Am. B 19, 94 (2002)

[8]. C. P. Cain, C. A. Toth, D. G. Noogin, D. J. Stolarski, R. J. Thomas, B. A. Rockwell, Health Physics, 82, 855 (2002)

[9]. D. H. Sliney, "Nonlinear Optics" 21, 1-17 (1999)

[10]. T. Wei, T. Huang, T. Wu, P. Tsai, M. Lin, Chem. Phys. Lett. 318, 53 (2000)

[11]. P. J. Goncalves, L. De Boni, N. M. B. Neto, J. J. Rodrigues, S. C. Zilio, I. E. Borissecitch, Chem. Phys. Lett. 407, 236 (2005)

[12]. J. W. Perry, in Nonlinear Optics of Organic Molecules and Polymers, H. S. Nalwa and S. Miyata, eds. (CRC Press, New York,), 813 (1997)

[13]. D. G. Mclean, R. L. Sutherland, M. C. Brant, D. M. Brandelik, P. A. Fleitz, and T. Pottenger, Opt. Lett. 18, 858 (1993)

[14]. J. W. Perry, K. Mansour, S. R. Marder and K. J. Perry, Opt. Lett., 19 625 (1994)

[15]. D. I. Kovsh, S. Yang, D. J. Hagan, and E. W. Van Stryland, Appl. Opt. 38, 5168

(1999)

[16]. I. C. Khoo, A. Diaz, J. Ding, J. Opt. Soc. Am. B 21, 1234 (2004)

[17]. T. Xia, A. Dogariu, K. Mansour, D. J. Hagan, A. A. Said, E. W. Van Stryland, J. Opt. Soc. Am. B 15, 1497 (1998)

[18]. I. C. Khoo, A. Diaz, M.V. Wood, P. H. Chen, IEEE, Quantum Electronics 7, 760 (2001)

[19]. R. L. Sutherland, M. C. Brant, J. Heinrichs, J. E. Rogers, J. E. Slagle, D. G. McLean, and P. A. Fleitz, J. Opt. Soc. Am. B 22, 1939 (2005)

[20]. M. J. Potasek and Y. Gao, Nanofabrication: Technologies, Devices, and Applications, eds. W.Y. Lai, S. Pau, O.D. Lopez, Proc. SPIE 5592, 389 (2004)

[21]. R. L. Sutherland, "Handbook of nonlinear optics" Marcel Dekker, New York (2003)

[22]. Y. Gao and M. J. Potasek, Appl. Opts. 45, 2521 (2006)

[23]. S. Kim, D. McLaughlin and M. Potasek, Phys. Rev. A 61, 025801 (2000)

[24]. M. J. Potasek, S. Kim, D. McLaughlin, J. Nonlinear Optical Physics and Materials, special issue: Optical Limiters, Switches, and Discriminators: Materials, Principles and Devices, 9, 343 (2000)

[25]. E. Parilov and M. J. Potasek, J. Opt. Soc. Am. B 23, 1894 (2006)

[26]. T. W. Ebbeson, K. Tanigaki, and K. Sadanori, Chem. Phys. Lett. 181, 501 (1991)

[27]. M. Lee, O. K. Song, J.C. Seo and D. Kim, Chem. Phys. Lett. 196, 325 (1992)